Université Catholique de Louvain
Secteur des Sciences et Technologies
Institut de Recherche en Mathématique et Physique
Center for Cosmology, Particle Physics and Phenomenology

Study of GigaTracker performance and a search for Axion-Like Particles at the NA62 experiment

Doctoral dissertation presented by

Alina Kleimenova

in fulfilment of the requirements for the degree of
Doctor in Sciences

Thesis Jury

Prof. Vincent Lemaître	President	UCLouvain, Belgium
Prof. Marco Drewes	Secretary	UCLouvain, Belgium
Prof. Eduardo Cortina Gil	Supervisor	UCLouvain, Belgium
Dr. Tommaso Spadaro		LNF-INFN, Italy
Dr. Artur Shaikhiev		Birmingham, UK

September, 2021

Acknowledgements

The past four years of the PhD were a challenging but joyful journey. But, of course, I would not be able to get this far alone, and therefore here I would like to express my gratitude to all the people who helped me along this path.

First and foremost, I am deeply grateful to my supervisor Prof. Eduardo Cortina Gil. Thank you for always being there for me, guiding and helping me throughout my PhD.

I thank Prof. Vincent Lemaître, Prof. Marco Drewes, Dr. Artur Shaikhiev and Dr. Tommaso Spadaro for reviewing my thesis and providing comments and suggestions, which I hope I managed to implement...

I am indebted to Dr. Tommaso Spadaro and Dr. Babette Döbrich, without whom the last chapter of this work would not be possible. Thank you for your time, patience and guidance. I cannot express enough how grateful I am for all these years...

I want to thank the members of the GTK working group with whom I had the honour and the pleasure to work. Thank you, Prof. Flavio Marchetto, Prof. Ernesto Migliore, Dr. Mathieu Perrin-Terrin and Dr. Michele Corvino. My work on the GTK was a great experience, and I have learned so much from you all. I want to express an additional thank you and sorry for Michele, whom I abandoned alone with the GTK software during the finalisation of this manuscript.

A special thank you goes to Dr. Karim Massri, who immensely helped me with the GTK software and data quality during my PhD. Thank you for teaching me so many things, and especially for Italian proverbs.

Thank you to all my CP3 friends, Alessia, Angela, Artur, Claudio, Elisa, Hesham, Luca, Ken, Philipp, Richard, Roberta, for making my time here full of fun (and chocolate and beer).

Thank you to my lockdown friends, Roland, Matteo and Valentina. I will treasure these memories of our Saturday evenings with pizza and Durak, which undoubtedly helped me during these hard times.

Thank you to my Russian friends, Sasha and Alina, for always reaching out to me and keeping in touch. I am incredibly lucky to have friends like you.

Thank you to Enrico for the patience, support and care during these years. I cannot find the right words to express how blessed and grateful I am to have you always by my side.

Спасибо моей семье, моим маме и папе. Никаких слов не хватит, чтобы в полной мере передать мою благодарность за вашу неоценимую помощь за эти долгие годы моей учебы. Эта работа была бы невозможна без вашего понимания и поддержки.

Последняя, самая главная благодарность предназначается моей бабушке Тае, которой эта диссертация посвящена. Спасибо за все твои усилия, которые ты в меня вложила, за твою любовь и заботу, за все, чему ты меня научила. Мне очень хочется думать, что ты, как никто другой, гордилась бы этим моим достижением...

Contents

Моей любимой бабушке Тае, без
которой у меня бы ничего не
получилось

Introduction

The Standard Model (SM) is the most rigorous theory of particle physics; however, as indicated by various experimental observations, it is far from being complete. For that reason, searches for New Physics effects became the central focus of modern experimental particle physics.

These effects are searched in a large variety of experiments by following one of the two main approaches: investigating with a high level of precision some of the rarest processes in nature and finding the deviations from the SM (intensity frontier) or exploring interactions at higher energy scales (energy frontier).

The fixed-target kaon experiment NA62, located in the North area of the CERN Super Proton Synchrotron, follows the intensity frontier approach. NA62 was designed to measure the ultra-rare kaon decay $K^+ \to \pi^+ \nu\bar{\nu}$ ($K\pi\nu\nu$) with a precision of 10%. The SM predicts the branching ratio of this process to be of the order of $\mathcal{O}(10^{-11})$, with the intrinsic theoretical accuracy at the 2% level. Therefore, the precise measurement of such decay can shed light on possible New Physics effects.

Due to the simple experimental signature of $K\pi\nu\nu$, the NA62 experiment has highly efficient particle identification and photon veto systems and precise tracking and timing necessary to suppress the majority of kaon decays. Together with the detector performance, the high-intensity beam setup needed to collect the large sample of kaons makes NA62 one of the best facilities to search for feebly interacting particles.

The work described in this thesis was carried out within the NA62 collaboration and is divided into two separate projects. The first project is dedicated to the NA62 beam spectrometer GigaTracKer (GTK), which provides time, momentum, direction and position measurements for the incoming beam particles. The proper calibration and data quality monitoring are the key elements in achieving the detector best performance. This work describes the GTK pixel time calibration essential for obtaining a single hit time resolution better than 200 ps, along with a summary of the developed data quality monitoring tools. Since the detector operates in a harsh radiation environment, the work would not be complete without discussing radiation damage effects. Therefore, the studies of the GTK ageing using data collected by NA62 in 2017-2018 are also reported.

The second project of this thesis focuses on searches for a light neutral spin-0 particle called Axion-like Particle (ALP). In this thesis, the sensitivity of NA62 to the $B \to K\mathcal{A}, \mathcal{A} \to \mu^+\mu^-$ process is investigated. The analysis takes a model-independent approach treating the production and decay as unrelated parameters. The search strategy, designed with the help of the simulation, relies on precise reconstruction of the dimuon invariant mass using vertices displaced with respect to the nominal kaon beamline. This work reports the analysis of the data collected in 2017-2018 corresponding to the $(4.38 \pm 0.40) \times 10^{17}$ protons on target. The preliminary results suggest that the primary source of the signal loss comes from the trigger conditions. Therefore, this thesis provides the study of possible trigger conditions to be used in the new data taking period starting in July 2021.

The manuscript is organised into four chapters. The first chapter provides a general overview of the Standard Model and the New Physics scenarios, including axions and Axion-like particles. The status of the experimental searches for these particles is also presented. The second chapter describes the NA62 experiment, its primary goal, beamline setup and the apparatus. In the third chapter, a more detailed description of the beam spectrometer of NA62 is provided, along with the description of the developed time calibration and data quality monitoring tools. In addition, it features preliminary time resolution and radiation damage studies. Finally, the last chapter of the thesis is dedicated to searches for Axion-like particles using data collected by the NA62 experiment in 2017 and 2018. The signal Monte Carlo development, the sensitivity studies and a preliminary background evaluation are discussed.

Chapter 1

Theoretical introduction

Contents

The Standard Model (SM) of particle physics describes the fundamental puzzle pieces of the Universe, the elementary particles and the interactions between them. This theory is self-consistent and extensively validated by experiments, with the recent remarkable result – the discovery of the Higgs boson by the CMS and ATLAS collaborations [1, 2]. However, despite being the most rigorous model of particle physics so far, the SM fails to explain several observed phenomena in astrophysics and particle physics itself.

From astronomical and cosmological observations [3] can be concluded that only $\sim 4\%$ of the total energy density in the Universe is in the form of "visible" baryonic matter well-described by the SM. The other $\sim 28\%$, called Dark Matter, interacts only gravitationally, and the remaining 68% exists in the form of energy known as Dark Energy. The nature of Dark Matter and Dark Energy is one of the big open questions of modern cosmology and particle physics. Moreover, the "visible" part of the Universe mentioned above does not include anti-baryons. This matter-anti-matter asymmetry can be explained by processes in the early Universe violating baryon (B) number conservation, charge (C) and charge-parity (CP) symmetries and happening out of thermal equilibrium [4]. While searches for baryon number violating processes are ongoing, CP violation was experimentally observed and introduced into the SM. Nevertheless, the source of this violation appears to be far too small to justify the existing asymmetry.

Another interesting phenomenon comes from neutrino physics. The SM describes neutrinos as massless particles; however, the experimental results indicate otherwise. In 1998, the Super-Kamiokande experiment observed that neutrino flavour could change with the travelled distance [5]; the discovery was confirmed by the Sudbury Neutrino Observatory (SNO) [6] and many other experiments later on. The existence of this effect, also known as neutrino oscillations, implies that neutrinos should have non-zero masses.

Apart from the phenomena described above, the SM suffers from several theoretical problems such as large fine-tunings of various parameters (mass of the Higgs boson, for example), the strong CP problem, the origin of the fermion mass hierarchy and the absence of gravity. All these complications, along with various experimental hints, emphasise the necessity of the SM extension by introducing unknown particles and interactions. Therefore, a considerable effort from both theoretical and experimental sides is currently being taken to seek New Physics effects.

This work aims at the experimental searches for beyond the Standard Model particles, focusing on the so-called Axion-Like particles (ALPs). Axions were first introduced to the SM as a part of the strong CP problem solution; the proposed idea was later generalised and led to the new class of particles, ALPs. In the following sections, several aspects of the Standard Model related to CP violation will be discussed. Additionally, a short review of several SM extensions with axions and ALPs and the current status of experimental searches for these particles will be provided.

1.1 CP violation in the Standard Model

The Standard Model of particle physics is defined by the gauge symmetry $SU(3)_C \times SU(2)_L \times U(1)_Y$, which describes strong and electroweak interactions between three generations of fermions, quarks and leptons [7, 8, 9]. The strong interactions are mediated by eight massless gluons and described in terms of the $SU(3)_C$ group by Quantum Chromodynamics (QCD). The electroweak interactions are represented by the $U(2)_L \times U(1)_Y$ and mediated by the gauge bosons γ, $W^{\pm}$ and Z^0. The gauge group $SU(3)_C \times SU(2)_L \times U(1)_Y$ is broken by the spontaneous symmetry breaking mechanism (the Brout-Englert-Higgs (BEH) mechanism) to $SU(3)_C \times U(1)_{EM}$. This mechanism generates masses of the fermions and $W^{\pm}$ and Z^0 bosons and gives rise to a physical scalar particle called the Higgs-boson. The schematic representation of the SM elementary particles is shown in Fig. 1.1.

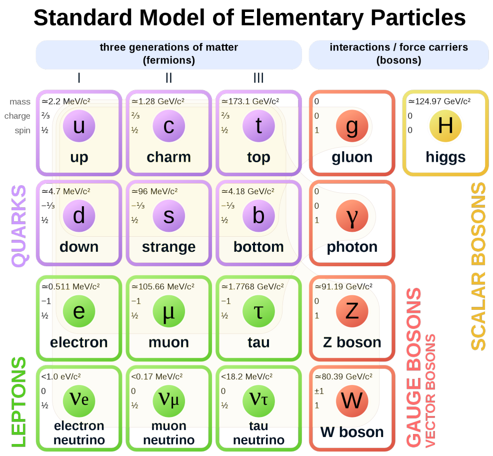

FIGURE 1.1: Schematic representation of the Standard Model of particle physics: the twelve fundamental fermions and the five gauge bosons are shown along with allowed interactions indicated with the shaded areas.[1]

There are three particularly interesting discrete symmetries in particle physics: time reversal (T) $t \to -t$, charge conjugation (C) $q \to \bar{q}$ and parity transformation $\vec{r} \to -\vec{r}$. The product of all three, CPT, is conserved accordingly to the CPT-theorem, and up to date, there is no experimentally known process proving it wrong. However, charge conjugation and parity transformation were found to be violated in the weak interactions. This observation led to the assumption that their product CP should be conserved to preserve time reversal T and CPT. Nonetheless, in 1964, CP violation was observed for the first time [10]; it took almost ten years to explain this phenomenon in the context of the Standard Model.

Before the discovery of CP violation, in 1963, to preserve the universality of weak interactions, Nicola Cabibbo postulated that the charged weak interactions are given by [11]

$$\mathcal{L}_{W^{\pm}} = \bar{u}\gamma^{\mu}(1-\gamma^{5})[d\ cos\theta_C + s\ sin\theta_C]W_{\mu} + h.c. \tag{1.1}$$

where $\theta_C = 13.2^{\circ}$ is Cabibbo angle and $u,\ d,\ s$ are quark mass eigenstates. The major problem of this theory was that, while being allowed, no strangeness-changing neutral current process was observed at the time. The solution was provided by Sheldon Lee Glashow, John Iliopoulos and Luciano Maiani [12, 13], who predicted the existence of the fourth quark c (charm) and introduced

---

[1] The figure is from Wikimedia Commons.

the unitary 2×2 quark mixing matrix V (Cabibbo matrix) such that:

$$\mathcal{L}_{W^\pm} = \begin{bmatrix} \bar{u} & \bar{c} \end{bmatrix} \gamma^\mu (1-\gamma^5) V \begin{bmatrix} d \\ s \end{bmatrix} W_\mu + h.c. \tag{1.2}$$

where

$$V = \begin{bmatrix} V_{ud} & V_{us} \\ V_{cd} & V_{cs} \end{bmatrix} = \begin{bmatrix} cos\theta_C & sin\theta_C \\ -sin\theta_C & cos\theta_C \end{bmatrix} \tag{1.3}$$

This mechanism, also known as the GIM mechanism, ensures that flavour-changing neutral current processes are not generated at the tree level. The fourth quark c was discovered in 1974 independently by Stanford and Brookhaven groups confirming the prediction [14, 15].

In 1973, even before the charm-quark discovery, Makoto Kobayashi and Toshihide Maskawa suggested that the existence of the third quark generation could explain the phenomenon of CP violation in weak interactions [16]. The Cabibbo matrix was then extended to what now is known as the CKM matrix:

$$V_{CKM} = \begin{bmatrix} V_{ud} & V_{us} & V_{ub} \\ V_{cd} & V_{cs} & V_{cb} \\ V_{td} & V_{ts} & V_{tb} \end{bmatrix} \tag{1.4}$$

The CKM matrix elements are not defined by the theory but are fundamental parameters of the SM, and therefore, their precise experimental determination is essential.

The matrix can be represented in various ways. One of the most used parametrisations of CKM, the Wolfenstein parametrisation [17], takes into account empirical hierarchy in the magnitudes of the matrix elements, and can be expressed as

$$V_{CKM} = \begin{bmatrix} 1-\lambda^2/2 & \lambda & A\lambda^3(\rho - i\eta) \\ -\lambda & 1-\lambda^2/2 & A\lambda^2 \\ A\lambda^3(1-\rho-i\eta) & -A\lambda^2 & 1 \end{bmatrix} + \mathcal{O}(\lambda^4) \tag{1.5}$$

where λ, A, ρ are real parameters, η is a CP-violating phase, $\lambda = \frac{|V_{us}|}{\sqrt{|V_{ud}|^2+|V_{us}|^2}}$ and $A \approx 1$. The unitarity of the CKM matrix ($\sum_i V_{ij}V^*_{jk} = \delta_{jk}$) leads to nine conditions on the matrix elements. The six vanishing conditions can be represented in the complex plane as triangles. Notably, the areas of all triangles are the same. The most used unitarity triangle in literature comes from dividing each side of the condition

$$V_{ud}V^*_{ub} + V_{cd}V^*_{cb} + V_{td}V^*_{tb} = 0 \tag{1.6}$$

by the best known quantity $V_{cd}V_{cb}^*$. The sketch of the triangle is shown in Fig. 1.2

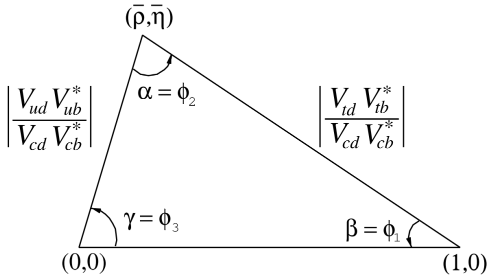

FIGURE 1.2: Unitarity triangle in complex plane $(\bar{\rho},\bar{\eta})$, where $\bar{\eta} = 1 - \lambda^2/2$ and $\bar{\rho} = 1 - \lambda^2/2$ with $\lambda = \frac{|V_{us}|}{\sqrt{|V_{ud}|^2+|V_{us}|^2}}$ [18].

All CP-violating effects in the quark sector involve a quantity called Jarlskog invariant J_{CKM} [19] defined as:

$$\mathcal{I}[V_{ij}V_{kl}V_{il}^*V_{kj}^*] = J_{CKM}\sum_{m,n}\epsilon_{ikm}\epsilon_{jln} \tag{1.7}$$

which in the Wolfenstein parametrisation is $J_{CKM} = A^2\lambda^6\eta$. This parametrisation demonstrates that the smallness of CP violation in the SM is motivated mostly by mixing angles, not by the smallness of the CP-violating phase itself. The Jarlskog invariant also has a connection to the unitarity triangle described above – the area of any CKM triangle is equal to half of J_{CKM}.

The current values of CKM matrix elements are:[2]

$$V_{CKM} = \begin{bmatrix} 0.97401 \pm 0.00011 & 0.22650 \pm 0.00048 & 0.00361^{+0.00011}_{-0.00009} \\ 0.22636 \pm 0.00048 & 0.97320 \pm 0.00011 & 0.04053^{+0.00083}_{-0.00061} \\ 0.00854^{+0.00023}_{-0.00016} & 0.03978^{+0.00082}_{-0.00060} & 0.999172^{+0.000024}_{-0.000035} \end{bmatrix} \tag{1.8}$$

and the Jarlskog invariant is $J_{CKM} = (3.00^{+0.15}_{-0.09}) \times 10^{-5}$.

Apart from the flavour physics, there are other possible sources of CP violation in the Standard Model. In particular, an analogous to the quark mixing idea is applied in the neutrino sector, where it is used to explain the phenomena of neutrino oscillations [20]. Similarly to quarks, there is a 3×3 unitary matrix describing transitions between neutrino flavour eigenstates $(\nu_e, \nu_\mu, \nu_\tau)$ and their mass eigenstates (ν_1, ν_2, ν_3). The matrix is called the PMNS-matrix after

---

[2] Complete review on the status of the measurements of the CKM elements can be found in [18].

Maki, Nakagawa, Sakata and Pontecorvo. It is similar to CKM and can be parametrised by three mixing angles and one CP-violating phase if neutrinos are Dirac or three phases if they are Majorana. The PMNS elements' hierarchy is different from CKM and indicates that neutrinos do not have the same suppression of weak interactions between generations as quarks. The current values of the PMNS elements in 3σ ranges are [21]:

$$U_{PMNS} = \begin{bmatrix} 0.801 \to 0.845 & 0.513 \to 0.579 & 0.143 \to 0.156 \\ 0.233 \to 0.507 & 0.461 \to 0.694 & 0.631 \to 0.778 \\ 0.261 \to 0.526 & 0.471 \to 0.701 & 0.611 \to 0.761 \end{bmatrix} \tag{1.9}$$

Like for CKM, one can write a similar Jarlskog invariant which will be a measure of CP violation in the neutrino sector regardless of whether neutrinos are Dirac or Majorana particles:

$$\mathcal{I}[U_{ij}U_{kl}U^*_{il}U^*_{kj}] = J^{max}_{PMNS}\, sin\delta_{CP} \tag{1.10}$$

To date, no experiment can directly measure the CP-violating phase in the PMNS mixing matrix; however, it can be estimated from the global fit of measurable variables. The current result for J^{max}_{PMNS} is $J^{max}_{PMNS} = 0.0332 \pm 0.0008 (\pm 0.0019)$ and the best fit value for J_{PMNS} is $J^{best}_{PMNS} = -0.0089$ [21]. Notably, although J_{PMNS} is not 0, δ_{CP} is found to be compatible with CP-conserving value 180 at 0.6σ [21]. Therefore, it is not confirmed whether CP is conserved in the neutrino sector or not.

Finally, yet another possible source of CP violation in the SM is also connected to quarks. It is related to the so-called Strong CP problem and will be discussed in the next section.

In conclusion, up to date, the only confirmed source of CP violation in the Standard Model is CKM. However, as stated in the introduction to this chapter, the amount of this violation is not enough to explain the observed baryon asymmetry of the Universe. Therefore, this discrepancy motivates further searches for new sources of CP violation within the SM and beyond it.

1.2 The Strong CP problem

At the beginning of its development, QCD had the so-called $U(1)_A$ problem. In short, conservation of the axial $U(1)_A$ symmetry in QCD could lead to the existence of a new pseudoscalar Goldstone boson with a mass close to the mass of the pion ($\leq \sqrt{3}m_\pi$). However, such particle was never observed and that created the $U(1)_A$ problem.[3] In the 1970s, in order to solve it, G.'t Hooft

---

[3] More details about the $U(1)_A$ problem can be found in [22].

suggested a topological CP-violating term in the QCD Lagrangian [23, 24]:

$$\mathcal{L}_{CPV} = \frac{\alpha_s}{4\pi}\theta\ TrG_{\mu\nu}\tilde{G}^{\mu\nu} \equiv \frac{\alpha_s}{4\pi}\theta\frac{1}{2}\epsilon^{\mu\nu\alpha\beta}\ TrG_{\mu\nu}G_{\alpha\beta} \tag{1.11}$$

where $G_{\mu\nu}$ is the gluon field strength tensor, the fundamental parameter θ has to be determined experimentally. One of the most sensitive tests for θ is the measurement of the neutron's electric dipole moment (nEDM), which arises from the CP-violating term in Eq. 1.11. It is expected to be of the order

$$|d_n| \sim \frac{e}{m_n}\frac{m_q}{m_n}|\bar{\theta}| \sim 10^{-16}|\bar{\theta}|\text{e cm} \tag{1.12}$$

where m_n (m_q) is the neutron (a light-quark) mass, e is the unit electric charge, and

$$|\bar{\theta}| \equiv \theta + arg\ det\ M \tag{1.13}$$

with M being the quark mass matrix. $\bar{\theta}$ is the actual observable of the CP-violating parameter of QCD. The current experimental upper limit on the electric dipole moment of the neutron $|d_n| < 3 \times 10^{-26}$ e cm [25] places an extremely stringent limit [26] on $\bar{\theta}$[4]

$$|\bar{\theta}| < 1.1 \times 10^{-10} \tag{1.14}$$

The absence of explanation why the parameter $\bar{\theta}$, a sum of two completely independent contributions, is so unnaturally small is known as the strong CP problem.

1.3 Axions and Axion-like particles

An interesting solution for the strong CP problem was proposed by Roberto Peccei and Helen Quinn in 1977 [28].[5] In this solution, a new $U(1)_{PQ}$ symmetry was introduced, and θ was promoted to a dynamical CP-conserving field $a(x)$, later called axion or QCD axion. The axion in this model is the Nambu-Goldstone (NG) boson of the spontaneously broken $U(1)_{PQ}$ symmetry [33, 34], which under $U(1)_{PQ}$ transformations translates as $a(x) \to a(x) + const$. The θ term of the Lagrangian Eq. 1.11 can be then eliminated by absorbing into the axion field, $a \equiv a + f_a\bar{\theta}$, where f_a is the strength of the axion interaction with the SM particles. This solution allows a natural explanation for the smallness of the observed nEDM from Eq. 1.12. The mass of the new NG boson is parametrically very small and can be expressed in terms of the lightest quarks

---

[4] In February 2020, the nEDM experiment at PSI published the new result, where the limit on nEDM is $|d_n| < 1.8 \times 10^{-26}$ e cm (90% CL) [27].

[5] There are alternative solutions for this problem not involving axions; for example see the following references [29, 30, 31, 32].

u and d, pion mass m_π and pion decay constant f_π [35] as

$$m_a = \frac{m_\pi f_\pi}{f_a} \frac{\sqrt{m_u m_d}}{m_u + m_d} \backsimeq 5.691(51) \frac{10^9 \text{ GeV}}{f_a} \text{ meV} \tag{1.15}$$

From the mixing with the neutral pion, the axion can have a universal coupling to photons:

$$\mathcal{L}_{a\gamma\gamma} = -\frac{g_{a\gamma\gamma}}{4} a F_{\mu\nu} \tilde{F}^{\mu\nu} \tag{1.16}$$

where the coupling constant $g_{a\gamma\gamma}$ is

$$g_{a\gamma\gamma} \sim \frac{\alpha}{2\pi f_a} \sim 10^{-13} \text{ GeV}^{-1} \left(\frac{10^{10} \text{ GeV}}{f_a}\right) \tag{1.17}$$

The original PQ model assumed that f_a is related to the electroweak symmetry breaking scale $v_{EW} = (\sqrt{2} G_F)^{-1/2} \simeq 246$ GeV, G_F being the Fermi coupling constant. However, this scenario was ruled out by the experiments later on (for example [36]), which, in turn, motivated the creation of other models.

If the coupling constant f_a is very large ($f_a \gg v_{EW}$), the new particles are very long-lived and interact very weakly. The models where such axions appear are known as invisible axion models. These models introduce $SU(2) \times U(1)$ scalar fields carrying a PQ charge, which results in the possibility of the vacuum expectation values of these fields being larger than v_{EW}. The models proposed by Kim, Shifman, Vainshtein, Zakharov (KSVZ model) [37, 38] and Dine, Fischler, Srednicki, Zhitnisky (DFSZ model) [39, 40] are typically used as benchmark examples for the invisible axion models. In brief, the KSVZ model, in addition to the PQ scalar field with $f_a \gg v_{EW}$, introduces a superheavy quark Q with $M_Q \sim f_a$ as another carrier of the PQ charge. The DFSZ Model, on the contrary, adds two Higgs doublets (as the original PQ model) and a scalar complex field with $f_a \gg v_{EW}$, which carries the PQ charge. Notably, the use of the Higgs in the DFSZ model leads to the tree-level axion-SM fermions coupling via the chiral terms in the mass matrix.

The concept of proposed anomalous Peccei-Quinn shift symmetry has been generalised to other similar (pseudo) Nambu-Goldstone bosons, axion-like particles (ALPs), which may arise from the breaking of other global symmetries such as family and lepton number [41]. These ALPs can explain various unrelated to the strong CP problem phenomena, for example, the anomalous magnetic dipole moment of muon $(g-2)_\mu$. This phenomenon is a long-standing discrepancy between experimental measurement and theoretical prediction. To date, the latest result for $\alpha_\mu \equiv (g-2)_\mu/2$ confirms the disagreement with $\alpha_\mu^{exp} - \alpha_\mu^{SM} = (251 \pm 59) \times 10^{11}$, which corresponds to a significance of 4.2σ [42, 43]. However, some models with flavour-violating ALPs can give an additional contribution to the α_μ on the level of $\Delta\alpha_\mu$ [44, 45, 46].

Axions and ALPs exist in supersymmetric models with the PQ solution to the strong CP problem. These models introduce an axion supermultiplet with an R-parity even spin-0 field s-axion and an R-parity odd spin-1/2 field axino. Both fields have couplings suppressed by the decay constant f_a and are expected to have TeV scale masses due to the supersymmetry breaking. Axion-like particles also appear in the string theory models [47, 48, 49], some of which predict even an 'axiverse' with many additional light ALPs evenly distributed in the mass scale [50, 51, 52].

Notably, the existence of axions and ALPs is strongly suggested by astrophysics and cosmology. If they are light and long-lived, they can be excellent candidates for the Cold Dark Matter [53, 54, 55, 56] and could explain various observed astronomical anomalies, for example, anomalously fast cooling of some stellar systems [57] or the seeming transparency of the galactic medium to the high energetic (TeV) gamma rays [58].

ALPs can act as mediators between Dark Matter particles and the SM, which leads to additional Dark Matter annihilation mechanisms. A general description of axion and ALP interactions can be made in terms of the so-called hidden sector portal framework, which aims to establish a systematic way to parametrise coupling of Dark Matter particles (hidden sector) incorporating SM and Dark Sector (DS) operators.[6]

In the case of ALPs, the Lagrangian can be written in the following way:

$$\begin{aligned}\mathcal{L}_{axion} = \mathcal{L}_{SM} + \mathcal{L}_{DS} + \frac{a}{4f_\gamma} F_{\mu\nu}\tilde{F}_{\mu\nu} + \frac{a}{4f_G} Tr G_{\mu\nu}\tilde{G}_{\mu\nu} + \frac{\partial_\mu a}{f_l} \sum_\alpha \bar{l}_\alpha \gamma_\mu \gamma_5 l_\alpha + \\ + \frac{\partial_\mu a}{f_q} \sum_\beta \bar{q}_\beta \gamma_\mu \gamma_5 q_\beta\end{aligned} \tag{1.18}$$

The Dark Sector Lagrangian $\mathcal{L}_{DS}$ may contain new states that provide ultraviolet (UV) completion to this model. Contrary to QCD axions, for generic axions and ALPs, there is no predictive relation between coupling and mass; thus, they can be searched in a broad range of both parameters.

The current benchmark ALP couplings summarised in the report of the Physics Beyond Colliders working group (PBC) [60] are:

- BC9: Photon coupling dominance assumes a single ALP state a with the predominant coupling to photons. In this case, production, decay and oscillation in the magnetic field can be determined as functions on $\{m_{\mathcal{A}}$, $g_{a\gamma\gamma}\}$ parameter space, where $g_{a\gamma\gamma} = f_\gamma^{-1}$.

---

[6] For more details see for example [59] and its references.

- BC10: Fermion coupling dominance assumes a single ALP state a with the predominant coupling to fermions. In this case, production and decay can be defined as functions on $\{m_a\ ,\ f_l^{-1}, f_q^{-1}\}$, where for simplicity, it is recommended to take $f^{-1} = f_l^{-1} = f_q^{-1}, g_Y = 2v_{EW}/f$. Note that despite the flavour diagonal choice of the Lagrangian Eq. 1.18, the $b - s - a$ and $s - d - a$ vertices will appear due to the loop processes.
- BC11: Gluon coupling dominance assumes a single ALP state a with the predominant coupling to gluons. In this case all related phenomenology can be defined as functions on $\{m_a\ ,\ f_G^{-1}\}$ parameter space, where the region of $m_a < m_{a_{QCD}}$ with $f_a = f_G$ requires fine-tuning and thus is less motivated.

The described interactions are effective and require UV completion at the scales at or larger than f_i. The suggested value for this cutoff is $\Lambda_{UV} = 1$ TeV.

It is worth mentioning that apart from the axion portal described above, there are a few more theoretically motivated models studied by experiments. For example, Vector portal with the Dark Photon kinetically mixed with the SM photon, Scalar portal with the Dark Scalar coupled to the SM Higgs via $H^\dagger H$ operator and Neutrino portal models with one or more additional neutrinos mixed with the SM ones.

1.4 Experimental techniques to search for axions and ALPs

Axions and ALPs are searched in a wide mass range starting from minimal 10^{-22} eV and going up to several GeV, and each mass range employs different techniques and approaches.[7] Various experiments can probe different coupling scenarios; however, the vast majority of the currently running and proposed experiments focus on the photonic-axion coupling.

Searches for axions and ALPs are performed in natural and laboratory sources. The existing experiments with natural sources can be divided into two main groups: helioscope experiments aiming to detect axions produced in the Sun and haloscope experiments looking for axions from the hypothetical Dark Matter halo [62].

In the solar environment, axions and ALPs can be produced by several reactions, the most relevant of which is the Primakoff conversion of plasma photons in the electrostatic field of charged particles. If axions couple to electrons, they also can be produced in the axion-recombination, Bremsstrahlung and Compton [63].

---

[7] This short review is based on the more comprehensive work, which can be found in [61].

Helioscopes are a typical example of a solar axion experiment. The main idea of the helioscope is that in the presence of a strong electromagnetic field, axions can be converted back to photons with energies equal to the incoming axion, X-rays. Thus, the basic layout of a helioscope consists of a strong magnet aligned with the Sun and X-ray detectors.

Another method for solar axion searches is based on Primakoff-Bragg conversion in crystalline detectors. In this case, axion-photon conversion happens in the crystalline media, and if the momentum of the axion matches one of the Bragg angles, it becomes coherently enhanced (Bragg condition). Due to the Earth rotation, the relative incoming direction of the axions with respect to the crystal planes will produce very characteristic energy and time-dependent patterns, which can be used for identification. This technique is employed in already existing underground Dark Matter or double-beta decay experiments.

Solar axions are also searched via their coupling with electrons or nucleons. In this case, they can be detected through the axio-electric effect (atomic ionisation by absorption of axions). Therefore, existing underground ionisation detectors, such as liquid Xe detectors designed to identify WIMP's (weakly interacting massive particle) interaction with the ordinary matter, are sensitive to this process and can be used for the search.

If the Dark Matter halo around our galaxy consists entirely of axions, due to its huge density of $3 \times 10^{14} (\mu\text{eV}/m_a)\ \text{cm}^{-3}$, it is possible to search for detectable effects in the laboratory experiments despite axion feeble interactions with the known matter. The principal strategy for such experiments is a haloscope technique. The technique exploits axion conversion into photons in the presence of a strong magnetic field. Since Dark Matter axions are highly non-relativistic, and therefore almost monochromatic, haloscopes use resonantly enhanced conversion in microwave cavities with the high quality factor Q. The cavity's resonant frequency must be matched to the unknown axion mass to enable the resonant conversion. Since there is a solid motivation to try a wide range of masses, this frequency must be tunable, allowing for a mass scan. The current limitation of the cavity detectors is in the mass range of a few μeV. For masses smaller than this, it may be more advantageous to use an LC circuit. In this case, if an axion with the mass of $1/\sqrt{LC}$ converts into photons in the magnetic field of the detector, it will cause specific fluctuations in the current, which can be measured and compared with the expected noise. As an alternative to the resonant cavity and LC circuit techniques, there is a concept of the dish-antenna, which employs magnetised reflective surfaces to produce photons in the presence of an axion field.

The existence of axions and ALPs can result in effects observed in the laboratory experiments without relying on natural sources. For axions and ALPs with masses below eV, three main approaches are used. The most straightforward is the so-called light-shining-through-the-wall (LSW) experiment [64], which uses a powerful source of photons, laser, for example, to create axions in the magnetic field. The axions then pass through an optical barrier and, in the presence of another magnetic field, reconvert back to photons detectable by photodetectors.

Another technique uses axion induced effects on the polarisation of laser beams passing through a magnetic field. Axion conversion into photons, in this case, can introduce changes in the ellipticity angle and add angular rotation to the laser polarisation [65].

Lastly, since light axions and ALPs can mediate long-range forces, they can be constrained by the precision measurements of Newton's law and in searches of violations of the equivalence principle.

As for ALPs with masses above MeV, these particles can be searched in the fixed target, beam-dump and collider experiments, where they can be produced in meson decays or directly in the interactions of beam particles with beam particles or the target material.

1.5 Current status of searches for axions and ALPs

This section contains a short overview of the current status of axion and ALP searches in terms of three coupling scenarios: photon, fermion and gluon. The review was based on the report of the Beyond the Standard Model working group of Physics Beyond Colliders initiative (PBC) [60]. All projected and existing limits reported in this section are set at 90% CL with $\Lambda_{UV} = 1$ TeV; the projected limits are made with 0 background events assumption.

The present status of the searches for axions and ALPs with photon coupling dominance in $(g_{a\gamma\gamma}, m_a)$ parameter space is summarised in Fig. 1.3 made by Irastorza and Redondo [61] and updated by the BSM working group of PBC [60]. It shows results obtained with various methods, namely: black or grey correspond to the laboratory and beam dump searches, blue shades highlight boundaries of the helioscope experiments or bounds from stellar physics, in green shades are shown results from helioscopes or cosmology related arguments, the yellow/orange areas correspond to the hinted parameter space regions, such as QCD axions (DFSZ and KSVZ axion models shown with red lines).

The results from laboratory experiments (dark grey) were obtained by the LSW experiment OSQAR [66] in the range below 1 meV and polarimeter PVLAS [67] in the region above 1 meV. The helioscope and haloscope results come from CAST [68] and ADMX [69] experiments. Notably, ADMX excluded KSVZ and DFSZ axion models in the mass range of $1.91 - 3.69$ μeV and $2.66 - 2.81$ μeV, respectively.

The rest, excluding beam dump experiments, comes from stellar and cosmology related limits. Label "HB" stands for the constraints from the ratio of horizontal branch (HB) stars to red giants in globular clusters (GCs) [74]. Results labelled as "Sun" come from the neutrino flux from the Sun and helioseismology [75]. "SN1987A" stands for the constraints obtained from the neutrino pulse duration of the supernovae SN1987A [76]. Results marked as "Telescopes", "X-rays" and "γ-rays" come from the data of radio, X and γ-ray telescopes [77]. Constraints with "x_{ion}" are motivated by the photoionisation cross-section of Hydrogen, which, together with UV photons from decay of axions or ALPs, can affect the history of the Hydrogen ionisation fraction [77]. Label "EBL" stands for the constraints on the extragalactic background light flux to which axion and ALP decays in the early Universe can contribute [77]. Lastly, "BBN" and "CMB" limits come from Big Bang Nucleosynthesis and Cosmic Microwave

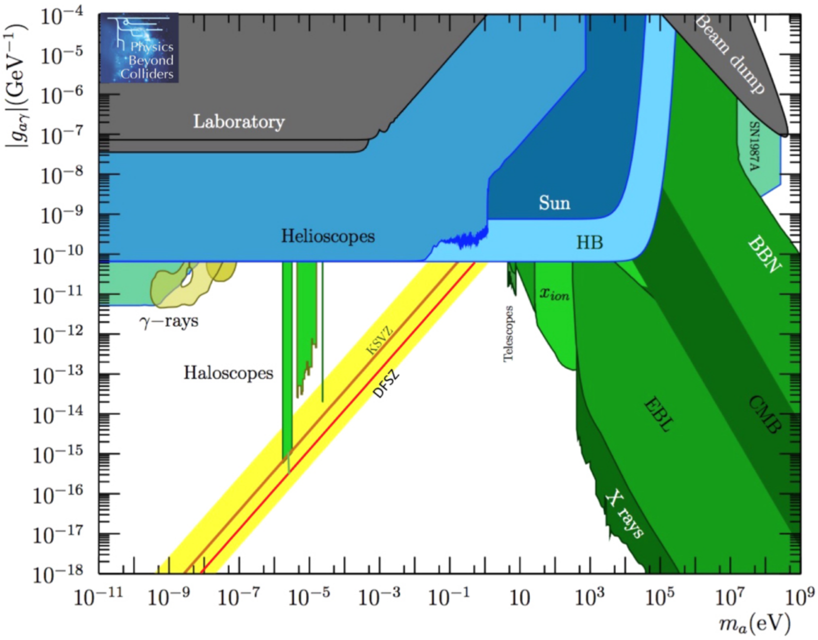

FIGURE 1.3: Current constraints at 90% CL for the axion-photon coupling in $(g_{a\gamma\gamma}, m_a)$ plane in the axion mass range from 10^{-11} eV to 1 GeV [60, 61]. Black or grey colours correspond to the laboratory and beam dump searches. Blue shades highlight boundaries of the helioscope experiments or bounds from stellar physics. Results from helioscopes or cosmology related arguments are shown in green shades. Yellow and orange areas correspond to the hinted parameter space regions, such as QCD axions (DFSZ and KSVZ axion models shown with red lines).

Background, which can be affected by axion decays before the CMB decoupling [77].

Limits and projections from the beam dump and accelerator-based experiments are shown in Fig. 1.4. Coloured areas correspond to the current bounds, which were obtained by electron beam dump experiments (E141 [78, 79] and E137 [80] in SLAC), proton beam dump experiments (CHARM [81] and NuCal [82]), the Large Electron-Positron Collider experiment OPAL from $e^+e^- \to \gamma\gamma$ [83], B-meson experiments Belle-II [84] and BaBar [85], and π^0 lifetime measurement experiment PrimEx [86]. Expected sensitivity of current (kaon experiment NA62 [71], active beam-dump experiment NA64 [70]) and future experiments (FASER [87], SHIP [88], SeaQuest [89]) are shown with lines. The results of the quoted future experiments will reduce the gap in parameter space between beam dump results and results of OPAL and BELLE-II.

The present status of searches for axions with fermion coupling dominance in

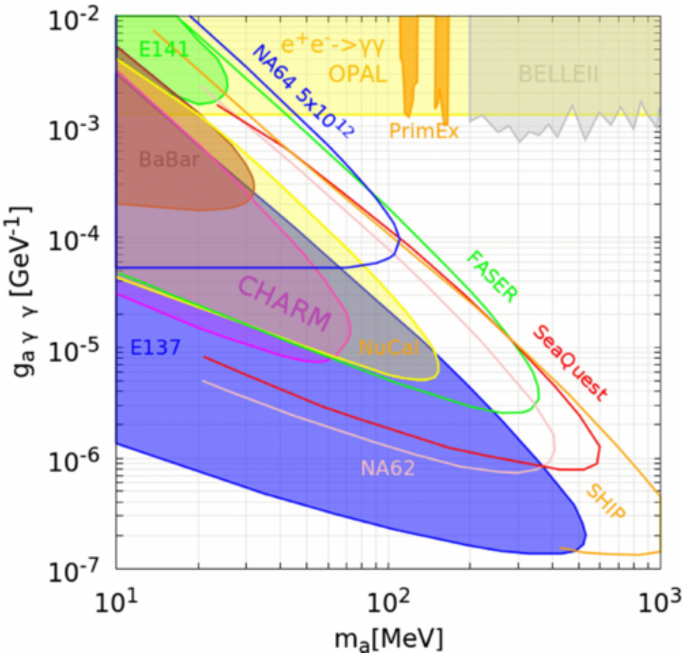

FIGURE 1.4: Current constraints at 90% CL for the axion-photon coupling in $(g_{a\gamma\gamma}, m_a)$ plane zoomed to the MeV-GeV mass range [70, 71, 72, 73]. The shaded areas show already excluded parts of the parameter space, while the solid lines correspond to the sensitivity of current and future experiments. These results were obtained using data from the beam dump and collider experiments.

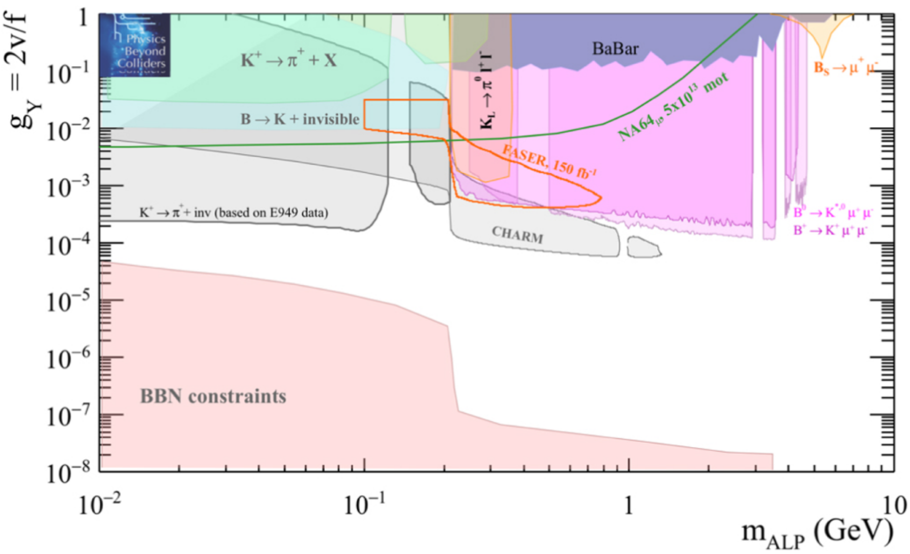

FIGURE 1.5: Current constraints at 90% CL for the axion-fermion coupling in (g_Y, m_a) plane [60]. The shaded areas show already excluded parts of the parameter space, while the solid lines correspond to the sensitivity of current and future experiments.The limits mostly come from meson decays studied at the collider and fixed-target experiments and Big Bang Nucleosynthesis marked as "BBN Constraints".

(g_Y, m_a) parameter space is shown in Fig. 1.5. The shaded areas correspond to the current exclusion limits; lines correspond to the projected sensitivity of NA64 [60] and FASER [90] experiments, the shaded area with the "BBN Constraints" label corresponds to the bounds from Big Bang Nucleosynthesis.

In the mass range shown in Fig. 1.5, ALP searches are carried out mainly at the LHC and fixed-target experiments by studying production in meson decays. The most stringent limits in the mass range below $2m_\mu$ ($\sim$ 226 MeV) are obtained by the kaon experiment E949 from $K^+ \to \pi^+ + invisible$ decay searches [91] and by CLEO in $B^0 \to K_s + invisible$ decays [92]. This mass region was recently updated by another kaon experiment, NA62, which apart from studying $K^+ \to \pi^+ + invisible$ channel, investigated $\pi^0 \to invisible$ decay [93]. In the mass range above $\sim$ 226 MeV and up to $\sim$ 1 GeV, the best limits come from the reinterpretation of the results of the CHARM experiment [81] (updated exclusion bound can be found in [94]). The strongest limits in the mass region above 1 GeV come from the collider experiments BaBar, LHCb and CMS. These experiments performed the search for ALPs with fermionic coupling in $B \to K/K^*\mu^+\mu^-$ [95, 96], $B^0 \to \mu^+\mu^-$ [97], $\Upsilon \to \mu^+\mu^-\gamma$ or $\Upsilon \to \tau^+\tau^-\gamma$ [98] decays. Notably, the LHCb results from $B \to K/K^*\mu^+\mu^-$ were initially evaluated under the assumption of the scalar particle ϕ decaying into the pair of muons. The corresponding limits in Fig. 1.5 are reinterpretations of these results from [94]. Additionally, the limits from $B^0 \to \mu^+\mu^-$ and BaBar are recast provided by [99].

Fig. 1.5 does not include the eV-sub-MeV mass region. However, axions and ALPs in this mass range can be searched via the axio-electric effect in underground experiments. At present, values of g_{ae} in the range of $1-100$ keV are excluded by PandaX-II [100] and XENON1T [101] up to $\sim 10^{-13}$. Interestingly, in the recent paper [101], XENON1T reported an excess in the mass region $1-7$ keV with a significance of 3σ, which could be either a solar axion with a mass of 2.3 keV or a tritium background. Discussions on this matter are currently ongoing.

The present status of searches for axions with gluon coupling dominance is shown in Fig. 1.6. In this scenario, ALPs mix with neutrally charged pseudoscalar mesons, and therefore they can be produced in any process where these mesons appear, including decays of B mesons. The exclusion limits shown in Fig. 1.6 with shaded areas come from the reinterpretation of results from various experiments [102]. Limits corresponding to the LEP experiments and CHARM are estimated using the results of $A \to \gamma\gamma$ analysis [81, 60]. Bounds from $b \to sa$ penguin processes were obtained from $B^\pm \to K^\pm\eta\pi^+\pi^-$, $B^\pm \to K^\pm K^\pm K_S\pi^\mp$, $B^0 \to K^0\phi\phi$ and $B^\pm \to K^\pm\omega(3\pi)$ decays [103, 104, 105], while constraints on $s \to d$ penguin decays come from studies of $K^{+/-/0} \to \pi^{+/-/0}\gamma\gamma$ [106, 107]. Production from kaons and B-mesons were obtained under the assumption that the UV-dependent factor included in the loop is approximately equivalent to $log(\frac{\Lambda^2_{UV}}{m_t^2} \pm \mathcal{O}(1))$ and under the assumption of $\Lambda_{UV} \simeq \mathcal{O}(\text{TeV})$ is taken to be unity.

In Fig. 1.6, the solid and dotted lines stand for the sensitivity of the future experiments with the timescale from 5 to 15 years. These experiments, FASER2 [90] and REDTOP [60], in particular, will be able to explore a large area of the parameter space in the sub-GeV mass range partly covered by CHARM. It is worth mentioning that the discussed limits do not include projections for NA62 and SHIP, which are also sensitive to the search in a similar coupling-mass range.

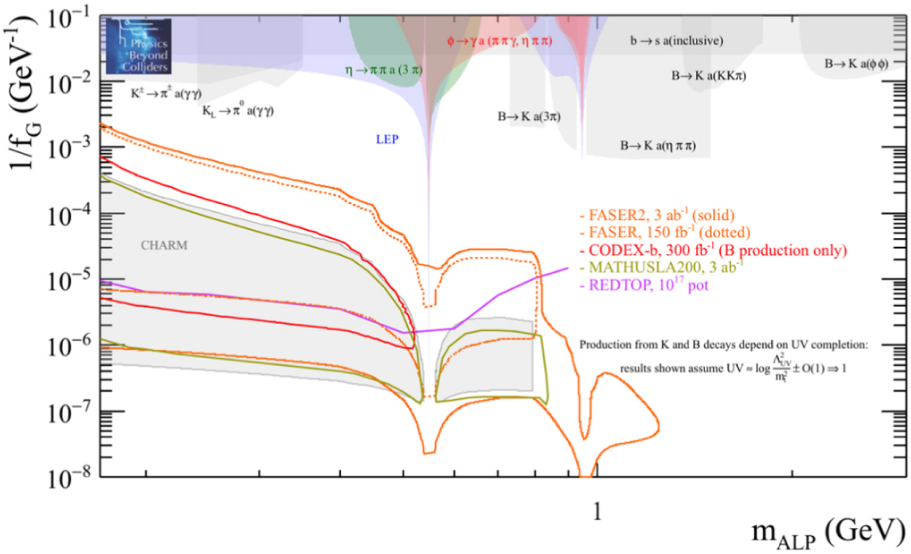

FIGURE 1.6: Current constraints at 90% CL for the axion-gluon coupling in (g_G, m_a) plane [60]. The shaded areas show already excluded parts of the parameter space, while the solid and dotted lines correspond to the sensitivity of the future experiments.

1.6 Outlook

Axions and Axion-like Particles arise from a plethora of well-motivated Standard Model extensions, explaining a large variety of different phenomena of nature, including Dark Matter, Dark Energy, Strong CP problem and many more. Thanks to this, these particles are searched for in many experiments varying in used techniques. The fixed-target kaon experiment, NA62, is also sensitive to exploring different coupling scenarios of ALPs.

This work focuses on ALPs with couplings to SM fermions produced in the $b \to s$ transitions. The existence of this particle would modify the rates of the flavour-changing processes such as $b \to s$. In the absence of data supporting any particular New Physics scenario, this search adopts a model-independent approach. In this case, the NA62 experiment has a unique opportunity to probe a parameter space for the pseudoscalars with masses in the MeV-GeV range and lifetimes of the order of nanoseconds [94], which is difficult to constrain by collider and fixed-target experiments.

The following chapter will provide a brief description of the NA62 experiment, while the sensitivity of NA62 to ALPs with fermionic couplings will be discussed in the last chapter of this thesis.

Chapter 2

The NA62 experiment

Contents

NA62 is a fixed target experiment located in the North Area of CERN Super-Proton Synchrotron (SPS) and dedicated to the rare kaon decays measurements [108]. The NA62 experiment was designed for high precision kaon physics. However, its setup, detector performances, and beam intensity allow other studies, including New Physics searches. The experiment already collected physics data in 2016-2018 and will restart its activity after the Long Shutdown 2 (LS2) in 2021.

In the following sections, a brief description of the physics motivation of NA62, its beamline and the majority of the sub-detectors will be provided. The chapter is based on the NA62 detector paper [108], which details the detectors, readout systems, and performances.

2.1 Physics motivation

The main goal of the NA62 experiment is to measure the branching ratio of an ultra-rare kaon decay $K^+ \to \pi^+ \nu\bar{\nu}$ with 10% precision. This decay is a flavour-changing neutral current (FCNC) process forbidden at the tree level in the Standard Model (see Sec 1.1). Being dominated by top quark loops, it is highly suppressed by the small value of the CKM element $|V_{td}|$. In the SM, the process can be described by the so-called box and penguin diagrams shown in Fig. 2.1.

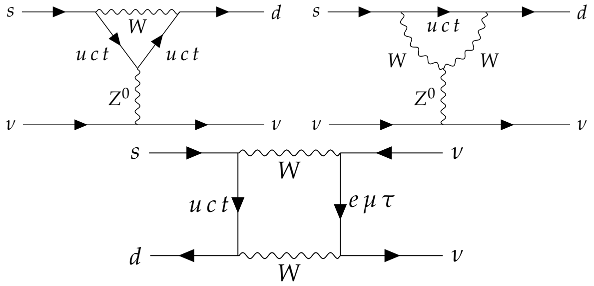

FIGURE 2.1: The penguin (top) and the box (bottom) diagrams describing the ultra-rare kaon decay $K^+ \to \pi^+ \nu\bar{\nu}$.

The most recent computation of the $K^+ \to \pi^+ \nu\bar{\nu}$ branching ratio is [109]:

$$\mathcal{B}(K^+ \to \pi^+ \nu\bar{\nu})_{SM} = (8.4 \pm 1.0) \times 10^{-11} \tag{2.1}$$

where the dominant contribution to the error comes from CKM parameters V_{cb} and γ, measured experimentally. For the illustration, the branching ratio can be expressed as

$$\mathcal{B}(K^+ \to \pi^+ \nu\bar{\nu})_{SM} = (8.39 \pm 0.30) \times 10^{-11} \cdot \left[\frac{|V_{cb}|}{40.7 \times 10^{-3}}\right]^{2.8} \cdot \left[\frac{\gamma}{73.2^\circ}\right]^{0.74} \tag{2.2}$$

to separate the theoretical uncertainty from parametric.[8]

The $K^+ \to \pi^+ \nu\bar{\nu}$ decay is extremely sensitive to the New Physics contribution: its branching ratio varies within several models, including Randall-Sundrum with protective custodial symmetry [110], littlest Higgs [111], simplified Z and Z' [112], minimal supersymmetric models [113, 114], models with leptoquarks [115] and models with invisible axions discussed in the previous chapter.

---

[8] This parametric relation is approximate and is accurate to 1% depending on the choice of the values for V_{cb} and γ.

The most precise experimental value before NA62 was obtained by the kaon experiment E949 in the Brookhaven National Laboratory [91]:

$$\mathcal{B}(K^+ \to \pi^+ \nu\bar{\nu})_{SM} = 1.75^{+1.15}_{-1.05} \times 10^{-10} \tag{2.3}$$

The large uncertainties of this measurement motivated further investigation of the $K^+ \to \pi^+\nu\bar{\nu}$ decay by the NA62 experiment (section 2.2 and onwards).

Over the data taking in 2016-2018, NA62 collected $\mathcal{O}(10^{13})$ kaons, which, assuming 5% acceptance, amounts to about twenty signal SM $K^+ \to \pi^+\nu\bar{\nu}$ events. As of date, NA62 observed one event in the 2016 data sample [116], two events in the 2017 data sample [117] and seventeen events in the 2018 data sample [118] with a total expected background of 7.0 events. As a result, NA62 achieved the branching ratio measurement at 68% CL compatible with the Standard Model prediction within one standard deviation:

$$\mathcal{B}(K^+ \to \pi^+ \nu\bar{\nu}) = (10.6^{+4.0}_{-3.4} \pm 0.9_{syst}) \times 10^{-11} \tag{2.4}$$

This measurement is the first to provide a 3.4σ evidence for the very rare $K^+ \to \pi^+\nu\bar{\nu}$ decay. Future data taking will improve this result and make the comparison with the SM more precise.

2.2 The NA62 detector layout

Unlike its predecessors, the NA62 experiment uses the decay-in-flight technique, which is reflected in its beamline, detector setup and analysis strategy. The choice of this technique is motivated by the possibility of collecting a large sample of kaon decays $\mathcal{O}(10^{13})$ over a few years of data taking. NA62 uses a high-intensity beam, which allows reducing non-kaon related background; however, in this case, kaons cannot be separated from pions and protons. The schematic layout of the NA62 detector and the beamline is shown in Fig. 2.2.

The signature of the $K^+ \to \pi^+\nu\bar{\nu}$ event is very simple: one incoming kaon track and a single detectable charged pion track in the final state. The kinematic rejection of other kaon decay modes is made by selecting two restricted regions of the squared missing mass distribution (Fig. 2.3) defined as $m^2_{miss} = (P_K - P_\pi)^2$, where P_K and P_π are 4-momenta of kaon and pion.

In order to achieve the desired kinematic rejection of the order of $\mathcal{O}(10^4 - 10^5)$, NA62 must measure the kaon momentum and angle with a precision of $\sim$ 0.2% and 0.16 mrad, respectively, while the pion track momentum and angle must have resolution better than 1% and 0.060 mrad. These measurements are performed by the beam spectrometer GTK (section 2.5) and the downstream spectrometer STRAW (section 2.8).

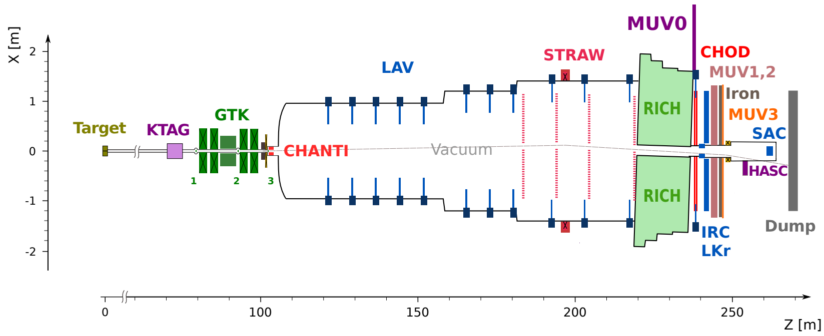

FIGURE 2.2: Schematic horizontal view of the NA62 beamline and detector [108]. The intense flux of beam particles from the target, shown with the dashed grey line, passes through an evacuated passage without interacting with detectors before the beam dump. The kaon decays are detected inside a 65 m long decay region located inside the vacuum tank.

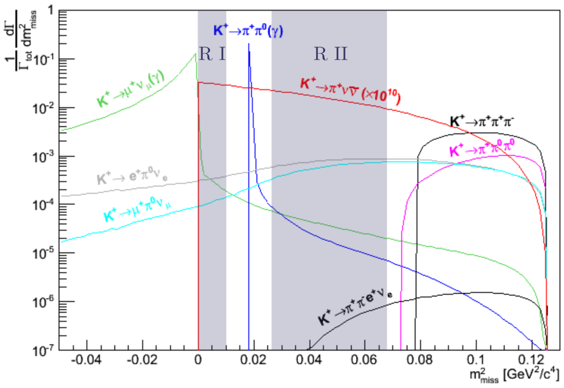

FIGURE 2.3: Distribution of the squared missing mass m^2_{miss} assuming the decay particle is a pion for all kaon decay modes on a logarithmic scale [108]. The two $K^+ \rightarrow \pi^+\nu\bar{\nu}$ signal regions are highlighted with shaded areas. Note that the $K^+ \rightarrow \pi^+\nu\bar{\nu}$ contribution is enhanced by a factor of 10.

Particle identification (PID) in NA62 plays a vital role in tagging incoming kaons and separating the signal from other kaon decays with a single track in the final state. The PID system is represented by the kaon identifying detector KTAG (section 2.4) and the RICH detector used to discriminate between pions and other charged particles, particularly muons and electrons (section 2.9). Additional information is given by the Liquid Krypton electromagnetic calorimeter LKr (section 2.11) and the muon veto system detectors. Muon veto consists of two hadron calorimeters, MUV1 and MUV2, and a fast muon veto MUV3 placed at the end of the beamline right after an iron wall (section 2.13). Altogether the downstream PID detectors must provide muon rejection at the level of $\mathcal{O}(10^7)$.

Furthermore, to suppress one of the main backgrounds, $K^+ \to \pi^+\pi^0$ (Fig. 2.3), NA62 must provide a hermetic coverage against photons emitted at angles from 0 to 50 mrad with a rejection factor of $\mathcal{O}(10^8)$. The photon veto system of NA62 consists of the Large Angle Veto detectors LAV (section 2.7) with angular coverage from 8.5 to 50 mrad, the LKr with coverage of $1 - 8.5$ mrad and the Small Angle Veto represented by IRC and SAC detectors with the coverage of $0 - 1$ mrad (section 2.12).

Finally, to have precise matching between the kaon track and its decay products in the high-intensity environment, time resolution between sub-detectors must be at the level of 100 ps.

In the following sections, a description of the beamline and most of the sub-detectors will be provided. The description of MUV0, HASC, MUV1 and MUV2 was omitted since these detectors were not considered in the analysis described in chapter 4; however, their detailed description can be found in the NA62 detector paper [108].

2.3 Kaon beamline

NA62 uses a primary proton beam extracted at 400 GeV/c from the CERN SPS accelerator via the P42 beamline. The proton beam is directed to the beryllium target, T10 (400 mm long, 2 mm diameter), located in a tunnel connecting the SPS to the NA62 experimental hall. Positively charged secondary particles with a central beam momentum of 75 GeV/c ($\sim$ 1 % RMS) are selected and propagated to the NA62 decay volume via the K12 beamline. The sign and the momentum choice were motivated by the kaon fraction maximisation regarding the flux of incident protons and other particles in the beam.

The K12 beam optics is schematically shown in Fig. 2.4. The length of the beamline from the T10 centre to final collimators C6 and C7 is 101.3 m.

The first beam element downstream of T10 is a 950 mm long, water-cooled, copper collimator with a set of bores of different apertures, which are used to limit the transversal size of the beam. Generally, a 15 mm diameter hole was used. This collimator is followed by a set of quadrupole magnets Q1, Q2 and Q3, which collect particles at 75 GeV/c central momentum in a large solid angle acceptance ($\pm$2.7 mrad horizontally and $\pm$1.5 mrad vertically). Right after the magnets, a front-end achromat A1 selecting particles at 75 GeV/c with a 1 % RMS is located. The achromat consists of four vertically deflecting

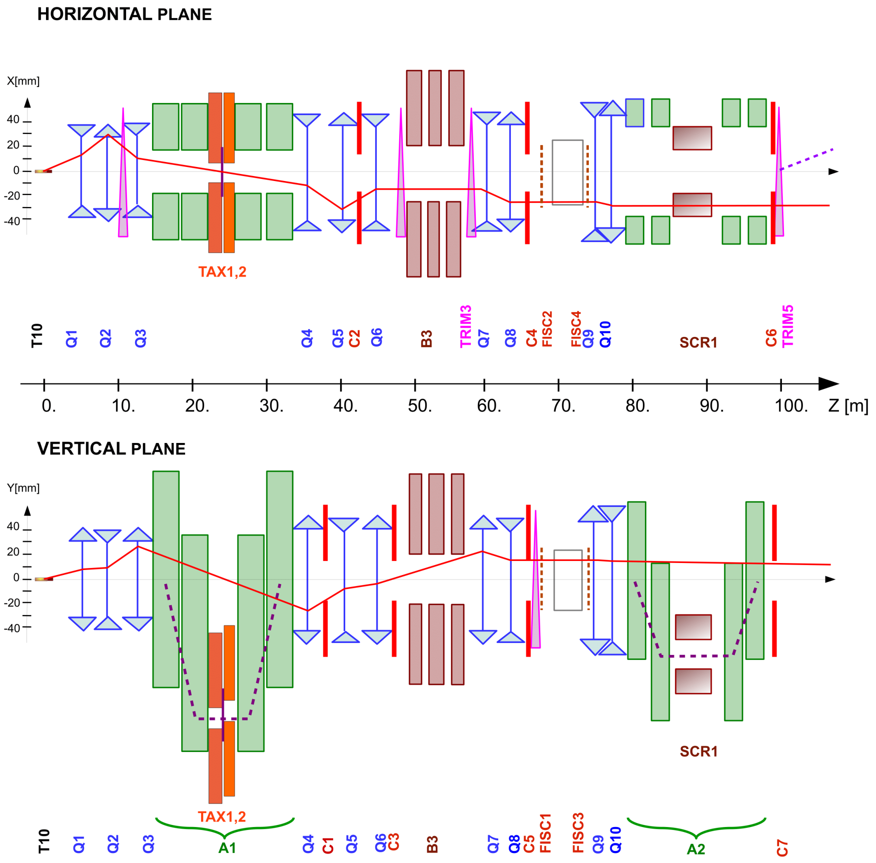

FIGURE 2.4: Schematic layout and optics of the high-intensity hadron beam from the target T10 to the entrance of the decay volume [108]. In each view, the solid red line corresponds to the path of a particle leaving the target from the centre at nominal momentum and the indicated angle. The dashed line illustrates the trajectory of an initially on-axis 75 GeV/c momentum particle.

dipole magnets. The first pair displaces the beam vertically by 110 mm, and the last returns it to the original axis. Between the A1 magnets, the beam passes through apertures in two motorised water-cooled beam-dump modules, TAX1 (copper) and TAX2 (iron). The TAX absorbs unwanted secondary particles and remaining primary protons and adjust the secondary beam intensity. Notably, the TAX can be closed completely, letting NA62 operate in the beam-dump mode.

The achromat A1 is followed by the quadrupoles Q4, Q5 and Q6. These magnets refocus the beam in the vertical plane and make it parallel with limited width in the horizontal plane. The triplet of quadrupoles is intercepted by three acceptance redefining collimators, C1 (vertical), C2 (horizontal) and C3. The collimators prepare the beam to pass through a 40 mm diameter bores of the three following dipole magnets B3, 2 m long each. The dipole magnets sweep away the muons of both signs. The beam deviation caused by the small stray field inside the bores is cancelled by two steering dipoles TRIM2 and TRIM3, placed before and after the B3 magnets.

A differential Cerenkov detector CEDAR (shown as a blue rectangular located between the scintillator counters FISC1(2) and FISC3(4) on the vertical (horizontal) view of Fig. 2.4) is equipped with eight arrays of photodetectors (KTAG) to tag the kaons in the beam (section 2.4). The optimal detector operation requires the beam to be parallel. For this reason, the CEDAR is preceded by quadrupoles Q7 and Q8. In addition, the horizontal and vertical collimators C4 and C5 located after the quadrupoles absorb particles in the tails of the beam.

After passing the CEDAR, the beam is focused by a pair of quadrupoles, Q9 and Q10, onto the beam tracking system GigaTracKer (section 2.5). The GigaTracKer (GTK) consists of three silicon stations installed in the beam vacuum. The space between the first and the last stations is occupied by a second achromat A2, which comprises four magnets vertically deflecting the beam. Right before the second station, there is a magnetised iron collimator SCR1, which, together with the yokes of the third and fourth magnets, defocuses muons. The last magnets of A2 are followed by the two collimators, C6 and C7, which main task is to remove particles outside the beam acceptance. In 2018, the C6 and C7 collimators were replaced with a single large one due to the insufficient suppression of the upstream decays observed in $K^+ \to \pi^+ \nu \bar{\nu}$ analysis. Finally, right before the last station of GTK, there is a horizontal steering magnet TRIM5. The TRIM5 deflects the beam by $+1.2$ mrad towards positive X to compensate for the following bent of the downstream magnet MNP33 (-3.6 mrad towards negative X) and let the un-decayed beam particles pass through the central aperture of the LKr calorimeter and subsequent detectors (see Fig. 2.5).

Few meters after the last GTK station, the NA62 decay region starts (see Fig. 2.5). This region is located inside a large 117 m vacuum tank ($\sim 10^{-6}$ mbar) made of steel or stainless steel. The tank hosts 11 large angle veto (LAV) detectors (section 2.7) and four chambers of the downstream spectrometer STRAW (section 2.8). The residual magnetic field inside the decay volume, which can affect trajectories of passing particles, was precisely measured [119]. The vacuum tank is closed off at its downstream end by a 2 mm thick aluminium window, separating the tank from the neon gas of the RICH counter. Finally, after being deflected by the BEND magnet placed after the MUV3 detector, the beam is sent to the beam dump.

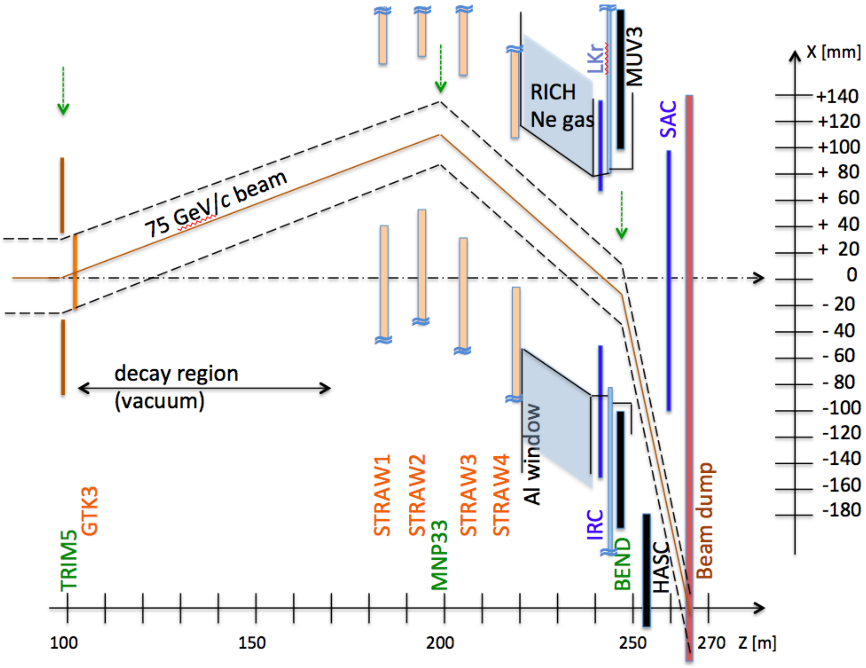

FIGURE 2.5: Schematic drawing of the K12 beamline from the decay volume to the beam dump in (X, Z) plane [108]. At the entrance of the decay region, the beam has a horizontal angle of $+1.2$ mrad. The spectrometer magnet MNP33 deflects the beam by -3.6 mrad to match the central aperture of the LKr calorimeter. After MUV3, the dipole magnet BEND diverts charged particles associated with the beam away from the SAC, sending them into the beam dump. The solid (dashed) lines correspond to the mean (two sigma width) of the beam profile. The vertical green arrows indicate the bending centre of each magnet.

Several important design characteristics of the kaon beam are shown in Tab. 2.1. The spill length is a duration of proton beam extraction with an effective length of about 3 s; it will be referred to as a burst later on. The spill cycle is the time between two extractions, which is about 10 s on average.

SPS spill length (s) / SPS cycle time (s)		0.3
Effective SPS duty cycle (s/s)		~ 0.2
SPS protons per pulse of 3 s		3.3×10^{12}
Instantaneous beam rates	protons	173 MHz (23 %)
	K^+	45 MHz (6 %)
	π^+	525 MHz (70 %)
	μ^+	~ 5 MHz ($< 1\%$)
	Total	750 MHz (100%)

TABLE 2.1: Parameters of the high-intensity K12 beam at nominal intensity [108].

2.4 Kaon tagging detector KTAG

The kaon tagging detector of NA62 is based on a differential Cherenkov counter with achromatic ring focusing, CEDAR. CEDAR detectors are widely used to discriminate kaons, pions and protons in unseparated beams extracted from the CERN SPS.

In NA62, CEDAR has a 0.94 m^3 vessel filled with nitrogen (N_2) at 1.75 bar at room temperature with a total material thickness along the beam of $3.5 \times 10^{-2}\ X_0$. In addition, the detector can also be filled with hydrogen (H_2) at 3.9 bar, which reduces the material thickness to $7 \times 10^{-3}\ X_0$. The pressure in the vessel was chosen in such a way that only light produced by kaons can pass through an annular diaphragm of fixed central radius and varying radial aperture.

Even though the optics and the gas volume of CEDAR suit the needs of NA62, the original photodetection system and the readout electronics could not sustain the 45 MHz kaon rate with the time resolution of $\mathcal{O}(100)$ ps. Thus, the KTAG detector was developed to meet the requirements. With the new design, after exiting the CEDAR vessel, the light is passing through eight quartz windows and gets reflected radially outwards by eight spherical mirrors into eight lightboxes. Each lightbox, also called a sector, is equipped with 48 Hamamatsu photomultipliers placed at the end of light guiding cones. The schematic drawing of the KTAG optics and mechanics is shown in Fig. 2.6 left. Fig. 2.6 right demonstrates a photo of the KTAG installed in the NA62 beamline.

According to the analysis of data collected in 2015, the coincidence in at least five sectors ensures the presence of kaon with 98% efficiency with kaon-pion misidentification at the level of $\mathcal{O}(10^{-4})$. Furthermore, the time resolution of the kaon tagging system was found to be 70 ps.

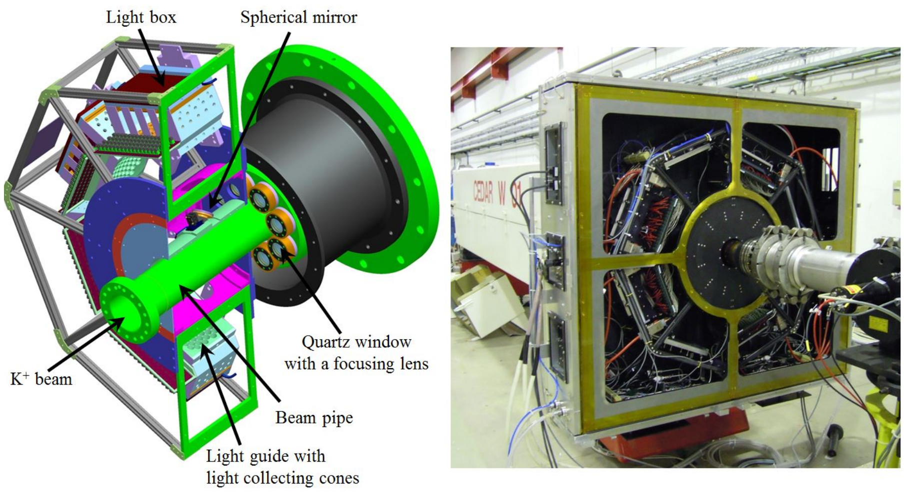

FIGURE 2.6: Left: Drawing of the upstream part of the CEDAR with the KTAG. Right: The KTAG (the squared box) and CEDAR detectors installed in the NA62 beamline during a test run in 2012 with four out of eight KTAG sectors present [108].

2.5 Beam tracking system GigaTracKer (GTK)

The beam tracking spectrometer GigaTracKer (GTK) measures the momentum, direction and time of the incoming beam particles.

GTK was designed and built to fulfil a number of challenging specifications.

- The GTK must provide the angular and momentum resolution of $p_{x,y}/p_z =$ 16 μrad and $\delta p/p = 0.2\%$. This requirement and the limitation on the number of inelastically scattered beam particles restrict the material budget of the whole detector to 1.5% X_0.
- The GTK has to have a hit time resolution better than 200 ps to unambiguously reconstruct and associate a beam track with signals in other subdetectors.
- All constraints mentioned above must be satisfied despite the beam irradiation amounting to a yearly fluence of 4.5×10^{14} 1MeV $n_{eq}/\text{cm}^2/200$ days.

GTK is made of three stations placed inside the achromat A2 (Fig. 2.7). Each station consists of an assembly of a hybrid pixel detector and a cooling plate inserted into the countersink of the carrier board. The carrier board is mounted into the vacuum vessel flange, which is used to fix the station in the beam pipe of the experiment. The top and bottom views of the GTK assembly are shown in Fig. 2.8.

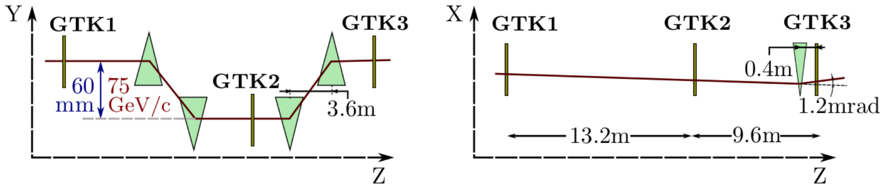

FIGURE 2.7: Schematic layout of the GTK stations within the achromat A2 in vertical and horizontal views [108]. The green triangles in the YZ view correspond to the magnets of A2, while in XZ, it indicates the TRIM5. The beam is deflected vertically by 60 mm and then returned to its nominal direction to allow the momentum measurement.

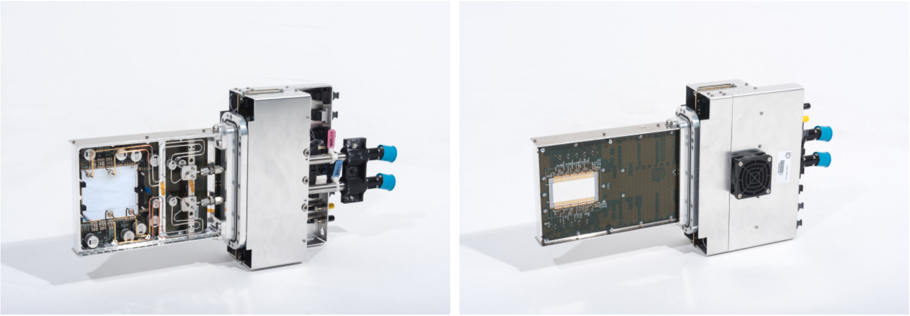

(A) (B)

FIGURE 2.8: Photograph of the GTK assembly from the cooling plate side (A) and the sensor side (B) [108].

The 60.8×27 mm^2 sensitive part of the detector is made of 200 μm thick silicon with the resistivity of ≥ 3 kΩcm. The sensor is segmented into 18000 pixels of 300×300 μm^2 size and readout by two rows of five custom made ASICs, the TDCpix [120] thinned to 100 μm (0.1% X_0). Each chip bump-bonded on the sensor is serving 40×45 pixels. In order to protect from single event upsets caused by the radiation, the internal logic of TDCpix was triplicated. Since the chip power consumption is about 4 W per chip and the detector is placed in a vacuum, active cooling was required.

The GTK cooling plate is the first application of a microchannel cooling system in high energy physics [121]. The cooling device is a 70×80 mm^2 silicon plate fabricated by bonding silicon wafers together. The plate is etched to have 150 micro-channels with a cross-section of 200×70 μm^2 through which a liquid coolant C_6F_{14} flows at 3 g/s keeping the sensor and the front-end electronics at less than 5°C. The cooling plate thickness was minimised to 210 μm (0.2% X_0) in order to meet the design requirements.

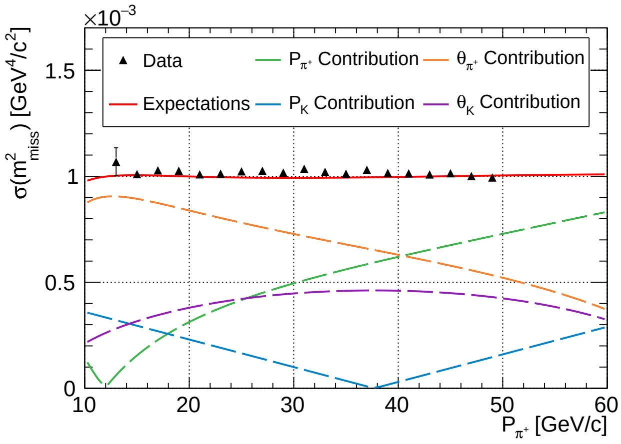

FIGURE 2.9: Squared missing mass resolution measured with $K^+ \to \pi^+\pi^0$ decays as a function of the pion momentum for the 2016 data (black triangles) compared to the expected performance (solid red line) [122].

The detector performances measured with the data collected in 2016 and 2017 show that the GTK achieved the track time resolution of 65 ps with a single hit time resolution of 115 ps surpassing the design requirements [122]. In addition, the kinematic performance was found to be matching the specifications (see Fig. 2.9).

2.6 CHANTI

Despite the reduced material budget, the GTK still can be a source of inelastic interactions, the most critical of which happen in the last station, GTK3. Charged particles created in such interactions can mimic the $K^+ \to \pi^+\nu\bar{\nu}$ signal if they reach the downstream spectrometer. While most of the particles produced in the two upstream stations, GTK1 and GTK2, are swept away by the GTK magnets, events occurring in GTK3 are rejected with the help of the CHANTI detector. In addition to the products of inelastic processes in GTK3, the detector can also tag halo muons close to the beamline and a fraction of charged particles produced upstream of GTK3.

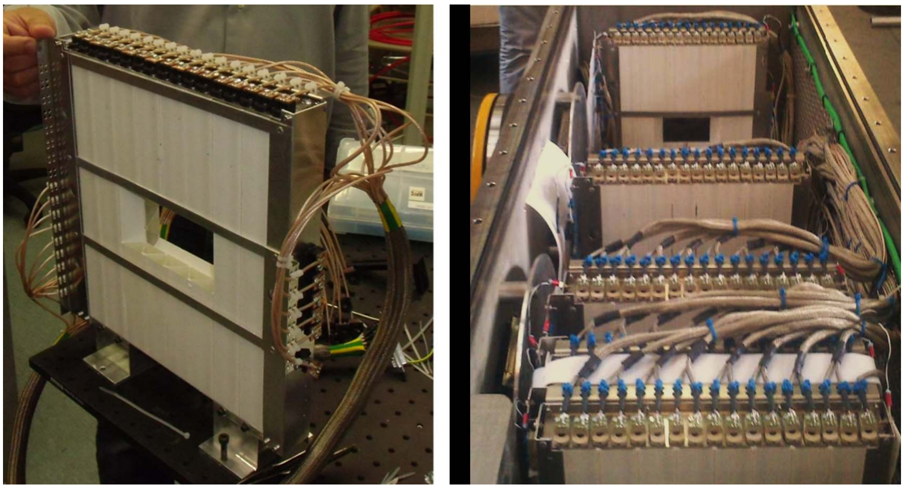

FIGURE 2.10: Left: Photo of a single CHANTI station. Right: View of the upstream part of the CHANTI vacuum vessel with the first five stations installed [108].

The CHANTI detector is made of six square scintillator stations with an area of 300×300 mm^2 and a central hole of 95×65 mm^2 to allow the passage of the beam pipe. The stations are placed inside the GTK3 vessel. The distance between each station and the next one is doubled along the beam direction to provide angular coverage starting from 49 mrad and up to 1.34 rad. Fig. 2.10 right shows one of the CHANTI stations, while on the left picture the placement of the first five stations inside the vessel is demonstrated.

Each station comprises 48 triangular scintillator bars readout with the fast wavelength-shifting (WLS) fibres coupled to silicon photomultipliers (SiPMs). The bars in each station are arranged into two planes oriented in X and Y directions.

The detector performances measured with data collected in 2015 in dedicated muon runs demonstrate uniform efficiency above 99% for each view of each station. The time and the spatial resolutions were reported to be about 830 ps and 2.5 mm, respectively.[9]

2.7 Large Angle Veto (LAV)

The Large Angle Veto detector (LAV) is a part of the NA62 photon veto system, aiming to provide hermetic coverage for photons produced inside the decay volume. The detector is made of 12 ring-shaped stations, 11 of which surround

---

[9] More detailed information about CHANTI can be found in [123].

the vacuum tank. The last station placed about 3 m upstream the Liquid Krypton calorimeter (section 2.11) operates in the air. LAV provides full geometric coverage for photons emitted from within the decay volume at angles from 8.5 to 50 mrad. By design, the detector is required to register low energy photons (below 200 MeV) with an inefficiency lower than 10^{-4}.

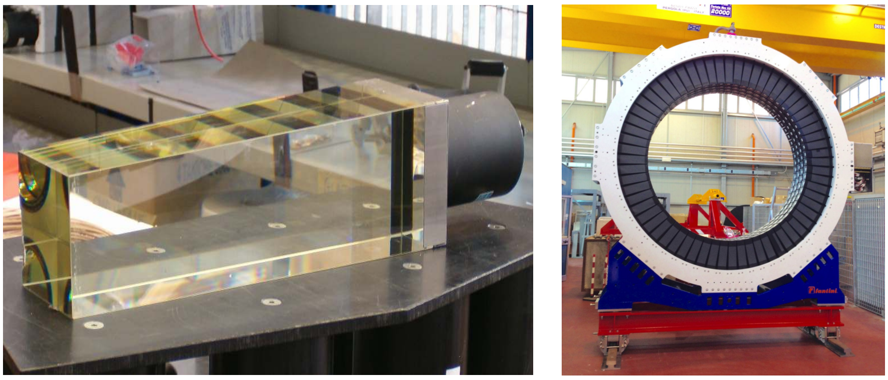
(A) (B)

FIGURE 2.11: (A) LAV lead-glass block without wrapping. These blocks were previously used in the OPAL calorimeter. (B) Completed LAV station before insertion in the beamline. Both pictures are taken from [108].

The LAV detector uses lead-glass blocks from the OPAL electromagnetic calorimeter (Fig. 2.11A). The blocks are made of 75% lead oxide PbO by weight with a radiation length of $X_0 = 1.50$ cm and refraction index $n \approx 1.85$ at $\lambda = 550$ nm and $n \approx 1.91$ at $\lambda = 400$ nm. Photons produced in the electromagnetic showers inside the block are detected by collecting the Cherenkov light. Signals from lead glass blocks are read out at the backside by a Hamamatsu photomultiplier optically coupled via a 4 cm long light guide.

Each LAV station is made by arranging blocks in multiple inward facing rings like in Fig. 2.11B. As a result, at any angle, particles cross at least three LAV rings ($\geqslant 21\ X_0$).

Analysis of data collected in 2015 showed that the LAV time resolution for 1 GeV photons is on the level of 1 ns for all stations.

2.8 STRAW spectrometer

The STRAW spectrometer measures the momenta and the direction of the tracks downstream the decay volume. The detector consists of four straw chambers separated by a large aperture dipole magnet MNP33 providing an integrated field of 0.9 Tm. The chambers are made of light material (1.8 X_0 in total) and placed inside the vacuum tank to minimise the multiple scattering.

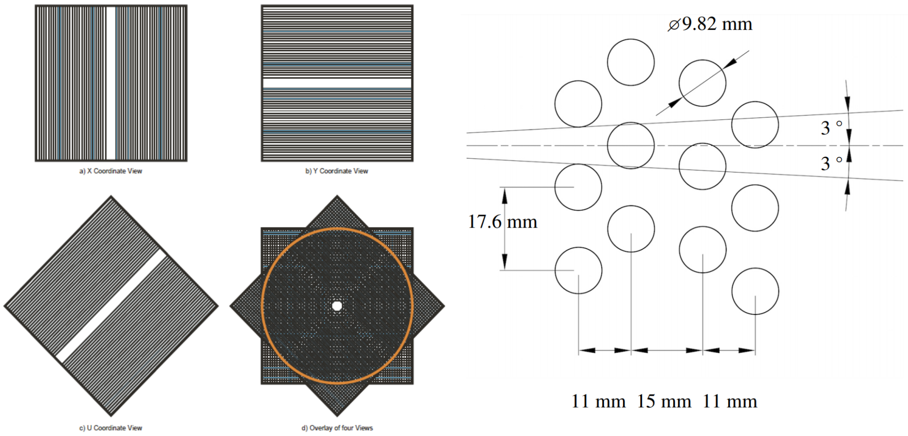

(A)

(B)

FIGURE 2.12: (A) One STRAW chamber composed of four views: X, Y, U, and V. In the middle of each view, a few straws are removed to create a passage for the beam pipe. (B) Straw geometry inside one view. It is based on two double layers with sufficient overlap to guarantee at least two straws to be crossed per view per track. Figures are taken from [108].

STRAW chambers are composed of two modules, where one of the modules contains views X (0°), Y (+90°) and the other U (−45°) and V (+45°). Each view has a $\sim$ 12 cm gap, such that the assembled chamber has an octagon-shaped hole 6 cm apothem for the beam pipe. The schematic drawing of the STRAW chamber is shown in Fig. 2.12 left along with the highlighted circular active area, 2.1 m in diameter.

Each chamber contains 1792 straws of 9.82 mm diameter and 2160 mm length. Each view contains the straw tubes arranged into four layers, as shown in Fig. 2.12. This configuration ensures the presence of at least two hits per view and $8 - 12$ hits per track per chamber. The straws are made from 36 μm thick polyethylene terephthalate (PET), coated with 50 nm of copper and 20 nm of gold on the inside. The 30 μm anode wires inside the straw tubes are made from the gold-plated tungsten and tensioned at 80 g. The tubes are filled with a mixture of 70% Ar and 30% CO_2 at atmospheric pressure.

The performances of the STRAW spectrometer measured with data collected in 2015 are in agreement with the design specifications. The track momentum resolution was found to be consistent with:

$$\frac{\sigma(p)}{p} = 0.30\% \oplus 0.005\% \cdot p \tag{2.5}$$

where p is in GeV/c. The angular resolution decreases from 60 μrad at 10 GeV/c to 20 μrad at 50 GeV/c.

2.9 RICH

The NA62 Ring Imaging Cherenkov detector (RICH) is designed to separate pions from muons in the momentum range from 15 to 35 GeV/c. The detector shown in Fig. 2.13 has a 17.5 m long cylindrical vessel filled with neon gas at 990 mbar. The vessel is built of four sections of gradually decreasing diameter and different lengths. A lightweight aluminium beam pipe passes centrally through the detector.

The upstream section of the radiator vessel is $\sim$ 4.2 m wide. The section hosts two photomultiplier flanges with 976 Hamamatsu PMs at each side. The last vessel element is 3.2 m and contains the mirror mosaic with 18 hexagonal and two semi-hexagonal spherical mirrors. The mosaic is divided into two spherical surfaces – one with the centre of curvature reflecting light to the left and another to the right of the beam pipe.

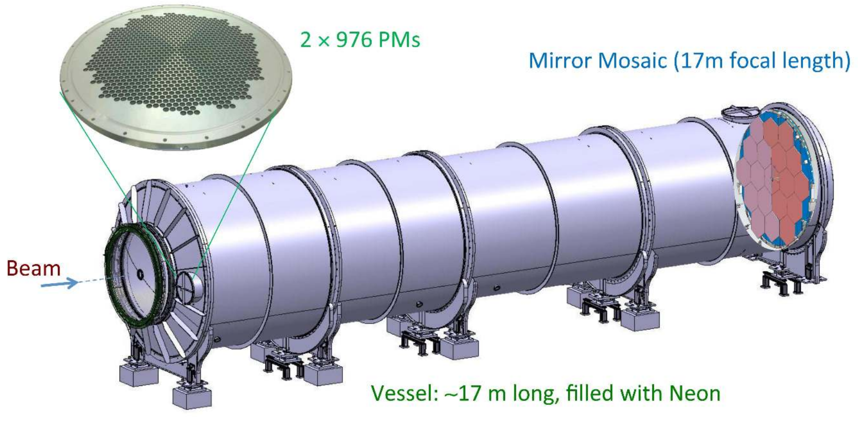

FIGURE 2.13: Schematic view of the RICH detector [108]. The hadron beam shown with the blue arrow travels throughout the detector in an evacuated beam pipe. A zoom on one of the two disks hosting the photomultipliers (PMs) is displayed on the left. The mirror mosaic can be seen on the right.

The intrinsic time resolution of the RICH detector was measured to be about 70 ps, while the pion identification efficiency was found to be at the level of 80% with the muon suppression factor of 10^2.

2.10 Charged particle hodoscopes

The NA62 detector setup includes two scintillator counters called Charged Hodoscopes (CHOD), responsible for the charged particles detection. One of the counters is the NA48 CHOD detector used in the former kaon experiment NA48, and another one is a newly constructed counter adapted for the high-intensity environment of NA62. The NA48 CHOD is placed right after the twelfth station of the LAV, LAV12, while CHOD is placed upstream LAV12.

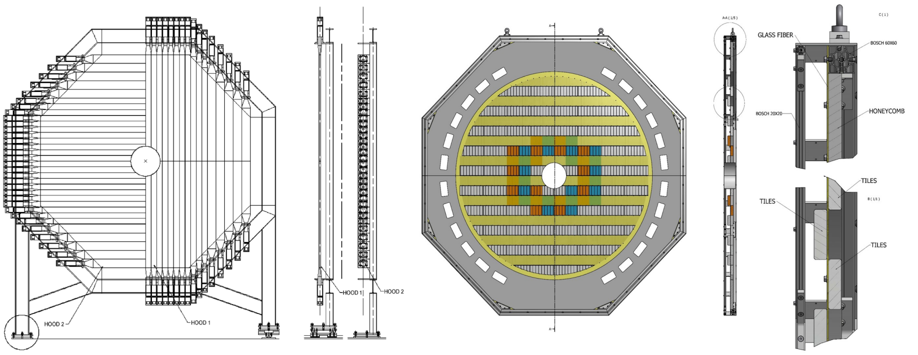

(A) (B)

FIGURE 2.14: (A) Front and side views of the NA48 CHOD detector. Half sections of the horizontal and vertical planes are shown. (B) Front and side views of the CHOD detector. The 152 scintillator tiles are mounted front and back of a thin support panel ((B) bottom right). The structure is stiffened at the periphery with honeycomb and aluminium construction profiles ((B) top right). Pictures taken from [108].

Hodoscope CHOD

The CHOD active area comprises 152 plastic scintillator tiles of 30 mm thickness, covering an area with a radius of 1070 mm (Fig. 2.14B). The central part of the detector has a circular hole with a radius of 140 mm to fit the beam pipe. The scintillator tiles are mounted on the front and back sides of the support panel with a 1 mm overlap. The tiles are 108 mm high (except for 12 tiles near the external edge) and 268 mm wide (tiles near the beam pipe are 134 mm). The light produced in the scintillator is collected and transmitted by length shifting fibres (1 mm diameter Kuraray) to a 3×3 mm^2 SensL SiPMs (four fibres for one SiPM).

The CHOD time resolution is about 1 ns.

NA48 hodoscope NA48 CHOD

The NA48 CHOD is made of two planes made of 64 vertical and 64 horizontal plastic scintillator slabs 20 mm thick. Each slab is read out from one side by a PHOTONICS photomultiplier. The slabs are arranged into four quadrants of 16 slabs, each with a total octagonal sensitive area with an apothem of 1210 mm. As in the CHOD detector, the NA48 CHOD has a central hole with a 128 mm radius for the beam pipe. The schematic drawing of the NA48 CHOD detector is shown in Fig. 2.14A.

The time resolution of the detector is about 200 ps with inefficiency at the per mille level.

2.11 Liquid Krypton calorimeter LKr

The Liquid Krypton calorimeter LKr is an important part of the NA62 photon veto system providing angular coverage in the range of $1 - 8.5$ mrad. LKr is a quasi-homogeneous calorimeter filled with 9000 litres of liquid krypton at 120 K. It is located after charged hodoscopes. The calorimeter has a sensitive area of 128 cm in radius and 127 cm in depth (27 X_0), allowing for the full development of the electromagnetic showers. The central part has a hole for the beam pipe with a radius of 8 cm.

The active area of the calorimeter, housed inside a cryostat, is segmented into 13248 longitudinal cells with a cross-section of $\sim 2 \times 2$ cm^2. The cells are made from three zig-zag shaped $Cu - Be$ electrodes, as shown in Fig. 2.15 right, to avoid possible inefficiencies when particles shower near the anode. The anodes are connected to the high voltage of 3000 V on the downstream end, which produces the drift field. The created signals are collected by preamplifiers inside the cryostat, directly attached to the electrodes, and then sent to the transceiver boards via 50 Ω coaxial cables.

Since the detector was previously used in the NA48 experiment, external components of its cryogenic system and auxiliary parts of the readout system were renewed. The readout system was entirely replaced in order to satisfy the beam rate of NA62.

An estimation of the LKr energy resolution in NA62 using simulation is [108]

$$\frac{\sigma(E)}{E} = \frac{4.8\%}{\sqrt{E}} \oplus \frac{11\%}{E} \oplus 0.9\% \tag{2.6}$$

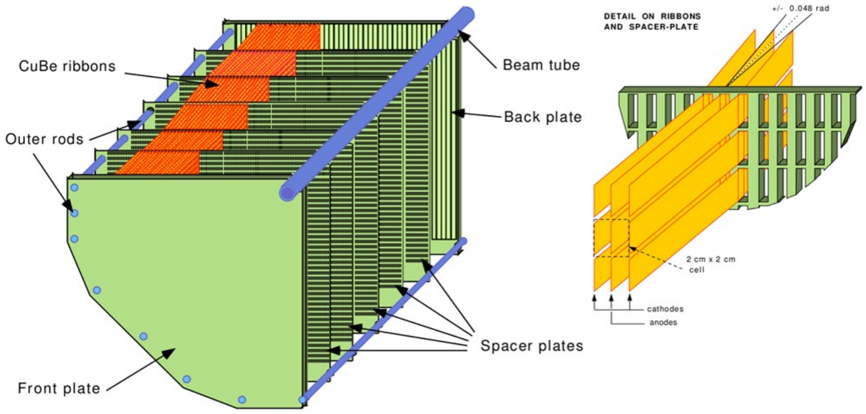

FIGURE 2.15: Left: Schematic structure of one LKr quadrant. Right: Detailed scheme of the calorimeter cells with the zig-zag electrodes shown. Pictures taken from [108].

where the energy E is measured in GeV. The NA48 CHOD-LKr time resolution was found to be about 550 ps.

2.12 Small Angle Veto

The Small Angle Veto (SAV) detectors cover angles from 0 to 1 mrad finalising the hermetic coverage of the NA62 photon veto system. The SAV system consists of two shashlyk-type calorimeters: the Small-Angle Calorimeter (SAC) and the Intermediate-Ring Calorimeter (IRC).

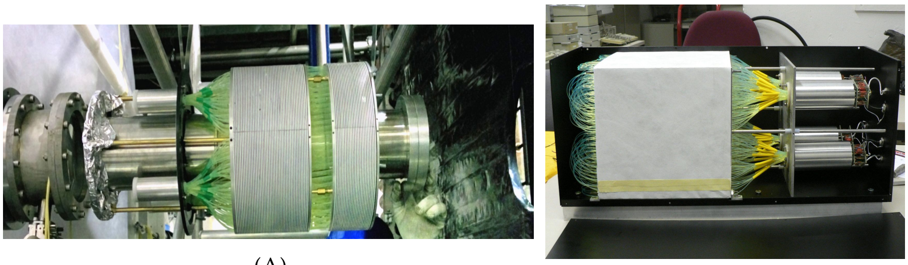
(A)

(B)

FIGURE 2.16: (A) Picture of the IRC detector. The two detector modules are visible; the beam direction here is from the right. (B) Picture of the SAC detector after completion of assembly. Photos taken from [108].

Intermediate-Ring Calorimeter (IRC)

The Intermediate-Ring Calorimeter (IRC), placed upstream LKr, has an eccentric cylindrical shape with an outer radius of 290 mm and an inners radius of 120 mm for the beam pipe. The detector is shifted by 12 mm in the positive X direction to account for the beam deflection by the MNP33 magnet. The calorimeter is divided into two modules with a depth of 89 mm upstream and 154 mm downstream (Fig. 2.16A). The distance between the two modules is 40 mm. The upstream and downstream modules consist of 25 and 45 ring-shaped layers. Each layer is made of a 1.5 mm thick lead absorber (97% lead, 3% antimony alloy) and a 1.5 mm thick scintillator plate, amounting to a total interaction length of 19 X_0. The light produced in scintillators is read out by 1.2 mm wavelength-shifting fibres traversing both modules. The upstream ends of the fibres are covered with black paper, and on the downstream side, the fibres are read out by four Hamamatsu photomultipliers. The detector is covered with black paper to protect it from other possible light sources.

Small-Angle Calorimeter (SAC)

The SAC calorimeter, placed at the very end of the beamline, comprises 70 plates of lead and 70 plates of scintillator. The transverse size of the SAC is 205×205 mm^2, and it has a thickness of 1.5 mm amounting to the total depth of 19 X_0. Each plate has a grid of 1.5 mm diameter holes with 9.5 mm spacing, 484 holes per plane in total. The plates are stacked together with Tyvek sheets between the lead and scintillator layers. Wavelength-shifting fibres (240 in total) traverse the stacked plates through two holes, forming a U shape as shown in Fig. 2.16B. Four Hamamatsu PMs read out the fibre ends.

The SAC energy resolution is

$$\frac{\sigma(E)}{E} = \frac{8.8\%}{\sqrt{E}} \oplus \frac{7.1\%}{E} \tag{2.7}$$

where energy is in GeV. The inefficiency for detecting 600 MeV electrons was measured to be less than 5×10^{-3}.

The total SAV mistagging probability was found to be 7×10^{-4} with a time resolution of 1 ns.

2.13 Muon Veto (MUV3)

The muon veto counter MUV3 is located behind an 800 mm thick iron wall close to the final beam dump. The MUV3 detects charged particles that travelled a total thickness of 14 interaction lengths, improving π/μ separation in addition to the RICH. The total sensitive area of MUV3 is 2640×2640 mm^2. The detector is made of 50 mm thick scintillator tiles, 140 of which are 220 × 220 mm^2, the other 8, which surround the beampipe, have smaller sizes. Each tile is covered with an aluminised Mylar foil on the front and lateral sides. The signal produced in the tile is read out by two photomultipliers placed on its backside.

The time resolution of the MUV3 detector was found to be 600 ps, while the muon detection efficiency is at the level of 99.5% for muons with momenta higher than 15 GeV/c.

2.14 Trigger and Data Acquisition system (TDAQ)

In order to cope with high intensity, NA62 uses three trigger levels – hardware Level-0 (L0), software Level-1 (L1) and Level-2 (L2). By design, the decay rate of 10 MHz at nominal intensity has to be reduced first by L0 trigger down to $\sim$ 1 MHz and then by L1 and L2 to $\sim$ 10 kHz, ensuring bandwidth availability for data storage to tape. The schematic overview of the NA62 Trigger and Data Acquisition system is displayed in Fig. 2.17.

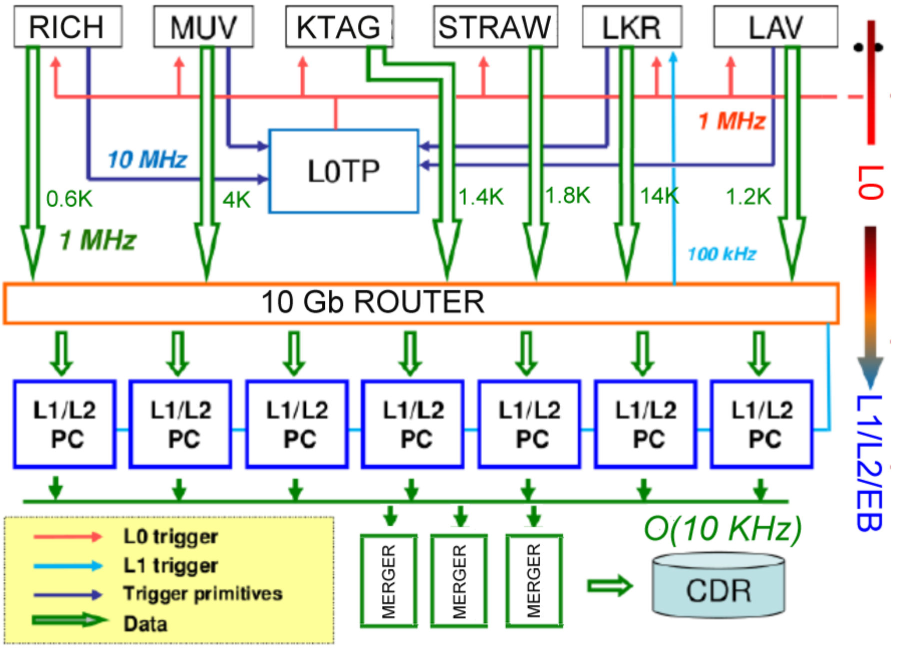

FIGURE 2.17: Overview of the NA62 Trigger and Data Acquisition system. Numbers near the data arrows correspond to the average data size in byte. Note that only a few detectors are displayed for the sake of simplicity [108].

Unlike LHC, the SPS beam structure is expected to be uniform in rate for about 3 seconds long machine burst. Each burst is separated from the next one by a variable time (up to a minute). Due to this separation, a single burst became the unit of data-taking in NA62. Thus, all electronic devices are running in a fully synchronised way during the burst, and outside the burst, everything resets to the initial state.

All synchronous elements of the NA62 TDAQ system run on the centrally distributed clock delivered via the Timing, Trigger and Control (TTC) system. The TTC is a unidirectional transmission system based on optical fibre. The system has two multiplexed channels encoded using a 40 MHz clock and transmitted at a 160 MHz rate. The Start of Burst (SOB) command sent via TTC about 1 s before the first beam particles are delivered identifies the start of time measurements for the current burst. Similarly, the End of Burst (EOB) signal, sent at the end of the burst signalises all systems to stop.

Most of the NA62 detectors (all except trackers and calorimeters) are equipped with a TDC-based[10] TDAQ system, TEL62. The TEL62 is a 9U-size board, which was redesigned from the TEL1 board developed for the LHCb experiment. Each TEL62 board has four identical FPGA-controlled 640 MB/s input data channels with up to 2 GB random access memory RAM (DDR2).[11] In addition, the TEL62 is equipped with 4 GbE ports, which are used to send trigger information outside the board. The TEL62 can hosts up to four high precision TDC board (TDCB) mezzanine cards. Each TDCB can digitise leading and trailing edge times of 128 detector channels delivered as LVDS signals. The time resolution provided by the TDCB is measured to be 100 ps.

The GigaTracKer off-chip readout system is made of custom build modules called GTK-RO boards, which serve as an interface between on-chip readout TDCpix and TTC clock and trigger. The two decked cards centred around an FPGA comprise each of the GTK-RO boards. The main card has four 3.2 Gb/s optical links, one 320 Mbit/s optical link and 2 GbE copper links, where each of the four-gigabit optical links serves one-quarter of TDCpix. The total GTK readout data bandwidth is 128 Gb/s per station or 12.8 Gb/s per chip. The data transferred from TDCpix is stored in the large onboard memory of GTK-RO. After receiving the L0 trigger with a fixed latency, three time slots centred around L0 time (75 ns) are read out from memory and then transmitted to the six sub-detector computers (PC), each serving five chips through Gigabit Ethernet switches. On the PCs, the data is organised and identified by the L0 triggers and then sent to the dedicated PCs, called PC farm, upon receiving the L1 trigger.

---

[10] TDC stands for the time-to-digital converter.

[11] FPGA stands for the field-programmable gate array.

The STRAW on-detector readout board consist of an eight-channel analogue front-end chip serving eight straws and a TDC. The on-detector readout is connected to the Straw Readout Board (SRB) via Ethernet cable. Each SRB serves up to 16 on-detector boards, and eight SRBs serve each STRAW view. The STRAW readout sends the data to the PC farm upon receiving the L0 trigger.

The Calorimeter Readout Module (CREAM) was developed specifically for the LKr calorimeter; however, it is also used for MUV1,2 calorimeters and SAV detectors. The CREAM module is a 6U VME 64 board equipped with large DDR3 memory for storing data of the complete burst, 14 bit, serial output 40 MHz FADCs and an FPGA for handling the data and trigger requests. The full data from CREAMs is sent upon receiving the L1 trigger; however, every 25 ns, the sum of the digitised signals is sent from CREAM to the Cal-L0 system. The Cal-L0 is composed of 37 TEL62 boards and 111 mezzanine cards for data transfer. The system reconstructs clusters, computes their energies and generates trigger primitives.

L0 triggers

The L0 trigger is based on inputs from a small set of fast detectors with a maximum latency of 1 ms. All trigger primitives generated by detector readout boards are sent to the Level-0 Trigger Processor (L0TP), which responsibility is to sort them in time and find matches with any active predefined trigger masks. A programmable downscaling factor to the L0 trigger generation can be applied if a trigger mask is satisfied. After the L0 trigger is issued, the recorded data is sent to the PC farm to be further processed by the High-Level Trigger algorithms L1 and L2.

The following detectors are used in the L0 trigger: RICH, CHOD, LKr and MUV3.

L1 and L2 triggers

The NA62 experiment uses two levels of software trigger – L1 and L2. The Level-1 trigger reduces data rate from 1 MHz to 100 kHz using algorithms based on various standalone detectors such as STRAW, KTAG and LAV. The Level-2 trigger reduces data even more to the level of $\mathcal{O}(10\text{kHz})$. The trigger is based on partially reconstructed events and exploits correlations between several detectors. Both trigger levels run on the NA62 PC farm. Notably, even though the infrastructure for L2 is in place, no L2 algorithm has been applied so far.

2.15 The NA62 Framework

The NA62 Framework [124, 125] was developed by the NA62 Collaboration for Monte Carlo (MC) simulations, data reconstruction and analysis. The Framework, written mainly in `C++`, `Python` and `Fortran`, employs various packages widely used in the physics community as `ROOT` [126] and `Geant4` [127, 128, 129]. The NA62 Framework consists of four main parts.

- **NA62Tools** contains the base classes and necessary configuration files mainly for MC and reconstruction.
- **NA62MC** is responsible for detector and physics simulation. Models of each detector are implemented using `Geant4`. The physics decays are simulated as follows. First, the kinematics of the primary particle is generated. In the case of kaons or pions, the particle's momentum, direction, and position at the KTAG front plane are obtained with the dedicated beam simulation `Turtle` [130]. The same can be done using the output of the NA62 beamline simulation in `BDSIM` [131] or `G4Beamline` [132] packages. The case of Beyond the Standard Model generators will be described in chapter 4 in more detail, but, in short, the kinematics of the primary particle is obtained from the pre-evaluated distributions. Then, if the forced decay was requested, the kinematics of the selected mode is computed with the help of some physics model. Otherwise, decays are generated by `Geant4`. The obtained daughter particles are then sent to the `Geant4` simulation of the NA62 apparatus, where their interactions and propagation are handled.
- **NA62Reco** provides tools for reconstructing both raw data and MC. For MC, there are two modes available: standard and overlay. In the case of an overlay, multiple raw MC outputs are reconstructed simultaneously, accounting for the emulated beam intensity. Typically, the main reconstructed decay mode is superimposed with muons from the beam halo, pions and kaons from the beam, and their decays. So far, the overlay technique provides the most precise description of the data and pileup.
- **NA62Analysis** provides a set of tools for data analysis, data quality monitoring and detector calibration. Typically, a user writes a separate analyser, which relies on already developed methods stored in the NA62Analysis.

The NA62 Framework uses the version control system, and each official release is labelled and compiled centrally. Thus, each data and MC sample has a label corresponding to the software version with which it was processed and produced. Monte Carlo samples can have two labels attached since they can be generated and reconstructed with different releases.

Analysis tools

The analysis described in chapter 4 makes use of various tools developed within the NA62 Collaboration. In this subsection, some of them will be briefly discussed.

A set of corrections is applied to some reconstructed variables before any physics selection. In particular, corrections are applied on the reconstructed track momentum and cluster energy. The momentum of each reconstructed STRAW track, P_{init}, is corrected with run-dependent α and β constants applied at the analysis level with the help of the `SpectrometerTrackCorrections` tool as:

$$P_{corr} = (1+\beta) \times (1+\alpha \cdot Q \cdot P_{init}) \times P_{init} \tag{2.8}$$

where Q is the charge of a given track.

The LKr calorimeter cluster energy is adjusted with the help of the `LKrClusterCorrections`, which relies on the π^0 mass correction method. The method relies on the reconstructed $K^+ \to \pi^+\pi^0$ decays, from which the π^0 mass is extracted and then compared with the known value.

The vertex reconstruction is made with the `SpectrometerVertexBuilder` tool based on the least-squares method, which implementation is described in detail in [133].

Additionally, each STRAW track is matched with downstream detectors with the help of geometrical propagation and timing cuts. Results of this matching can be retrieved via the standard NA62 class `DownstreamTrack`.

Pileup generators

The standard Monte Carlo reconstruction, i.e. without overlay, does not have any pileup particles included. Therefore, several tools in the NA62 Framework were developed to add (or remove) hits to the upstream and downstream detectors according to the particle rate in a given detector and its estimated inefficiency. In this thesis, two such generators are used, namely `UpstreamPileupGenerator` and `MUV3PileupGenerator`.

The `UpstreamPileupGenerator` injects hits in KTAG and GTK detectors with the rate randomly selected from the known data distribution of the instantaneous beam intensity measured with out of time GTK hits. After using the generator, a specific algorithm is needed to re-reconstruct GTK tracks to account for the simulated effect. The author of this thesis was the developer of this tool, which main task is to provide the correct set of setting for the GTK reconstruction in NA62Reco and then re-reconstruct GTK tracks.

The `MUV3PileupGenerator` adds accidental hits to MUV3 in a ±100 ns time interval in accordance with the distributions obtained from the data. More details about the generator can be found in [134].

Trigger emulators

The NA62 Framework has special tools for L0 and L1 trigger response emulation working both on MC and data. L0 trigger conditions are obtained using primitives either stored in the data or emulated with the help of registered hits. In addition, some emulators, CHOD and MUV3, can inject accidental hits from the distributions derived from the data. As for L1 triggers, the exact same online algorithms, called HLT, are executed during the data and MC reconstruction. The response of each algorithm is stored in the output and can be later read out by the user analyser. A complete description of L1 algorithms and their implementation in the NA62 Framework can be found in [135].

Chapter 3

The GigaTracKer: the NA62 beam spectrometer

Contents

3.1 Introduction

The GigaTracKer (GTK) is one of the key detectors of the NA62 experiment providing precise measurements of beam track time, momentum and direction. The required physics performances of the detector, discussed in section 2.2, limit the single hit time, track momentum and angular resolutions to 200 ps, $\delta p/p = 0.2\%$ and 16 μrad, respectively. At the same time, the detector has to face a high non-uniform beam rate of $\sim$ 1 GHz in total with a maximum of 2.0 MHz/mm^2 at the centre of the beam.[12] These requirements form a list of rather challenging detector specifications (Tab. 3.1), which can be summarised as:

- the amount of material crossed by the beam must be minimised to reduce beam interactions and scattering;
- the detector must be able to cope with a gigahertz particle rate;
- the detector must have sufficient radiation hardness.

---

[12] Rates correspond to the nominal beam intensity.

To fulfil these specifications, the GTK team used a number of cutting edge technologies in the domain of hybrid silicon pixel detectors and microchannel cooling.

Material budget per station	$\leq 0.5\%\ X_0$
Overall efficiency per station	$> 99\%$
Pixel size	$300 \times 300\ \mu\text{m}^2$
Single hit time resolution	< 200 ps RMS
Beam particle rate	750 MHz
Peak beam particle rate	2.0 MHz/mm^2
Average fluence	1.0×10^{14} 1 MeV $n_{eq}/\text{cm}^2/200$ days[13]
Peak fluence	4.5×10^{14} 1 MeV $n_{eq}/\text{cm}^2/200$ days

TABLE 3.1: GTK specifications at the nominal beam intensity [122].

As discussed in section 2.5, the GTK consists of three stations installed in the beam pipe around two pairs of bending magnets of the achromat A2 (see section 2.3). The distance between the first and the second stations is 13.2 m, while the third station is 9.6 m downstream from the second. This configuration allows for precise measurement of the direction of incoming particles. In addition, the second station is shifted downward in the vertical axis by 60 mm to measure the track momentum. The shift corresponds to a displacement of particles with a momentum of 75 GeV/c.

Each station hosts an assembly (module) of a hybrid detector and a cooling plate inserted into the carrier printed circuit board (PCB). The choice of a hybrid silicon detector was motivated by the possibility of individual optimisation of each detector component. The detector consists of a silicon sensor bonded to the ten readout chips from one side and glued to the cooling plate from the other. The chips are electrically connected to the carrier board with aluminium wire bonds to transfer power, clocks, configuration and data. The PCB is then glued into a frame and a vacuum flange. All modules are kept in vacuum (10^{-6} mbar) to minimise the interactions of beam particles.

GTK stations are equipped with an identical mechanical interface so that modules can be installed in any station and easily replaced. The latter is important since hybrid detectors need to be replaced regularly due to the permanent damages caused by the radiation. In particular, the replacement is necessary approximately every 100 days of data taking at the nominal beam intensity. Therefore, it is essential to monitor the detector data quality to maximise its lifetime and understand when the module must be removed.

---

[13] Fluence in 1 MeV n_{eq}/cm^2 is typically used as a measure of the radiation damage in silicon sensors. More details will be provided in section 3.5.

The following sections will provide a more detailed description of the sensor, on-detector readout chip TDCpix and the cooling plate.[14] Afterwards, the GTK offline time calibration, data quality monitoring, and performance during the data taking in 2017-2018 will be presented. Finally, the studies of the radiation-induced damage in the GTK modules will be discussed.

Sensor

Each GTK module is made of a large 60×27 mm^2 sensor connected via bump bonding to the two rows of five readout chips. The GTK employs planar sensor technology and operates with p- and n-type sensors, doped with boron and phosphorus, respectively.

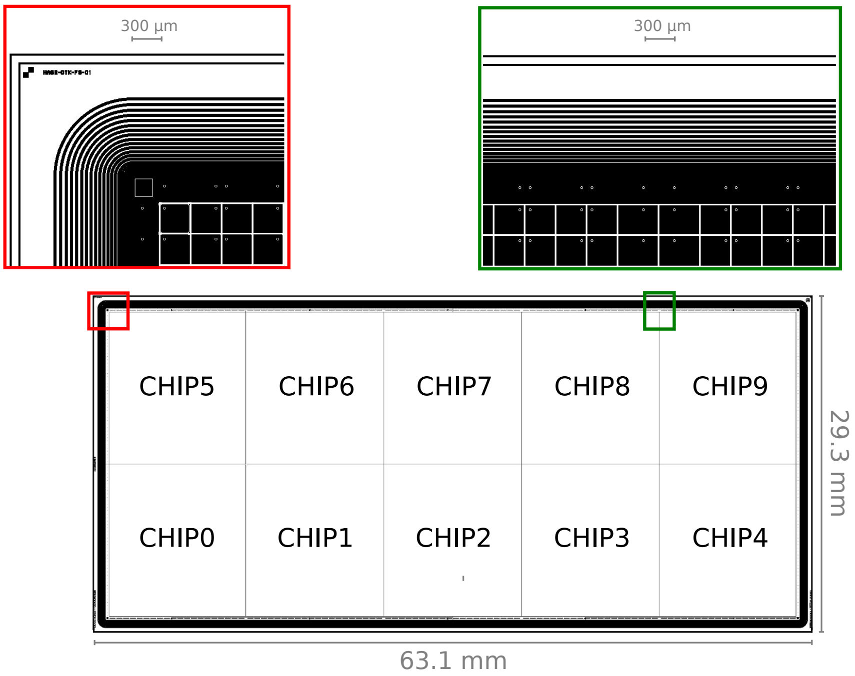

FIGURE 3.1: GTK sensor geometry. The top left zoom demonstrates the twelve sensor guard rings and the corner pixels. The top right zoom shows enlarged pixels at the chip borders; the bump bonding pads are shown as circles [122].

The choice of the sensor thickness was motivated by the material budget and the desired time resolution. A thickness of 200 μm (0.22% X_0) was found to be optimal, with a good trade-off between the requirement for the minimum

---

[14] More information about GTK can be found in [122] and its references.

material budget, fast charge collection and a sufficiently large signal for readout electronics – 15000 electron-hole pairs for a most probable charge value of 2.4 fC, corresponding to a 75 GeV/c particle.

The required time resolution is obtained by keeping the sensor highly overdepleted so that it operates close to the charge carrier saturation velocity. This approach minimises the charge collection time to $2-4$ ns [136]. An aluminium field plate was left over the edge of the implant to keep the electric field uniform in the active area. The sensor was designed with twelve guard rings to allow operation at high bias voltages and prevent surface leakage currents from extending from the sensor to pixels.

The sensor geometry is shown in Fig 3.1; the bump bonding pads can be seen as well. Notably, pixels on the chip borders are enlarged to provide additional space between bonding pads and chip borders (400×300 μm^2 instead of 300×300 μm^2).

The high-intensity environment of NA62 put a serious challenge on the sensor lifetime. Two main consequences of the radiation exposure, namely, the increase of the sensor leakage current and the reduced charge collection efficiency, can be mitigated by keeping the detector cooled. Furthermore, an increase in the bias voltage can partly recover the charge collection efficiency. The prototype sensors of both types were irradiated up to a fluence of 2×10^{14} 1 MeV n_{eq}/cm^2 , corresponding to $\sim$ 100 days of operation at nominal beam intensity. The leakage current measurements demonstrated that with a temperature of 5°C or lower, the sensors could be safely operated for all 100 days. The maximum full depletion voltage after the irradiation was found to be about 300 V; moreover, the irradiated sensors were able to operate at 750 V stably [137, 138].

Readout chip TDCpix

The majority of the requirements listed in Tab.3.1 are directly applied to the readout chip design. The summary of chip specifications is shown in Tab.3.2.

The GTK uses a custom-made chip, the TDCpix, manufactured with 130 nm IBM CMOS technology [140, 120, 141, 142]. The TDCpix is separated into two main areas – pixel matrix where hits are digitised and end-of-column (EoC) region where digitised hits are time-stamped, serialised and sent off-chip. This configuration allows minimisation of the number of clock signals in the sensitive area to reading and loading pixel configuration registers, limiting the risk of electronic noise.

The TDCpix is organised in four identical quarter-chips containing ten columns of 45 pixels with a total of 1800 pixels. Each pixel is equipped with one preamplifier with a 5 ns peaking time, a shaper, a time-over-threshold (ToT) discriminator, one five-bit threshold trim digital-to-analog converter (DAC),

Number of pixels per chip	$1800 = 45 \times 40$
Size of pixels	$300 \times 300\ \mu\text{m}^2$
Active area chip	$12\ \text{mm} \times 13.5\ \text{mm} = 162\ \text{mm}^2$
ASIC design time binning	~ 97 ps
Thickness of readout chip	$100\ \mu$m (0.11% X_0)
Dynamic input range	$0.7 - 10$ fC, $5000 - 60000\ e^-$
Electronic noise in pixel input with sensor	$< 250\ e^-$
Design particle rate per chip	105 MHz
Average rate per pixel	58 kHz
Peak rate per pixel/beam centre	114 kHz
Data transfer rate per chip	6 Gbit/s
Design transfer rate per chip	12.8 Gbit/s
Total dose in 1 year	6×10^4 Gy
Operating temperature	-20 to 5 °C

TABLE 3.2: Summary of the GTK on-sensor readout chip specifications [139]. Data and particle rates here correspond to the nominal beam intensity.

one three-bit configuration register and a transmission line driver. Lengths of the discriminated signals are equal to their ToT duration and proportional to released charges.

The signals are sent from pixels to the EoC region, where their rising and falling edges are measured. Non-adjacent pixels in each column are grouped by five with the help of an asynchronous multiplexer circuit called a hit arbiter; there are nine hit arbiters per column. This strategy allows reducing the number of needed time-to-digital converters (TDC) in the EoC region. The hit arbiter identifies the first coming signal and masks any other signals until the first one is deactivated. A pileup bit is set for simultaneous hits in a group, and all hit addresses are stored.

Each hit arbiter is connected to one two-channel TDC based on one delay-locked loop (DLL) shared between two adjacent columns. The TDC contains fine and coarse time counters with the precision of 97.7 ps[15] and 3.125 ns with a range up to 6.4 μs. The hit address and time stamp are encoded into 48-bit word and stored in a FIFO buffer. The data is then asynchronously sent out of the chip via 3.2 Gbit/s serialisers serving one quarter-chip. Notably, even though the EoC region is less exposed to radiation, the important registers are triplicated for the single-event upset (SEU) protection.

The discriminator thresholds can be adjusted by the pixel trim DAC and the column threshold DAC. The calibration is made by injecting a fixed charge in a

---

[15] The DLL operates at the nominal frequency of 320 MHz and is divided into 32 stages. Hence the minimal possible increment is 97.7 ps.

given pixel (or column) multiple times $\mathcal{O}(10^4 - 10^5)$ and scanning over a wide range of thresholds. The final value ensures that for the same charge, 50% of injections are counted. The calibration is verified with the help of a well-known radioactive source: a good set of thresholds provides a smooth function of the number of hits through the tested area.

The chip power dissipation is on average 4.1 W and varied across the chip as $\sim$ 4.8 W/cm^2 in the EoC region and 0.32 W/cm^2 in the pixel matrix. Since the optimal sensor operation requires temperatures below 5°C, and the detector is placed in vacuum, active cooling is mandatory.

Microchannel Cooling Plate

The GTK cooling plate was designed to keep the sensor and the chip at temperatures less than 5°C with a maximum difference of 10°C. Since the cooling should cover the sensor area, the amount of material used must be minimised. The microchannel cooling plate was developed to satisfy all these requirements [121, 143].

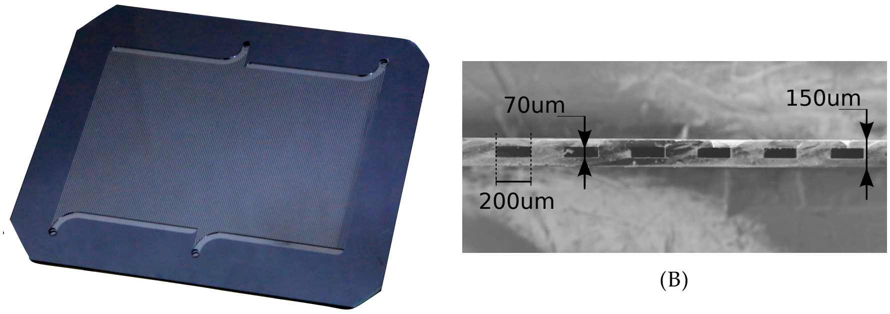

(A)

(B)

FIGURE 3.2: (A) Cooling plate wafer etched with channels and closed with glass. The two cooling circuits can be seen with their inlets and outlets. (B) Electron microscope image of the channel cross-section of a 150 μm thick prototype cooling plate produced to evaluate the limit of the technology. The pictures are taken from [122].

The cooling plate is made of two 70 × 80 mm^2 silicon wafers bonded together. One of the wafers is etched to have 150 channels with a cross-section of 200 × 70 μm^2 arranged into two circuits shown in Fig. 3.2. The coolant C_6F_{14} is circulated in the channels at 3 g/s to evacuate the heat. Each of the two circuits has an inlet and outlet openings on which the KOVAR connectors welded with capillaries are soldered.

A 300 W cooling plant is installed next to the stations to provide them with cooled C_6F_{14}. The plant is placed 10 m away from the beamline to reduce its radiation exposure.

Initially, the thickness of the cooling plate was 380 μm; however, with the introduction of the new production process based on silicon on insulator (SOI), the thickness of 210 μm was achieved (0.2% X_0).

GTK modules installed in 2016-2018 data taking periods

Tab.3.3 summarises the GTK modules used in 2016-2018. During these years, seven modules were used. The sensors were operated at a bias voltage of 100 V except for a few days at the end of each data taking period.

Module	Station	Cooling plate [μm]	Start of run	End of run	Comments
module 7	3	210	06/07/2016	14/11/2016	Beam started 03/05/2016
module 8	1	370	03/08/2016	14/11/2016	
module 9	2	380	15/09/2016	14/11/2016	
module 8	1	370	11/05/2017	23/10/2017	
module 9	2	380	11/05/2017	23/10/2017	
module 7	3	210	11/05/2017	23/10/2017	
module 12	1	330	11/04/2018	12/11/2018	
module 13	2	330	11/04/2018	12/11/2018	
module 15	3	210	11/04/2018	13/06/2018	Removed due to the chip problem
module 16	3	210	13/06/2018	27/06/2018	p-in-n, removed due to noise
module 7	3	210	27/06/2018	12/11/2018	

TABLE 3.3: Summary of GTK modules used in 2016-2018 data taking periods. All sensors are n-in-p unless stated otherwise. Dates in the "Start of run" column indicate the start of the SPS beam; if the module was installed during the run, it shows the installation date. The numbers in the "Station" column refer to the station in which the detector was installed.

The first set of three modules was installed in 2016. The detector was fully operational from mid-September 2016 until mid-November 2016. After that, the modules were dismounted and stored at $-21°$C. The same three modules were reinstalled in May 2017 and took data until the end of October 2017, when they were again dismounted and put into storage.

In April 2018, a new set of GTK modules was installed. The modules inserted in the first two stations were running until the end of November, while the module in the last GTK station was replaced twice. The first replacement was needed because one of the chips of GTK module 15 stopped interacting with the off-chip readout board due to the problem related to the wire bonding. The module was quickly replaced; however, the replacement had a p-in-n sensor, which produced noise. The same problem was observed during the data taking in 2015, but the reason for such behaviour is still unclear [144]. Since the number of noisy pixels in module 16 was rapidly increasing, it was decided to exchange it with one of the spare modules. Notably, the spare was GTK module 7 already used in the data taking periods in 2016 and 2017.

The beam intensity in 2016, 2017 and 2018 was about $30-35\%$, $50-65\%$ and $50-100\%$ of the nominal intensity, respectively. Examples of particle rates at each pixel of each station are shown in Fig. 3.3.

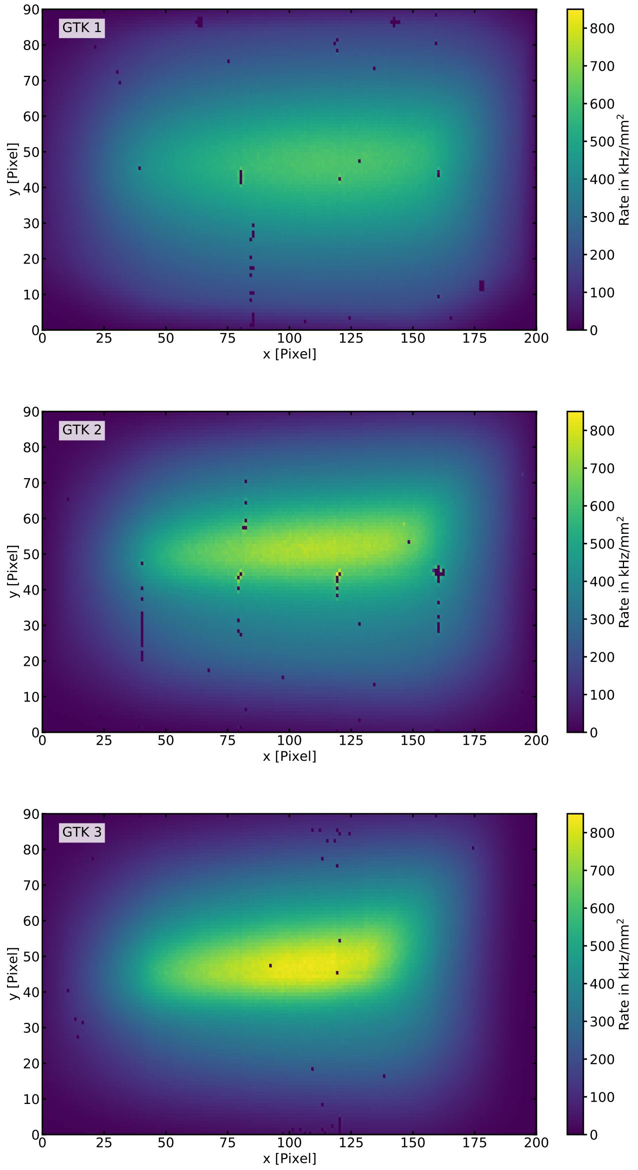

FIGURE 3.3: Average pixel rates in kHz/mm^2 in each of the three stations installed in the 2018 data taking period. The rates were extracted from run 8525, where the beam intensity was about 50% of the nominal. The run was taken at the beginning of the data taking, and therefore, all the modules here are new.

3.2 The GTK offline time calibration

The proper calibration of GTK is essential to achieve the required performances. While spatial alignment and track slope corrections for the magnetic field are out of the scope of this thesis (an example of this procedure can be found in [145]), the time calibration will be discussed in detail in the following subsections.

As mentioned in section 3.1, the TDCpix pixel front-end is based on the ToT discriminator, which requires an offline time walk correction. The compensation is needed since larger signals will reach discriminator threshold value faster than smaller ones (see Fig. 3.4 for the illustration). Thus, the smaller the signal is, the bigger the time correction will be needed. This effect is called time walk. To correct for the time walk, one needs to know the value of the hit charge, which can be extracted from the ToT. The relation between the ToT and charge is mostly linear except for charge values close to the threshold or saturation [146].

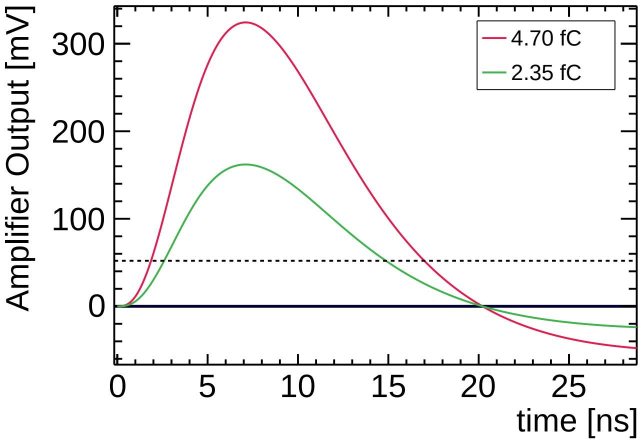

FIGURE 3.4: Simulated pixel amplifier output for 100 V sensor bias [122]. The dashed black line corresponds to the discriminator threshold. The two signals arrive simultaneously; however, the signal with a larger amplitude (red) reaches the threshold earlier than the smaller signal (green).

Additional time correction must be applied to each pixel due to its position in the pixel matrix to compensate for delays in the transmission lines to the EoC region. Finally, the mean time of each station and each chip must be corrected to compensate for delays in the cables and particle time of flight. All these corrections are evaluated and applied offline.

Coarse time calibration

The GTK coarse time calibration is done centrally along with all other NA62 detectors during the NA62 data processing. The time of each station and each chip is compared to the KTAG kaon candidate time. Then the mean of the difference is extracted with the help of a generic algorithm, similar for all detectors. The corrections are evaluated on the run by run basis using data of 100 bursts.

Pixel time calibration

The GTK pixel time calibration is crucial for reaching the single hit time resolution better than 200 ps. As explained at the beginning of this section, several corrections must be applied for each pixel.

One of the first projects of the author of this thesis was the integration of an already existing algorithm, discussed in [144, 145, 122], in the NA62 analysis and calibration framework. The corresponding source code of the calibration procedure can be found on the dedicated NA62 Doxygen page and in the NA62 `GitLab` repository along with other NA62 software for data analysis, calibration, reconstruction and Monte Carlo simulation [124, 125].[16]

In principle, the time calibration, namely the time walk and the individual time offsets (T0), should be applied for each pixel. However, it was observed that the time walk function is similar for most of the pixels in the chip [147]. Thus, to reduce the number of calibration constants and needed statistics, t was decided to perform the time walk calibration for the whole chip.

The GTK pixel time calibration algorithm consists of the following steps:

1. for each chip, fill a 3D histogram with pixel ID, hit time difference with the reference time (KTAG) and hit ToT;[17]
2. Read the filled 3D histogram:
   (a) exclude noisy pixels;
   (b) for each pixel ID, extract the mean time difference (pixel T0) at the bin corresponding to the most probable ToT value (by default set to 16 ns);
   (c) correct the histograms for pixel T0;
   (d) for the whole chip, extract a 2D histogram with the hit time difference as a function of the hit ToT;

---

[16] The Doxygen page of the source code: `na62-sw.web.cern.ch/d5/d0c/GigaTrackerPixelT0ChipTW_8cc_source.html`.

[17] For the histogram, a raw hit time corrected by the coarse time offset is used. The hits are selected in a 5 ns time window using their times after time walk calibration.

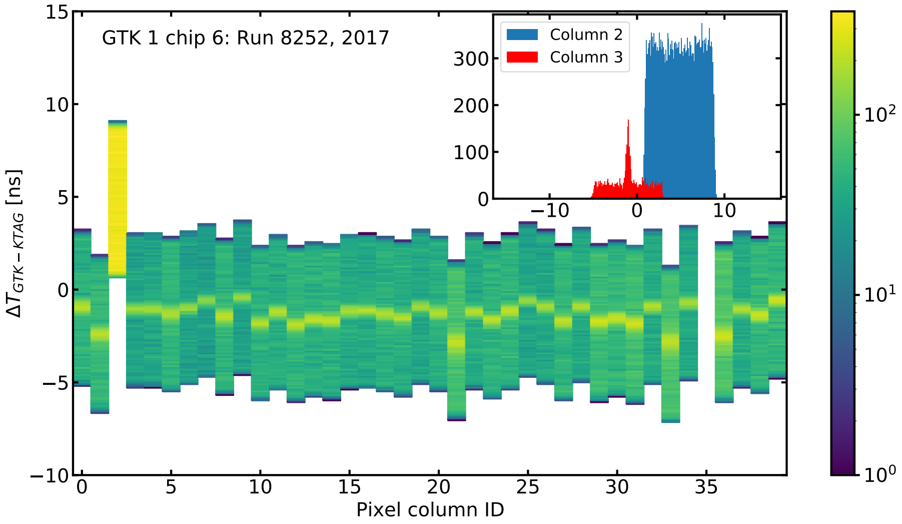

FIGURE 3.5: Example of the time difference between GTK hits and KTAG kaon candidates as a function of pixel column ID for a single row from GTK station 1, chip 6, row 32. Pixel time correction was not applied. One of the pixels in the row appears to be noisy (pixel column ID 2). The plot in the top right corner shows the time difference distribution for the noisy pixel compared to the regular pixel.

(e) for each ToT bin of the obtained 2D histogram, extract the mean time difference (time walk) using a Gaussian fit;

(f) correct the pixel histograms with the obtained time walk;

(g) extract the pixel T0 and correct for them the time walk histograms;

(h) extract the final chip time walk.

The calibration is very sensitive to noise, mainly affecting the time-walk in bins with lower statistics. For that reason, noisy pixels are excluded before proceeding with the calibration itself. Since noise is distributed uniformly in time and has much higher rates than physics signals (see Fig. 3.5), it can be easily detected and removed.

Despite providing satisfactory calibration constants, the algorithm has two main disadvantages. The first disadvantage is connected to memory consumption. Since each chip consists of 1800 pixels, 410 ToT bins are used with a width matching the size of the TDC bin, and the 3D histograms are filled with the statistics of a complete run (at least 1000 bursts), the memory required to read all histograms at once is higher than 2 GByte allowed for NA62 analysis and reconstruction programs. Thus, only one chip is calibrated in one batch job, and the final files with calibration constants are produced with the help of additional scripts. This complication made the procedure different from other detectors and required special treatment and extra time during the NA62 data processing rounds.

Another disadvantage is related to the complexity of the procedure described above. In this configuration, the calibration had to run on one run out of ten to minimise the necessary time. However, this approach is not optimal since corrections made for one run could be not perfectly suitable for another. Eventually, this can cause variations in the standard deviation and mean of the GTK-KTAG time difference. The latter can introduce an additional inefficiency in the matching between upstream and downstream tracks.

Considering all the disadvantages mentioned above, it was decided to revise the procedure and properly include it into the NA62 data processing routine. For this, the author of the thesis developed a completely automatic algorithm. The new calibration routine is based on the same idea as the old one. The order of the calibration constants extraction remained the same; however, a few details had to be changed.

The NA62 calibration is done for each run and is based on the statistics of 100 bursts which is much lower than previously used for the GTK pixel time calibration. Despite the reduced statistics, the memory-related complication mentioned above remained. As a solution, it was decided to fill a `ROOT TTree` [126] with the pixel ToT, time difference and pixel ID. The pixel ID contains all valuable information about the location of the pixel, i.e. the corresponding station ID, chip ID, column and row IDs. The usage of a `TTree` allowed to calibrate all chips simultaneously; however, it increased the program run time. A few possible improvements are foreseen for the run time reduction: the calibration of several or all chips could be run in parallel, and the number of calibration steps could be reduced. Furthermore, the possibility to use `ROOT RDataFrame` instead of `ROOT TTree` is considered.

While developing the new calibration procedure, it was noted that the ToT at which the first pixel T0 is extracted (16 ns by default) could be not optimal for some chips or groups of pixels. For example, in the data sample collected in 2017, the entire chip 4 of GTK3 had a peak ToT below 16 ns (see Fig. 3.6).

In such a case, the statistics can be somewhat low in the ToT range, several nanoseconds away from the peak (see Fig 3.7A). Low statistics combined with worsening of the time resolution in the lower ToT range affects the quality of the calculated pixel time offsets. Consequently, poorly extracted T0 for most of the pixels in a chip can lead to a failed time walk extraction and a failed chip calibration in general.

On top of that, in the presence of pixels with high ToT (several nanoseconds higher than 16), the time walk function may have a discontinuity, which is not

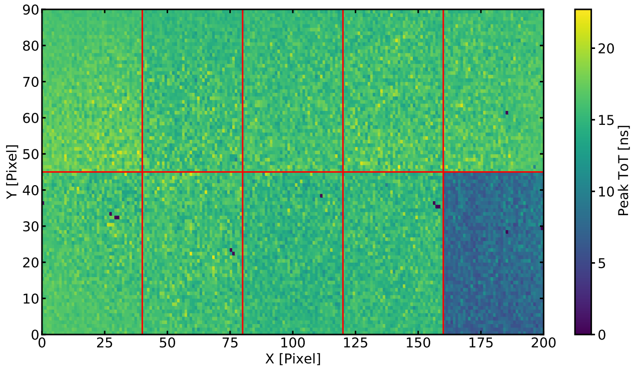

FIGURE 3.6: Pixel peak ToT as a function of the pixel coordinates for GTK station 3 in run 8252, 2017 data sample. The X and Y axes indicate the station column and row numbers. The red lines represent the chip borders. It can be noted that the bottom right chip (chip 4) has lower ToT, which is due to not optimal discriminator threshold settings.

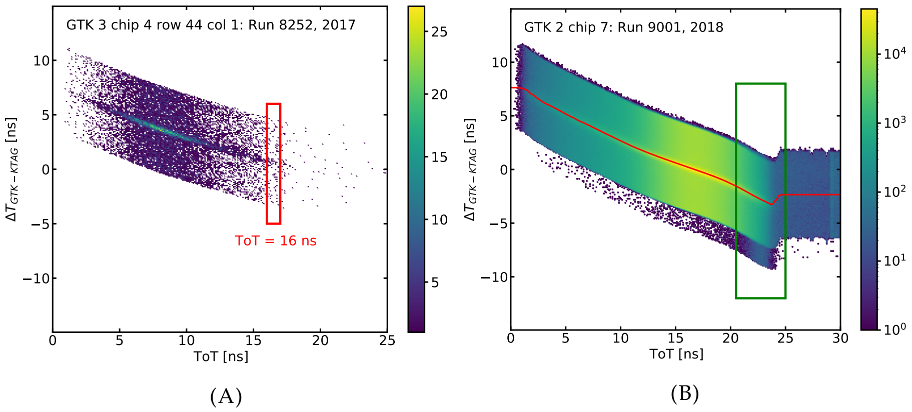

(A)

(B)

FIGURE 3.7: (A) Example of the time difference between GTK hit and KTAG kaon candidate as a function of ToT filled with data of 100 bursts from run 8252, 2017 data sample. The ToT range around 16 ns is indicated with the red box. Since the pixel peak ToT is around 8 ns, the statistics in the selected range is so small that no reliable pixel time offset can be extracted. (B) Example of the chip time walk for GTK2 chip 7 for run 9001, 2018 data sample. The red line illustrates the final time walk function. The green box highlights the ToT range of the time walk with the discontinuity, which appeared due to a pixel with higher ToT.

expected (Fig. 3.7B). The latter problem can be minor since it affects ordinary pixels only in the tails of the ToT distribution. However, the hits with ToT values in the range of $20 - 24$ ns are still used in the reconstruction and physics analysis and therefore must be properly calibrated as well.

To solve the default ToT problem, it was decided to extract the pixel T0 in five bins around the pixel peak ToT bin. Additionally, the chip time walk is now retrieved as a function of the difference between the hit ToT and the pixel peak ToT. This approach made the procedure more robust to changes in the pixel ToT distribution, which may appear due to the threshold calibration or radiation damage. Furthermore, it helped to increase the statistics needed to extract the first pixel T0 corrections and disentangle pixel offset and time walk corrections. Thanks to this improvement, calibration constants obtained at the first round of T0-time walk were found to be compatible with the final ones for most of the chips and pixels. Currently, the possibility of reducing the number of calibration steps is being investigated as it can help to reduce the program run time.

Another improvement was introduced to enhance the quality of the time walk corrections. Since the time walk relies on the output of the Gaussian fit at each ToT bin, it is prone to variations in the extracted mean. This situation frequently happens in the bins with low statistics, particularly on the positive side of the ToT difference. Therefore, to smooth the time walk, a simple local polynomial regression algorithm was implemented.

After the calibration is finished, the program produces `.dat` files with the calibration constants and a report in `.pdf` format with chip time walk and pixel T0 plots for further quality checks.

An example of pixel T0 offsets and chip time walk is shown in Fig. 3.8; analogous plots are saved in the `.pdf` report mentioned above. Notably, the pixel time offset from Fig. 3.8A gradually increases towards the centre of the station, which is expected due to the chip design discussed earlier in this chapter. The number of calibration constants per chip is 1800×2 for pixel offsets and peak ToT values and 333 for the time walk bins. It is larger than before due to the addition of the pixel peak ToT. However, pixel peak ToTs help reconstruct the pileup hits, which arrive simultaneously and share the same hit arbiter. Such signals do not have a reliable trailing time measurement; thus, they lose the ToT information and cannot be corrected appropriately. Therefore, providing the most probable ToT value for a given pixel can improve the time resolution of pileup hits, which, in turn, can improve the GTK efficiency. However, the efficiency improvement is expected to be below 1% since pileup hits are a few per mill of all GTK hits.

The hit time resolution and the mean were found to be compatible with the one obtained by the old version of the calibration. Fig. 3.9 demonstrates the time

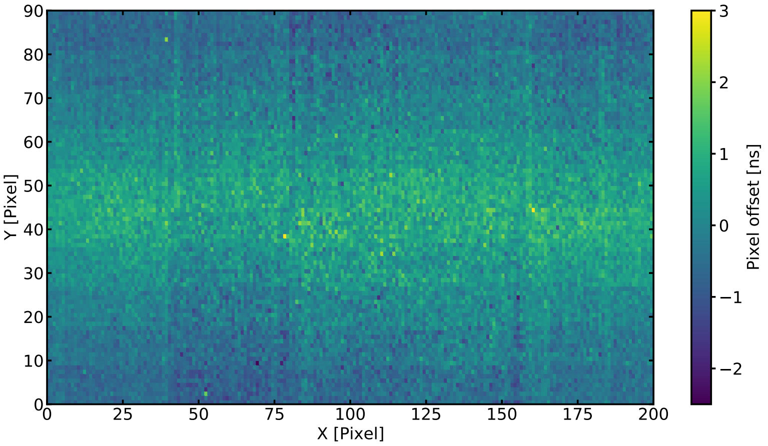

(A)

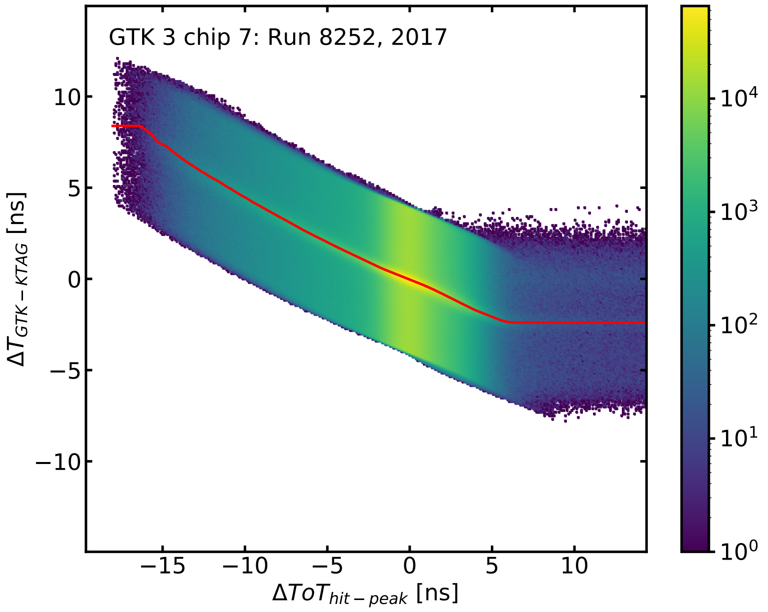

(B)

FIGURE 3.8: (A) Example of pixel delays for GTK2 as a function of pixel coordinates extracted using run 8252, 2017 data sample. Gradual increase in the pixel offset towards the centre of the station is expected because of the TDCpix design. (B) Example of the chip time walk as a function of the difference between hit ToT and pixel peak ToT for GTK3 chip 7 extracted using run 8252, 2017 data sample. The red line illustrates the obtained time walk function.

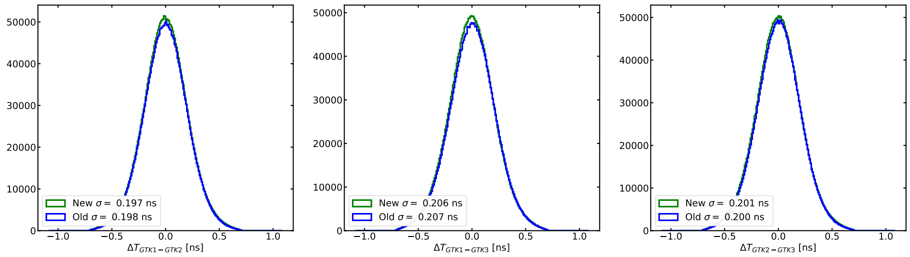

FIGURE 3.9: Comparison of the time difference between GTK stations using the old calibration constants (green) and the new calibration constants (blue). Left to right: $\Delta T_{GTK1-GTK2}$, $\Delta T_{GTK1-GTK3}$, $\Delta T_{GT2-GTK3}$. Data – run 8252, 2017 data sample. The observed differences are negligible.

difference between each GTK station and the peak resolution extracted with a Gaussian fit for each calibration version. It can be noted that the differences between the versions are on the picosecond level. From the standard deviations of the peaks can be concluded that in the selected run (run 8252, 2017 data sample), the time resolution of a single hit in GTK1 is 142 ps, GTK2 is 136 ps, and GTK3 is 148 ps which is well below the design value of 200 ps (Tab. 3.1).

The corresponding calibration code is now included in the NA62 analysis and reconstruction framework and is used in the NA62 data processing.[18]

3.3 Data quality monitoring

Data quality monitoring is essential for detecting problematic bursts and identifying possible sources of inefficiency. Therefore, dedicated programs were developed by the author of this thesis to be used in the NA62 data processing.

The first program is called `GigaTrackerDataQualityMonitor`,[19] and its main task is to identify bursts not suitable for any physics analysis relying on the GTK. The program uses the minimum bias trigger and relies on the standard NA62 analysers `K2piSelection`[20] and `K3piSelection`[21]. The analysers, as indicated by their names, reconstruct the $K^+ \to \pi^+\pi^0$ ($\mathcal{B} \sim$ 20.67%) and $K^+ \to \pi^+\pi^+\pi^-$ ($\mathcal{B} \sim$ 5.58%) decays, respectively [148]. The time and kinematic parameters of the reconstructed positively charged tracks are used to evaluate

---

[18] The Doxygen page of the source code: `na62-sw.web.cern.ch/d2/d02/GigaTrackerTimeCalibration_8cc_source.html`.

[19] The Doxygen page of the source code: `na62-sw.web.cern.ch/d3/d36/GigaTrackerDataQualityMonitor_8cc_source.html`.

[20] The Doxygen page of the source code: `na62-sw.web.cern.ch/d8/d41/K2piSelection_8cc_source.html`.

[21] The Doxygen page of the source code: `na62-sw.web.cern.ch/d1/dea/K3piSelection_8cc_source.html`.

the GTK-STRAW matching efficiency. The matching is done using one of the two methods. One method relies only on time, and the other, similar to the matching used in $K^+ \to \pi^+\nu\bar{\nu}$ analysis [117], relies on time and the closest distance of approach of the beam track to the downstream particle (CDA). The efficiency is computed for each burst and run; additionally, it is expressed in bins of the instantaneous intensity measured with out of time GTK hits and with KTAG candidates. The efficiency is defined as the number of events with matched GTK tracks divided by the number of normalisation events, either $K^+ \to \pi^+\pi^+\pi^-$ or $K^+ \to \pi^+\pi^0$.

The events that pass the matching allow for studying various parameters of GTK tracks and hits. The resolution and mean of the time difference between GTK tracks and KTAG kaon candidates is monitored for each burst and run. Moreover, for $K^+ \to \pi^+\pi^0$ decays for each run, the mean and the resolution of the squared missing mass $m^2_{miss} = (P_{GTK} - P_{\pi^+})^2$ distribution are extracted.

The analyser also keeps track of the events with the so-called bad quality mask. These events typically have errors related to the GTK readout and DAQ problems, for example, a missing chip flag or data corruption. Additionally, events are marked as bad in reconstruction if the number of hits in ± 10 ns with respect to the reference time, typically the trigger, is higher than 300. The cut was introduced due to the problems observed in the processing of several bursts. Such bursts had so many hits in the GTK in the first few seconds of the burst that the track reconstruction needed about eight times more time to produce the output than usually. As a result, it was considered that these events are not useful for physics analysis and, therefore, must be rejected. Indeed, in terms of rate, it corresponds to about 5 GHz per station, which is five times larger than the design value.

The analyser also contains a study of pixel ToT where the peak values and peak widths are extracted for each pixel in each run. This study allows monitoring the changes in the ToT distributions caused by radiation.

As an output, the analyser creates a report in `.pdf` format with basic plots and a text file with burst and run numbers, the quality of which was considered to be not sufficient for the physics analysis. Apart from the burst and run numbers, the output text file contains a flag indicating why the burst appeared on the list. The categories of bursts considered as bad and their flags are summarised in Tab.3.4. The first four flags are unrelated to the GTK – they were added to spot generally bad bursts where, for example, there were problems with the SPS beam or trigger related issues. The bursts marked with `LOWSTATK2PI` and `LOWSTATK3PI` also have nothing to do with GTK and typically indicate problems in other subsystems. The rest is directly related to the GTK performance. The thresholds quoted in the table were chosen based on typical values obtained with the selections used.

Flag	Description
`EMPTYBURST`	Low counts of the minimum bias trigger, no events in the GTK and no counts in the ARGONION
`NOARGON`	Low counts of the minimum bias trigger and no counts in the ARGONION
`LOWARGON`	Low counts of the minimum bias trigger and low counts in the ARGONION
`LOWTRIGGER`	Low counts of the minimum bias trigger
`LOWSTATK2PI`	Number of reconstructed $K2\pi$ events in the minimum bias trigger is lower than 30
`LOWSTATK3PI`	Number of reconstructed $K3\pi$ events in the minimum bias trigger is lower than 15
`BADGTKDAQ`	Fraction of events with good GTK quality is lower than 90% of all recorded GTK events
`LOWEFFGTK`	Fraction of GTK tracks matched in time with $K2\pi$ and $K3\pi$ in a burst is lower than 77%
`LOWEFFGTKMatch`	Efficiency of GTK-$K2\pi$($K3\pi$) matching is lower than 60%

TABLE 3.4: Summary of the GTK bad burst flags used in the data quality monitoring. ARGONION is the beam monitoring counter placed at the end of the K12 beamline 264 m downstream of the target.

An example of the `.pdf` report with the studies mentioned previously in this section is shown in Appendix A.

Another GTK data quality monitoring program, `SpectrometerGigaTrackerMatchingEfficiency`,[22] aims to study sources of GTK inefficiency. The program is based on matching the GTK track with the $K3\pi$ event. The $K3\pi$ events are selected with the standard `K3piSelection` as previously, but now only events in the last GTK station acceptance are requested. This selection was made to reduce the inefficiency due to the geometrical acceptance of GTK. The GTK candidates are selected in $\pm 3\sigma_T$ with respect to KTAG time, where $\sigma_T = 180$ ps, and matched with the $K3\pi$ candidate using a discriminant built as:

$$\begin{split} D = \left(\frac{P_{GTK} - P_{K3\pi}}{\sigma_P}\right)^2 + \left(\frac{\theta^X_{GTK} - \theta^X_{K3\pi}}{\sigma_{\theta^X}}\right)^2 + \left(\frac{\theta^Y_{GTK} - \theta^Y_{K3\pi}}{\sigma_{\theta^Y}}\right)^2 + \\ \left(\frac{X^{GTK3}_{GTK} - X^{GTK3}_{K3\pi}}{\sigma_{X^{GTK3}}}\right)^2 + \left(\frac{Y^{GTK3}_{GTK} - Y^{GTK3}_{K3\pi}}{\sigma_{Y^{GTK3}}}\right)^2 \end{split} \tag{3.1}$$

where P_{GTK}, $P_{K3\pi}$ are the GTK track momentum and the total of momentum of three pions respectively, θ^i_{GTK}, $\theta^i_{K3\pi}$ ($i = X, Y$) are angles of the GTK track and

---

[22] The Doxygen page of the source code: `na62-sw.web.cern.ch/d4/da8/SpectrometerGigaTrackerMatchingEfficiency_8cc_source.html`.

the total momentum of three pions, and i^{GTK3}_{GTK}, $i^{GTK3}_{K3\pi}$ ($i = X, Y$) are positions of the GTK candidate and the total 3π momentum at GTK3. The momentum, angular and spatial resolutions are extracted from the data, and $1.5\sigma_i$ values are taken as discriminant parameters listed in Tab. 3.5.

Variable	Value
σ_P	400 MeV/c
$\sigma_{\theta X,Y}$	30 μrad
$\sigma_{(X,Y)^{GTK3}}$	2 mm

TABLE 3.5: Values of parameters used for the GTK-$K3\pi$ matching discriminant in `SpectrometerGigaTrackerMatchingEfficiency`.

The GTK candidates with the minimum discriminant value of less than 20 are selected as a match. For these candidates, parameters as resolutions of track time, momentum and angle are studied. Additionally, the probability of finding a match is estimated as a function of the burst number, the run number, the instantaneous intensity, the number of KTAG candidates (used as an alternative measure of instantaneous intensity) and the time in the burst. This study allows investigating if the GTK track reconstruction and GTK calibrations are working as expected. However, it does not provide precise tracking or matching efficiency measurement since it does not consider pileup and kaon-pion mistag probabilities in the KTAG.

For events without a good GTK match, candidates with hits in only two GTK stations are reconstructed. The position in the missing station is predicted using hit positions in two other stations as

$$X_{miss} = Hit^1_X + \frac{Hit^2_X - Hit^1_X}{Hit^2_Z - Hit^1_Z} \times \left(Z_{miss} - Hit^1_Z\right) \tag{3.2}$$

$$Y_{miss} = Hit^1_Y + \frac{Hit^2_Y - Hit^1_Y}{Hit^2_Z - Hit^1_Z} \times \left(Z_{miss} - Hit^1_Z\right) \tag{3.3}$$

where the index i of Hit^i_j is related to the station Z position: the hit with index 1 corresponds to the station closest to the target.

If the missing hit is in GTK3, a shift is added to its X_{miss} to compensate for the effect of the TRIM5 (described in section 2.3) as

$$\Delta X_{TRIM5}(Z) = -\frac{c \cdot B_{TRIM5} \cdot L_{TRIM5}}{P_{K3\pi}} \times (Z - Z_{TRIM5}) \tag{3.4}$$

$$X_{miss} = X_{miss} + \Delta X_{TRIM5}(Z_{miss}) \tag{3.5}$$

where c is the speed of light, B_{TRIM5} is the strength of the TRIM5 magnetic field (0.7505 T/m), and L_{TRIM5} is the length of the TRIM5 magnet (400 mm). The kick produced by the TRIM5 is about 90 MeV. Alternatively,if there is a hit in GTK3, the same shift as above has to be subtracted from the predicted X position of the missing hit as:

$$\begin{aligned} X_{miss} = Hit^1_X + \frac{Hit^2_X - \Delta X_{TRIM5}(Hit^2_Z) - Hit^1_X}{Hit^2_Z - Hit^1_Z} \\ \times \left(Z_{miss} - Hit^1_Z\right) \end{aligned} \tag{3.6}$$

The reconstructed candidates are then matched with $K3\pi$ in a similar way as before using the hit position at GTK3, track slopes and candidate time computed as an average between hits in the two remaining GTK stations. If the matching candidate was found, the missing hit position is plotted for each station separately. Doing so allows visualising inefficiencies and helps to pinpoint such problems as dead or noisy pixels. An example of such visualisation is shown in Fig. 3.10, where inefficiencies from the geometrical acceptance, noise and dead pixels are visible.

The method described above can be helpful for the station efficiency evaluation. However, it is not so straightforward now since there are only three stations, meaning that the efficiency based on candidates with hits in two stations will have a non-negligible station-dependent uncertainty. In the new data taking period starting in July 2021, an additional GTK station, GTK 0, will be installed right before GTK1 (currently the first station). As a result, the predicted track position based on the reconstructed candidates with hits in three remaining stations will be much more precise, allowing for a more robust station efficiency evaluation.

The `SpectrometerGigaTrackerMatchingEfficiency` analyser is included in the NA62 data processing routine, and that is why it also produces a report in `.pdf` format. Appendix A features some plots from this report and shows some additional studies omitted in this section.

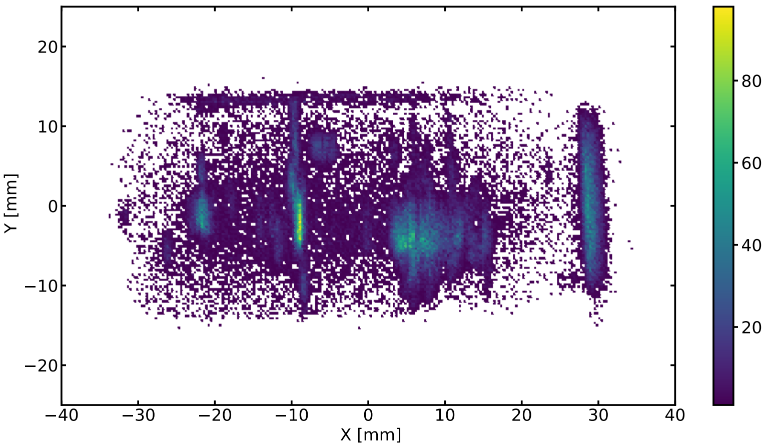

(A)

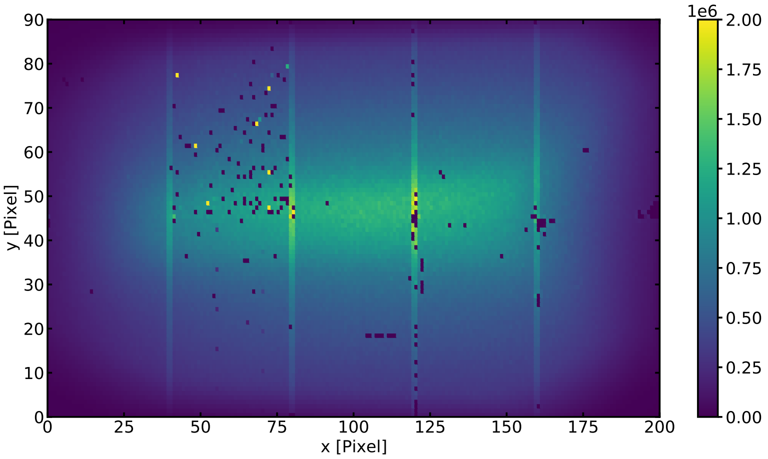

(B)

FIGURE 3.10: (A) Example of the map of missed hits at GTK1 extracted using data from run 8252, 2017 data sample. The inefficient areas should be compared with the hit map of the same station made for the same run and shown in Fig. (B). Note that the coordinate axes in Fig. (A) are rotated by 180° with respect to those in Fig. (B). Comparing the two figures, one can see that the inefficiencies correspond to the dead or noisy pixels and areas outside the detector acceptance.

3.4 Performance in 2017-2018 data taking periods

The following subsections will overview the GTK performances in the 2017 and 2018 data taking periods. In particular, the bad burst lists created by the data quality monitoring tool described above and the achieved GTK hit resolutions will be presented.

The choice of 2017 and 2018 samples was motivated by the NA62 data processing – only these two samples were available with the run by run pixel time calibration at the time of preparing this manuscript.

Bad bursts

The total number of GTK bad bursts in 2017-2018 data samples was found to be 22783 (22.46% of all bad bursts). From this number, 2357 (10.02%) bursts were marked as bad in 2017 and 20426 (26.21%) in 2018.[23] From all bad bursts, only 1.68% (0.75% in 2017 and 1.97% in 2018) were bad solely due to the GTK. The majority of these in 2017 was due to `LOWEFFGTKMatch`, while in 2018 it was `BADGTKDAQ`. Most of them (if not all) are related to generally unstable data taking conditions.

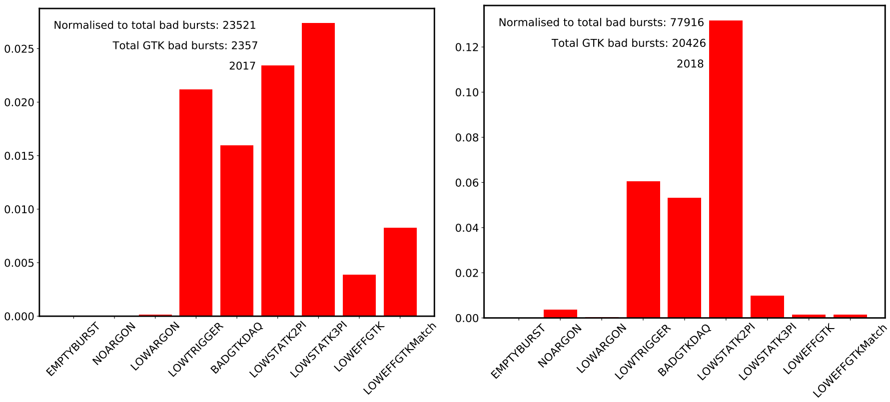

(A) (B)

FIGURE 3.11: GTK bad bursts by category from Tab. 3.4 in the 2017 (A) and 2018 (B) data samples. The bar plots are normalised to the total number of bad bursts in a given period. It can be noted that the most frequent flag in 2017 (2018) was `LOWSTATK3PI` (`LOWSTATK2PI`).

---

[23] The percentage in the brackets provides the fraction of the GTK bad bursts of all bad bursts in a given data sample.

Fig. 3.11A and Fig. 3.11B display GTK bad bursts by category for each data sample. It can be noted that a large fraction of these bursts was rejected due to reasons not related to the GTK, which suggests a generally good quality of the GTK data and the applied offline calibrations.

Time resolution

The expected time resolution of the GTK can be described as [149]:

$$\sigma_t = \sqrt{\sigma^2_{electronics+TDC} + \sigma^2_{weighting\ field} + \sigma^2_{straggling}} \tag{3.7}$$

where $\sigma_{electronics+TDC}$ corresponds to the resolution provided by the TDCpix with no sensor connected, $\sigma_{weighting\ field}$ is related to the pixel geometry and the weighting field, $\sigma_{straggling}$ is the contribution from the energy straggling. The quoted resolutions were estimated with the help of laboratory studies and simulations. Their values were found to be $\sigma_{electronics+TDC} \sim 80$ ps, $\sigma_{weighting\ field} \sim 85$ ps and $\sigma_{straggling} \sim 100$ ps. Therefore, the expected single hit time resolution of the GTK is $80 \oplus 85 \oplus 100 = 150$ ps. [24]

In this section, the resolution was extracted using the `SpectrometerGigaTrackerMatchingEfficiency` tool. Only matched candidates with one hit per station were used. For most plots in this section (unless stated otherwise), the resolution was extracted by comparing the three station to station time differences as in Fig. 3.9.

In Fig. 3.12 the GTK single hit time resolution is shown as a function of time for each module installed in 2017 and 2018 with the nominal bias voltage of 100 V. A moderate increase of about 20 ps by the end of each data taking period was observed in all used modules. This behaviour is expected due to the radiation-induced damages in the sensor. Additionally, it can be noted that the time resolution of GTK module 7 at installation in 2018 was about 20 ps larger compared to modules 12 and 13, and it was similar to its resolution measured at the end of the 2017 data taking period. The latter is important because it suggests that conservation, transportation and re-calibration of pixel thresholds did not affect the detector. Another detail can be seen from the trend of module 16 equipped with a p-in-n sensor – its resolution seems to increase much faster compared to n-in-p modules. The n-in-p modules, in turn, have a more or less similar rate of time resolution degradation. The difference in timing performances between n-in-p and p-in-n sensors can be explained by charge carriers: n-in-p collects electrons, which are faster than holes collected by p-in-n and less affected by trapping.

---

[24] Note that here a p-in-n sensor with a bias voltage of 300 V was assumed.

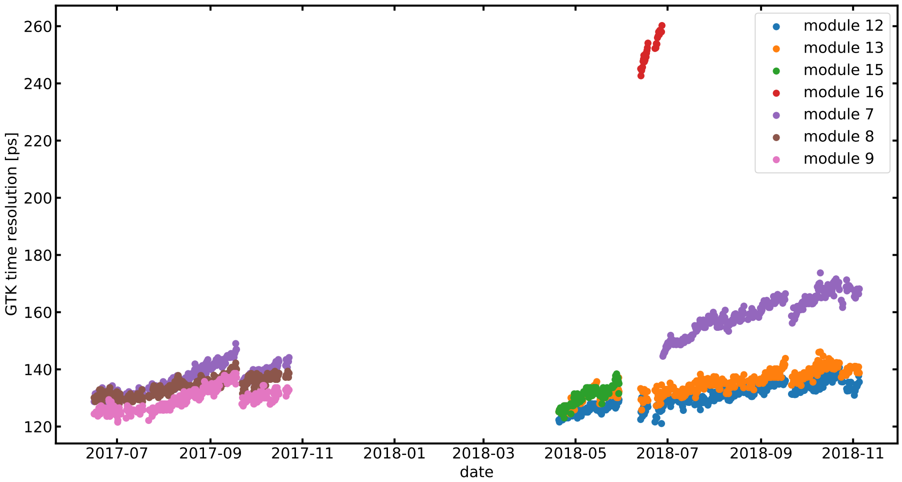

FIGURE 3.12: Single hit time resolution of each GTK module installed in 2017-2018. A moderate increase of about 20 ps can be seen by the end of each data taking period. All sensors except for the one used in module 16 are n-in-p.

As mentioned earlier in this chapter, at the end of each data taking period, the bias voltage of each installed module was changed from its nominal value. In this thesis, the data collected during the bias voltage test performed in the last week of the 2018 data taking period was analysed. During this week, the bias voltage was gradually increased from 100 to 300 V with steps of 50 V, and a few runs were taken at each value. Fig. 3.13 shows the single hit time resolution for each tested module as a function of the bias voltage. It can be seen that there is a slight but clear improvement in time resolution with the change of voltage from 100 to 300 V. Notably, even after three years of data taking, module 7 was able to achieve similar timing performances as the new modules with the bias voltage increased only by 50 V.

Apart from investigating the time resolution as a function of time and the bias voltage, it is also interesting to analyse it as a function of pixel coordinates. While performing the corresponding study, a peculiar feature was observed in GTK module 7. Fig. 3.14A illustrates the resolution of the time difference between the KTAG kaon candidate and a single GTK hit as a function of the pixel position for module 7. The data used to prepare this figure was collected close to the end of the 2018 data taking period with the sensor bias voltage set to 100 V. Unfortunately, due to the limited statistics in a single run the resolution of pixels far from the beam spot was not extracted (uncoloured area on the plot). From the distribution on Fig. 3.14A, it can be seen that the resolution of the GTK-KTAG time difference for pixels at the centre of module 7 is above 250 ps, which is much worse compared to other pixels (and

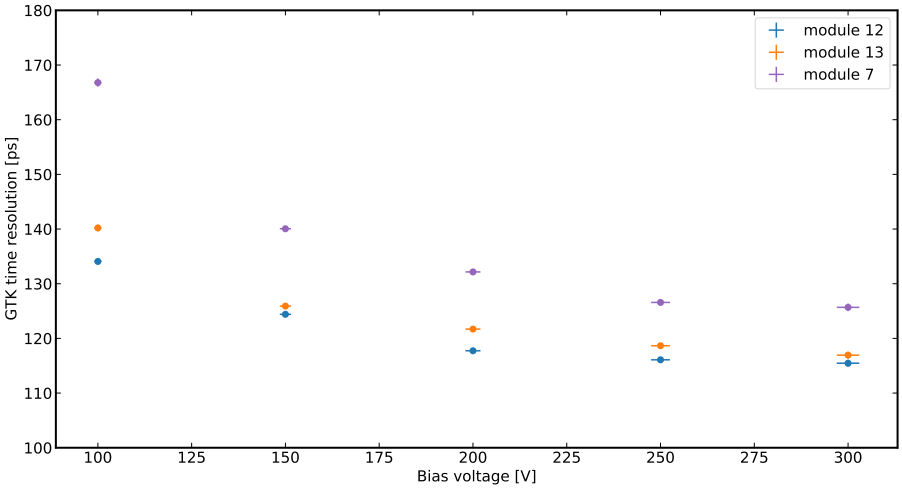

FIGURE 3.13: Single hit time resolution as a function of the sensor bias voltage evaluated for each GTK module installed at the end of the 2018 data taking period. A moderate improvement of about 20 and 40 ps is observed for modules 12, 13 and 7, respectively, at the bias voltage of 300 V.

other modules). Interestingly, the shape of the group of pixels with the worst timing performance on Fig. 3.14A resembles the beam spot. Furthermore, a similar structure, but less visible, was also observed during the pixel threshold calibration before the installation in 2018 [150].

Several pixels in this area were inspected, and it appeared that the time difference between the GTK and the reference time has a double peak in the tails of the pixel ToT distribution. This behaviour dramatically affected the time-walk calibration in the ToT range above 20 ns. For further details, see Appendix B.

Notably, after the increase of bias voltage to 150 V, the problem from Fig. 3.14A was visibly mitigated, and at 200 V, the structure disappeared (see Fig. 3.14B and 3.14C). This behaviour implies that radiation-induced damages in the sensor could be responsible for the observed structure. The effects of radiation damage on silicon sensors will be discussed in the next section, along with the radiation damage studies performed for the GTK.

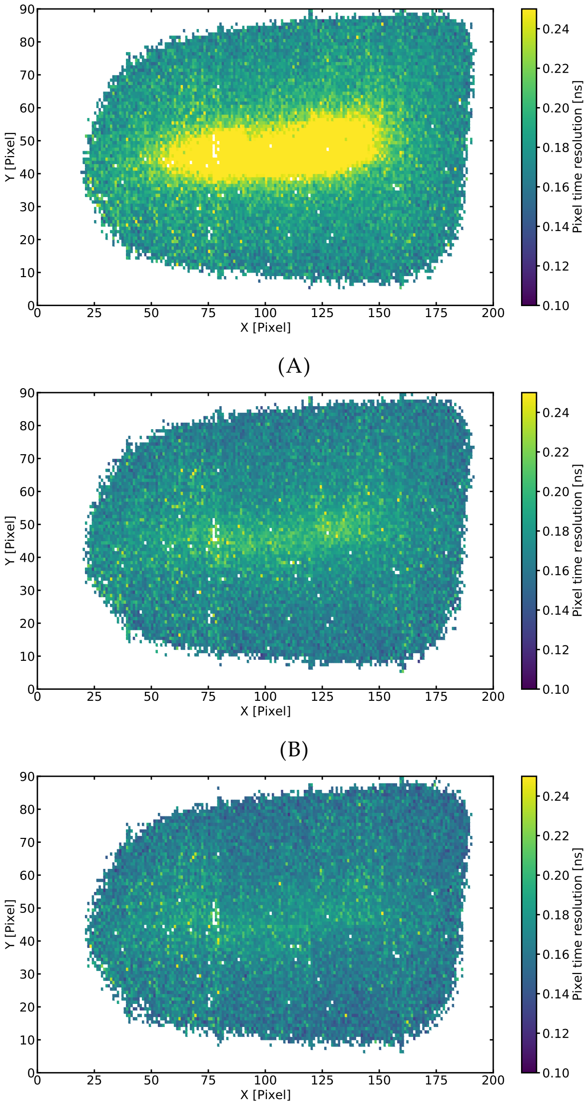

(A)

(B)

(C)

FIGURE 3.14: Resolution of the time difference between the KTAG kaon candidate and a single GTK hit as a function of pixel coordinates for GTK module 7 measured at the end of the 2018 data taking period with different bias voltages: (A) – 100 V, run 9263; (B) – 150 V, run 9421; (C) – 200 V, run 9430. The resolution of a large group of pixels at the centre of the module on Fig. (A) dramatically improves after the bias voltage increase. The observed behaviour can be related to the radiation-induced defects in the sensor.

3.5 Radiation damage studies

In a high radiation environment such as NA62, particles passing through the detector material can cause various damages to its structure. This effect is known as detector ageing or radiation damage.[25]

In silicon sensors, detector ageing effects can be roughly divided into surface damage and bulk damage. The surface damage happens in the insulating silicon oxide layers. It is typically caused by photons and charged particles and its main consequences are:

- an increase in the leakage current and inter-pixel capacitance;
- a decrease in the inter-pixel resistance;
- possible charge losses at the interface.

The effects of the surface damage tend to saturate after some small irradiation. The bulk damage, on the contrary, occurs in the silicon lattice. It is primarily caused by protons, pions and neutrons dislocating atoms from their positions in the silicon lattice. The defects in the semiconductor lattice mainly cause:

- changes in the silicon depletion voltage;
- an increase in the leakage current;
- decrease of the charge collection efficiency due to the charge carriers trapping.

The radiation-induced leakage current, therefore, mainly consists of two components – bulk and surface. Depending on the device and the kind of radiation it was exposed to, one type of current can dominate over another. The bulk current depends on the applied bias voltage as $\sqrt{V_{bias}}$ for $V_{bias} < V_{depletion}$ and the sensor temperature. Notably, there is no strong relationship between the surface current and temperature, but it can be proportional to the applied bias voltage. Thanks to the temperature dependence of the bulk current, the current measured at temperature T can be scaled to some reference temperature T_0 as

$$I(T_0) = I(T) \cdot R(T),\; R(T) = \left(\frac{T_0}{T}\right)^2 exp\left(-\frac{E_g}{2k_B}\left[\frac{1}{T_0} - \frac{1}{T}\right]\right) \tag{3.8}$$

where E_g is the energy gap (for silicon $E_g = 1.21$ eV [153]) and k_B is the Boltzmann constant ($k_B = 8.617 \times 10^{-5}$ eV K^{-1}).

The radiation damage caused by different types of particles at different energies is typically described with the help of the non-ionising energy loss (NIEL) hypothesis. The main assumption of the hypothesis is that any bulk damage

---

[25] More information about radiation damage effects can be found in [151, 152] on which this short review was based.

scales linearly with the non-ionising energy transfer to the silicon lattice. The integrated fluence, used as a measure of bulk damage, is proportional to the displacement damage cross-section. Furthermore, it depends on the energy, fluence and type of the interacting particles. Therefore, to compare results from different experiments, fluences are normalised to the displacement damage cross-section for 1 MeV neutrons (95 MeV mb [154]). For mono-energetic beams, the following conversion is normally used

$$\Phi_{eq} = \kappa\Phi \tag{3.9}$$

where Φ is the integrated fluence for 1 MeV neutrons, κ is the hardness factor defined experimentally or obtained from simulations, and Φ_{eq} is the integrated fluence in 1 MeV neutron equivalent (1 MeV n_{eq}).

Several techniques are used to study the bulk damage: measurement of leakage current and measurement of full depletion voltage. While the estimation of the GTK depletion voltage during the data taking was not performed,[26] the leakage current was continuously monitored. The bulk leakage current is related to the integrated fluence as

$$\Delta I_{leak} = \alpha\Phi_{eq}V \tag{3.10}$$

where ΔI_{leak} is the difference between leakage current before the irradiation and after, V is the depleted volume, α is the current related damage rate depending on temperature. The parameter α also accounts for the annealing effects in silicon sensors. Annealing describes the migration of the defects created by the radiation damage in the semiconductor. There are two types of annealing: beneficial and reverse. Beneficial annealing is a process when some of the dislocated atoms fall back into the normal lattice position; it is a temperature-dependent process. Reverse annealing, instead, happens when individual defects start to cluster, which leads to changes in the effective doping concentration. Typically, the Hamburg model [151] is used to parametrise these effects. In this model, α is described as

$$\alpha(t,T) = \alpha_0(T) + \alpha_I exp\left(-\frac{t}{\tau_I(T)}\right) - \beta ln\left(\frac{t}{t_0}\right) \tag{3.11}$$

where the exponential term and logarithmic terms correspond to the detector annealing processes, t_0 is a time scale parameter, $\tau_I(T)$ is a temperature-dependent time constant given by Arrhenius relation

$$\frac{1}{\tau_I(T)} = k_{0I} \times exp\left(-\frac{E_I}{k_B T}\right) \tag{3.12}$$

The values of the parameters at room temperature are shown in Tab. 3.6.

---

[26] The GTK depletion voltage is measured only in the laboratory due to the complexity of the procedure.

Parameter	Value
α_0	$(7.07 \pm 0.71) \times 10^{-17}$ A/cm*
α_I	$(1.23 \pm 0.006) \times 10^{-17}$ A/cm
β	$(3.29 \pm 0.33) \times 10^{-18}$ A/cm*
k_{0I}	$1.2^{+5.3}_{-1.0} \times 10^{13}$ s^{-1}
E_I	1.11 ± 0.05 eV
t_0	1 min

TABLE 3.6: Values of parameters of leakage current annealing at temperature $T = 21°\text{C}$ [151]. Entries marked with $*$ did not have specified uncertainties in the reference; therefore the 10% error was assigned.

High voltage scans

High voltage scans taken at different sensor temperatures are good for estimating and distinguishing bulk and surface current contributions to the total leakage current. The obtained value of the bulk current, in turn, can provide a measure of the integrated fluence.

Generally, during the data taking in 2017 and 2018, the high voltage scans were performed once a week. The temperatures were set by exploring power dissipation at different operation modes of the readout chip. In the end, the scan was done in three different temperature regimes. An example of the scan is shown in Fig. 3.15A.

As one can see, the current has a very defined dependency on the applied bias voltage ($\sim \sqrt{V}$) and on the temperature, which indicates that the GTK leakage current was dominated by the bulk component (see subsection 3.5 for the explanation). The measured bulk current values are normalised to a reference temperature of 21°C with the help of Eq. 3.8. The current values were extracted at 100 V (approximately plateau) and plotted against the temperature. The resulting distribution was fitted with the function $I(T_0) \cdot R(T)$ from Eq. 3.8, where $I(T_0)$ is the parameter of the fit and $T_0 = 21°\text{C}$. Fig. 3.15B shows the current as a function of temperature with the fit and its result; the error on $I(T_0)$ was extracted from the fit. The same procedure was repeated for each taken HV scan.

The results for each station measured from HV scans taken in 2017-2018 are presented in Fig. 3.16. It can be noted that the leakage current at the end of the 2018 data taking period increased by about 700 μA/cm^3 for modules 12 and 13 and 300 μA/cm^3 for module 7. A similar effect but slightly lower can be seen at the end of the physics run in 2017. Additionally, in each data taking period, one can notice small discontinuities in the trend of the leakage current (order of 10 μA). These discontinuities match with the beam stops and cooling

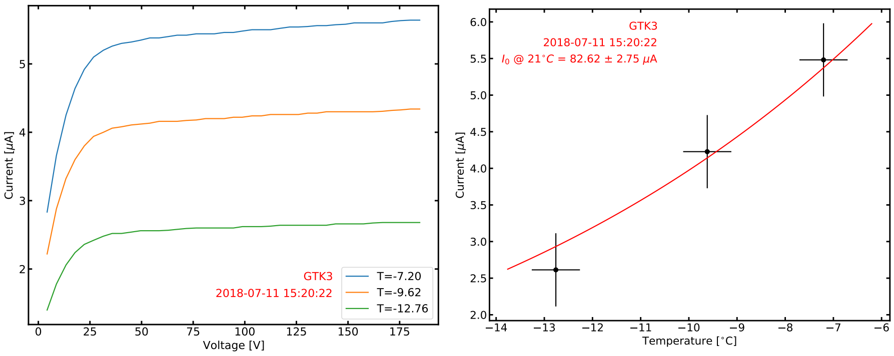

(A) (B)

FIGURE 3.15: (A) Example of the high voltage scan taken during the 2018 data taking period. The leakage current was measured as a function of the bias voltage at three different temperatures. The current saturates at approximately 50 V, indicating that the leakage current is dominated by the bulk component. (B) Example of the bulk current extraction procedure for a reference temperature of 21°C. For each temperature value, the leakage current was taken at the bias voltage of 100 V. The obtained graph of the current as a function of the temperature was then fitted with the exponential function.

failures when detectors were kept warm, indicating the presence of beneficial annealing processes.

Integrated fluence from ARGONION

The GTK integrated fluence was estimated using the beam counter ARGONION. This counter is placed at the end of the NA62 beamline and provides measurements independently of the NA62 trigger and data taking conditions; therefore, it has a complete history of the beam intensity. The integrated ARGONION flux for each GTK module installed in 2016-2018 is shown in Fig. 3.17.

Since the ARGONION counter is placed at the end of the beamline, the particle rates at the ARGONION and GTK are different. Therefore, the ARGONION counts were calibrated using the correlation between the integrated ARGONION flux and the total hits count from each GTK station extracted for the same burst. The total number of GTK hits per burst was obtained using the corresponding information from the TDCpix. Fig. 3.18 shows the typical calibration plot, where the total number of GTK hits per burst is plotted against the integrated ARGONION counts in the same burst. The slopes for each station are then extracted from this plot using linear fits.

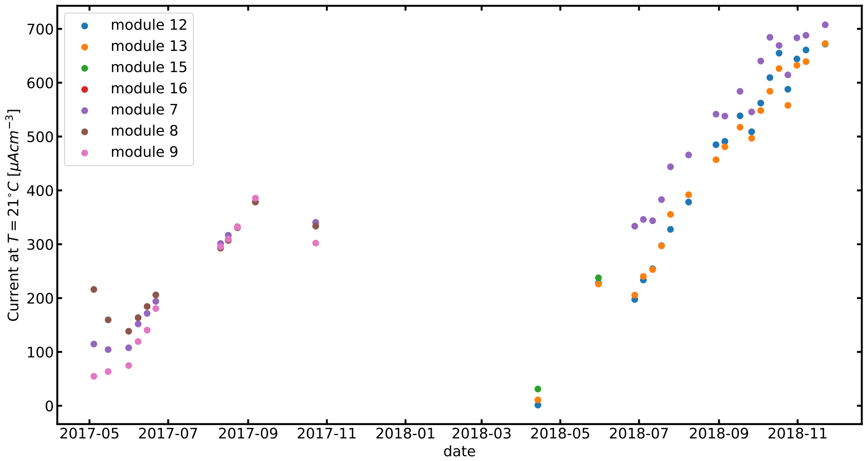

FIGURE 3.16: Bulk leakage current at 21°C normalised to the depleted volume as a function of time for each installed GTK module in 2017-2018 data taking periods. A linear increase in the bulk current is expected due to the sensor irradiation. The small discontinuities in the current are linked to the beneficial annealing processes.

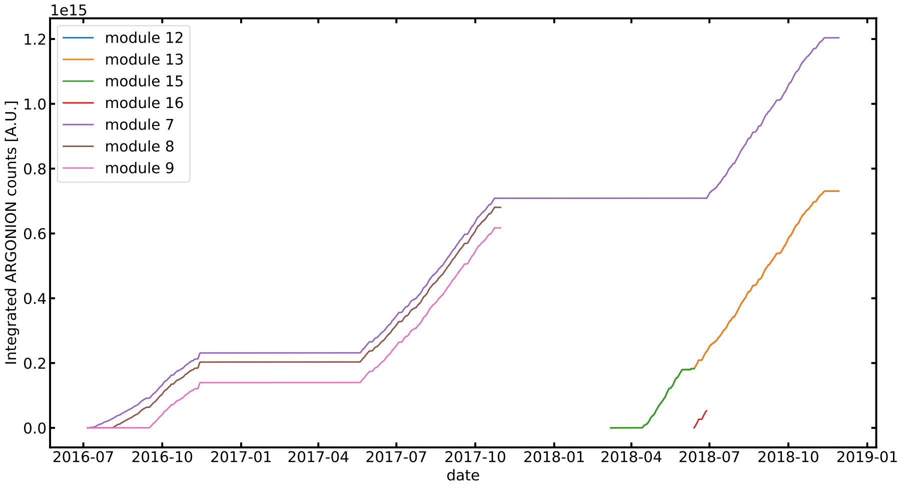

FIGURE 3.17: Integrated particle flux taken from the beam counter ARGONION as a function of time for each GTK module installed in 2016-2018 data taking periods.

The evaluated slopes have to be corrected by a factor of ~ 0.92 to account for particle decays ($\sim 5\%$ of particles will decay between ARGONION and

GTK) and clusters in GTK (GTK has typically $3-4\%$ more hits than crossing particles due to clusters with more than one pixel fired [155]). The resulting values of the slopes are 1.20 (raw 1.30), 1.13 (raw 1.23), 1.12 (raw 1.22) for GTK1, GTK2 and GTK3, respectively. These values remained similar for the whole 2017-2018 data taking period, which was cross-checked from several runs at the beginning and the end of the data taking.[27]

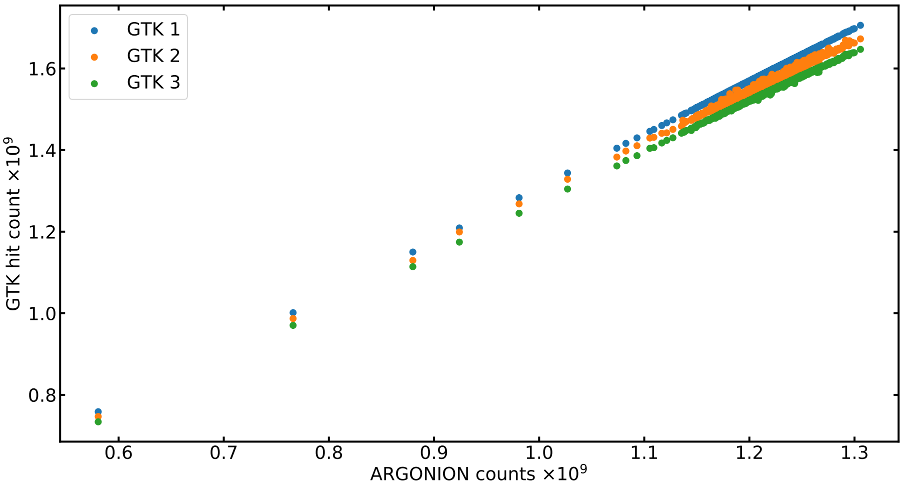

FIGURE 3.18: Total number of hits in a burst per GTK station as a function of total counts in the ARGONION in the same burst. The slopes extracted from this plot are used to estimate the particle flux at each GTK station.

The average integrated fluence for each GTK station was then computed as

$$\Phi_{eq} = \frac{\sum_i Argon^i_{corr} \times \left(f_\pi \cdot \sigma_{\pi\ NIEL} + f_p \cdot \sigma_{p\ NIEL}\right)}{\sigma_{GTK}} \tag{3.13}$$

where $Argon^i_{corr}$ is ARGONION counts for each burst corrected with the slopes discussed above, f_π and f_p are fractions of pions and protons in the NA62 beam – taken as 76% and 24% to account for all particles in the beam, $\sigma_{\pi\ NIEL}$ and $\sigma_{p\ NIEL}$ are the pion and proton NIEL cross-sections normalised to the cross-section of 1 MeV neutrons (0.48 and 0.62 respectively [156]), and σ_{GTK} is the GTK sensor cross-section (2.7×6.08 cm^2). The results of the computation for each module are shown in Fig. 3.19A. It can be noted that the most irradiated module, module 7, reached 4.2×10^{13} 1 MeV n_{eq}/cm^2. Using the average

---

[27] The corresponding plots recently were added to the data quality monitoring routines. The slopes will be available for each run from now on.

fluence and particle rates at GTK3, peak fluence was estimated as shown in Fig. 3.19B. The plot shows that the peak fluence of 1.6×10^{14} 1 MeV n_{eq}/cm^2 was reached. This value is considerably close to the design value listed in Tab. 3.1.

The estimated fluence is currently being validated with the help of the Hamburg model described in section 3.5. Knowing the temperature at which sensors were kept and the integrated fluence, one can estimate the expected value of the leakage current using Eq. 3.10, with α being estimated as in Eq. 3.11. The computed current can then be compared with the one presented in this section. The results of this study, as mentioned previously, are in preparation.

Another parameter that can help to monitor radiation damage is the GTK time resolution discussed in section 3.4. Fig. 3.20A shows the time resolution at the bias voltage of 100 V for each module as a function of average integrated fluence. The same plot but only for module 7 is presented in Fig. 3.20B. These plots show an expected linear correlation between the integrated fluence and the time resolution. Furthermore, the slope of this correlation is approximately the same for each irradiation period for all n-in-p sensors.

Notably, the observed discontinuities in the time resolution match in the time scale the similar structures in the measured bulk current (Fig. 3.16); this was also confirmed by studying the correlation between the estimated time resolution and the measured bulk current. Therefore, this observation suggests that the time resolution can be a useful tool to keep the radiation damage under control along with the leakage current.

Since the NA62 data processing is also running during the data taking, the output of the data quality analysers described in previous sections can be accessed relatively promptly. Therefore, in the future data taking period, a similar study can be done practically online. Combined with the bias voltage scan results, this can be a valuable tool for deciding when the bias voltage must be increased or when the module must be replaced.

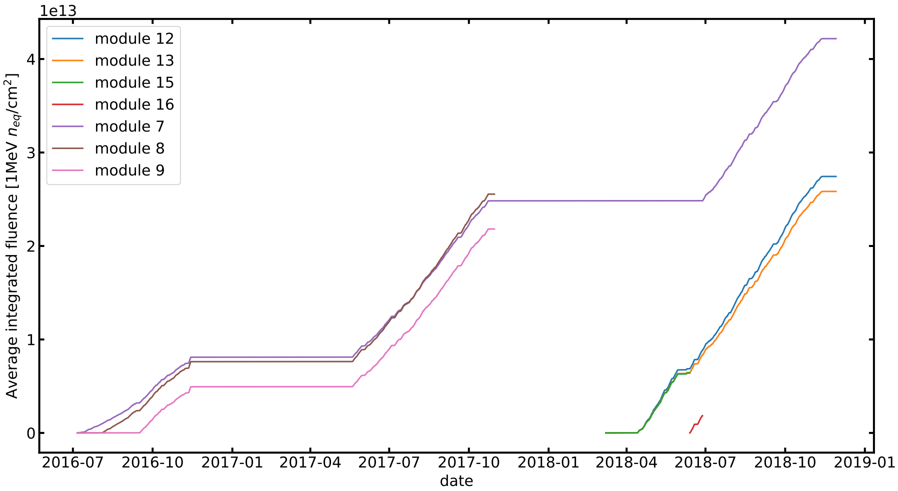

(A)

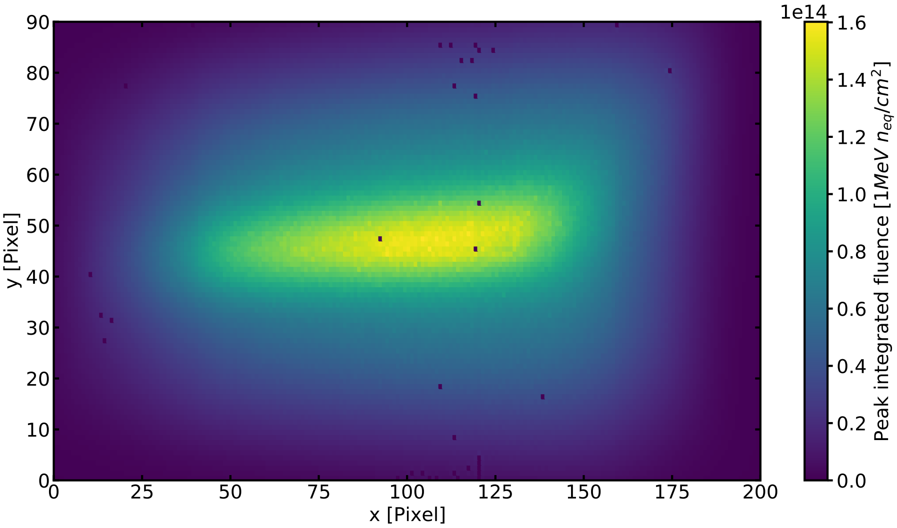

(B)

FIGURE 3.19: (A) Average integrated fluence in 1 MeV n_{eq}/cm^2 as a function of time for each installed GTK module in 2016-2018 data taking periods.(B) Integrated fluence in 1 MeV n_{eq}/cm^2 as a function of pixel coordinates for GTK module 7. In the area around the beam centre, the fluence reached 1.6×10^{14} 1 MeV n_{eq}/cm^2; this value is close to the yearly design fluence.

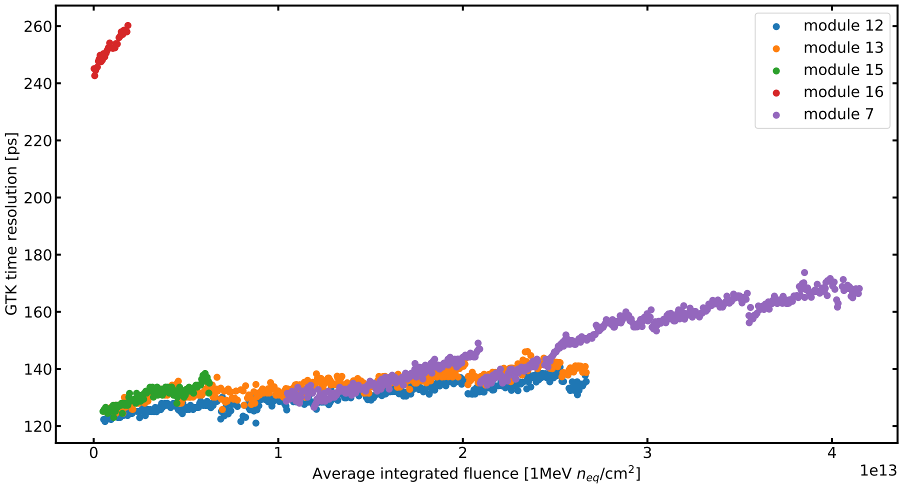

(A)

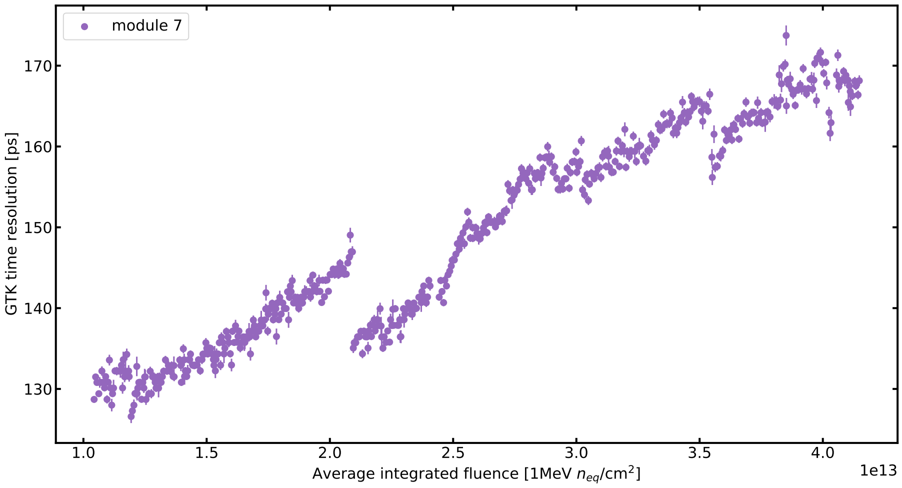

(B)

FIGURE 3.20: (A) Time resolution of each GTK module as a function of average integrated fluence in 2017-2018 data taking periods. The expected linear behaviour is observed for all modules, along with annealing effects hinted at with discontinuities. (B) Time resolution of the most irradiated GTK module, module 7, as a function of average integrated fluence in 2017-2018 data taking periods. The corresponding sensor bias voltage for both plots is 100 V.

3.6 Conclusions

The GTK is the first large scale silicon detector in HEP that achieved a single hit time resolution better than 200 ps. In this chapter, a short overview of the detector elements was provided. The time calibration, the data quality monitoring tools and the detector performances in 2017-2018 data taking periods were discussed. Additionally, a preliminary study of the damages caused by the radiation, including the bulk current measurement and the fluence estimation, was presented. For completeness, however, the obtained average integrated fluence has to be validated, which can be done with the help of the Hamburg model described in this chapter.

The results of the time resolution study, combined with the bias voltage scan performed at the end of the 2018 data taking period, indicate that even after the irradiation of about 4×10^{13} 1 MeV n_{eq}/cm^2, the detector can provide a single hit time resolution better than 150 ps at the bias voltage of 150 V. This finding demonstrates that the old modules can be reused at slightly higher bias voltages. However, the proper investigation of operation stability at higher bias voltages is required to ensure efficient data taking.

This result is of particular interest for the GTK working group since an additional fourth GTK station will be installed in the beamline starting from 2021. Considering the increased detector production rates and the fact that NA62 is going to run for a few more years, the understanding of module lifetimes will become a critical question.

Finally, the automatic time calibration and set of data quality monitoring tools developed within this project will be a valuable instrument in helping to improve the detector performances and keep radiation damage under control during the data taking starting in July 2021.

As the direct consequence of this work, GTK module 7 was installed in 2021 as GTK0 with the bias voltage set to 200 V.

Chapter 4

New Physics searches with the NA62 experiment

Contents

4.1 Introduction

As discussed in the previous chapters, the NA62 experiment was designed to measure the branching ratio of the ultra-rare kaon decay $K^+ \to \pi^+ \nu\bar{\nu}$.

Nonetheless, thanks to its precise tracking, hermetic veto and efficient particle identification systems, NA62 can be used to study other rare processes such as Lepton Number and Flavour Violating decays, decays involving exotic particles as axions and ALPs, HNLs and many others [157, 158, 159, 160, 161].

This chapter is focused on searches for a light spin-0 particle produced in the $b \to s$ transitions, where b-quarks are produced in the NA62 target material. The following sections will provide the description of the production mechanisms, the development of the signal Monte Carlo simulation, the signal selection, and the analysis performed on the data collected by NA62 in 2017 and 2018.

4.2 Light pseudoscalars from rare B-meson decays

The analysis performed in this thesis follows an idea suggested in [94].[28] This paper describes possible approaches for NA62 to search for a light pseudoscalar, axion-like particle (ALP), produced in the $b \to s\mathcal{A}$ processes, where $\mathcal{A}$ is an ALP.

The ALP is assumed to have Yukawa-like couplings to Standard Model fermions described in section 1.3. Therefore the interesting transition $b \to s\mathcal{A}$ can be expressed as:

$$\mathcal{L} \supset h^R_{sb}\mathcal{A}\bar{s}_L b_R + h^L_{sb}\mathcal{A}\bar{s}_R b_L + hc. \tag{4.1}$$

where $q_{L,R} = \frac{1}{2}(1 \pm \gamma^5)q$. The coefficients $h^{L,R}_{sb}$ can be parametrised in terms of a new-physics scale Λ as:

$$h^R_{sb} = \frac{i\alpha\ g_Y\ m_b m_t^2}{4\pi\ m_W^2 sin(\theta_W)^2\ v_{EW}} V_{tb}V^*_{ts} log(\frac{\Lambda^2}{m_t^2}) \tag{4.2}$$

$$h^L_{sb} = \frac{i\alpha\ g_Y\ m_s m_t^2}{4\pi\ m_W^2 sin(\theta_W)^2\ v_{EW}} V_{tb}V^*_{ts} log(\frac{\Lambda^2}{m_t^2}) \tag{4.3}$$

where m_b, m_t, m_W are masses of b-quark, t-quark and W-boson, $\alpha = e^2/(4\pi)$, θ_W is the Weinberg angle, V_{ij} is the CKM matrix element and g_Y is the ALP coupling. The partial decay widths for the flavour-changing B-meson decays are:

$$\Gamma(B \to K\mathcal{A}) = \frac{|h^S_{sb}|^2}{16\pi\ m_B^3} \lambda^{1/2}(m_B^2, m_K^2, m_\mathcal{A}^2) \left| f_0^{B^0}(m_\mathcal{A}^2) \right| \left(\frac{m_B^2 - m_K^2}{m_b - m_s} \right)^2 \tag{4.4}$$

---

[28] The section is based on the paper in [94], and therefore, more details can be found there and in its references.

$$\Gamma(B \to K^* \mathcal{A}) = \frac{|h^P_{sb}|^2}{16\pi\, m_B^3} \lambda^{3/2}(m_B^2, m_{K^*}^2, m_{\mathcal{A}}^2) \left| A_0^{B^0}(m_{\mathcal{A}}^2) \right| \frac{1}{(m_b + m_s)^2} \tag{4.5}$$

with $\lambda(a,b,c) = (a-b-c)^2 - 4bc$ and

$$h^S_{sb} = (h^R_{sb} + h^L_{sb})/2,\ h^R_{sb} = (h^R_{sb} - h^L_{sb})/2 \tag{4.6}$$

The decay form factors $f_0^{B^0}$ and $A_0^{B^0}$ are given by [162, 163, 164]:

$$f_0^{B^0}(q^2) = \frac{0.33}{1 - \frac{q^2}{38\ \text{GeV}^2}} \tag{4.7}$$

$$A_0^{B^0}(q^2) = \frac{1.36}{1 - \frac{q^2}{28\ \text{GeV}^2}} - \frac{0.99}{1 - \frac{q^2}{37\ \text{GeV}^2}} \tag{4.8}$$

Finally, assuming that the pseudoscalar has no other interactions than those with fermions, the dominant decay modes of pseudoscalar are expected to be into the Standard Model leptons. The partial width of such decays can be expressed as:

$$\Gamma(\mathcal{A} \to l^+ l^-) = \frac{g_Y^2\, m_l^2}{8\pi\, v_{EW}^2} m_{\mathcal{A}} \sqrt{1 - \frac{4m_l^2}{m_{\mathcal{A}}^2}} \tag{4.9}$$

The precise branching ratios of the light pseudoscalars are hard to evaluate due to the large uncertainties in the partial width for the hadronic decay modes. In order to avoid this and several other complications, the authors of [94] propose to treat production and decay mechanisms as completely independent parameters. That implies that rather than evaluating the sensitivity of a given experiment in terms of g_Y and $m_{\mathcal{A}}$, as was shown in chapter 1, the results can be presented in terms of $\mathcal{B}(B \to K\mathcal{A}) \times \mathcal{B}(\mathcal{A} \to \mu^+\mu^-)$ and lifetime τ_A for a fixed $m_{\mathcal{A}}$. In principle, $B \to K\mathcal{A}$ and $B \to K^*\mathcal{A}$ should be treated independently; however, if the underlying interactions satisfy the minimum flavour violation hypothesis [165], the coefficients h^R_{sb} and h^L_{sb} can always be written in the form of Eq. 4.2 and Eq. 4.3. Therefore, both partial decay widths, $\Gamma(B \to K\mathcal{A})$ and $\Gamma(B \to K^*\mathcal{A})$, are proportional to $log(\frac{\Lambda^2}{m_t^2})$ and the ratio

$$\frac{\Gamma(B \to K^*\mathcal{A})}{\Gamma(B \to K\mathcal{A})} = \frac{1}{(m_B^2 - m_K^2)^2} \frac{\left| A_0^{B^0}(m_{\mathcal{A}}^2) \right|^2}{\left| f_0^{B^0}(m_{\mathcal{A}}^2) \right|^2} \times \frac{\lambda^{3/2}(m_B^2, m_{K^*}^2, m_{\mathcal{A}}^2)}{\lambda^{1/2}(m_B^2, m_K^2, m_{\mathcal{A}}^2)} \tag{4.10}$$

is independent of Λ and any other model-dependent parameter excluding $m_{\mathcal{A}}$.

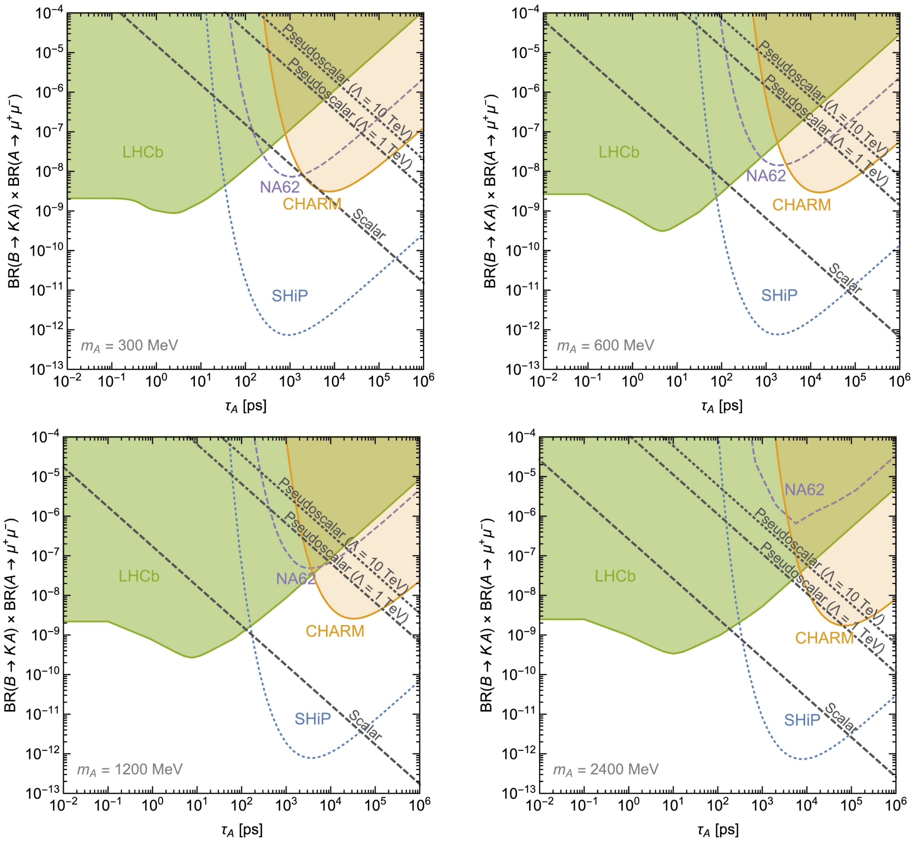

FIGURE 4.1: Model-independent constraints at 95% confidence level on the production and decay of a light pseudoscalar or a scalar expressed in terms of $\mathcal{B}(B \to K\mathcal{A}) \times \mathcal{B}(\mathcal{A} \to \mu^+\mu^-)$ as a function of lifetime $\tau_{\mathcal{A}}$ for four masses: 300 MeV/c^2, 600 MeV/c^2, 1200 MeV/c^2 and 2400 MeV/c^2 [94]. Specific model-dependent predictions are shown as straight lines. NA62 appears to be the most sensitive for masses below 1000 MeV/c^2 and lifetimes around 1000 ps. For further details see [94].

Hence, the two processes can be combined in a single plot. An example of such exclusion bound is shown in Fig. 4.1 for several selected masses. The evaluated limits include the requirement for both muons to be in geometrical acceptance of STRAW chambers 1 and 4, LKr and MUV3. The paper [94] also contains updated constraints on the model-dependent axion-lepton coupling in (g_Y, m_a) plane in the mass range from $2m_\mu$ to 3 GeV, which were not shown in Fig. 1.5. However, in this scenario, the sensitivity of NA62 falls into the parameter region already excluded by other experiments, LHCb and CHARM.

4.3 Analysis strategy

The analysis performed in this thesis follows the model-independent approach described in the previous section. The pseudoscalar particle (ALP) is assumed to be produced in the target or in one of the following beam-dump modules, TAX.[29] The signal signature in this search is a vertex formed by two opposite-charged muon tracks in the final state. Since the exotic particle is assumed to have spin and charge equal to 0 and is feebly interacting, its trajectory is unaffected by magnetic fields and beam elements of the NA62 beamline. Therefore, the total momentum of two muons is supposed to point back to the origin of the initial particle, i.e. target or TAX.

The analysis can be done using data collected in the beam-dump and kaon modes of the NA62 operation. In this thesis, the search using the data collected in the kaon mode was performed. This choice has two main disadvantages.

- The expected background contamination in the kaon mode is higher than in the beam-dump because of the kaon and pion decays before and inside the NA62 apparatus.
- The ALP yield in the kaon mode is slightly lower since a fraction of protons interacts in the lighter material of the T10 target (beryllium) instead of the TAX (copper). Moreover, the muon trigger stream in the kaon mode is typically highly downscaled compared to the beam-dump to spare the bandwidth for the main NA62 trigger dedicated to the $K^+ \to \pi^+ \nu \bar{\nu}$.

However, there is a major advantage in choosing the kaon mode: the statistics collected in the kaon mode is much larger than the one in the beam-dump. Additionally, the quality of the data acquired in the kaon mode is typically higher since often the experiment was running in the beam-dump mode in case of problems with some sub-detectors. To conclude, the analysis in kaon mode has good chances to achieve interesting sensitivity and can be used to complement the analysis done in the dump mode.

Regardless of the choice of the NA62 data collection mode, the expected yield of exotic particles can be estimated as:

$$N_{exp} = POT \cdot N_{b\bar{b}} \cdot \frac{\sigma_{b\bar{b}} \cdot A}{\sigma_{pp} \cdot A^{2/3}} \cdot \sigma(b\bar{b} \to \mathcal{A} \to \mu^+\mu^-) \cdot P_{RD}(\tau) \cdot \varepsilon \qquad (4.11)$$

where

- POT is the delivered number of protons on target;
- $N_{b\bar{b}}$ is the average $b\bar{b}$ multiplicity per proton-proton collision;

---

[29] See section 2.3 for the description of the NA62 beamline.

- A is the atomic mass of the target material;
- the $\sigma_{b\bar{b}}$ is $b\bar{b}$ production cross-section (linearly scales with A);
- σ_{pp} is the total proton-proton interaction cross-section (scales as $A^{2/3}$);
- $\sigma(b\bar{b} \to \mathcal{A} \to \mu^+\mu^-)$ is $\mathcal{B}(B \to K^{(*)}\mathcal{A}) \times \mathcal{B}(\mathcal{A} \to \mu^+\mu^-)$;
- $P_{RD}(\tau)$ is the probability of particle $\mathcal{A}$ being able to reach the NA62 decay volume and decay therein for a given lifetime τ;
- ε is the signal acceptance defined as the fraction of events that have both muons inside the geometrical acceptance of NA62 and pass the signal selection.

The value of $\sigma_{b\bar{b}}$ and $N_{b\bar{b}}$ were obtained from the dedicated `Pythia8` [166] simulation, details of which are provided in section 4.4. The total proton-proton cross-section σ_{pp} for the 400 GeV/c beam was taken as $\sim$ 40 mb as it was done in [94]. The value of ε was computed with the help of the Monte Carlo simulation discussed in section 4.4. Finally, the number of delivered protons on target, POT, was estimated using data. There are two ways to evaluate POT: one is available only in the kaon mode and relies on the estimation of the number of produced kaons, and another one takes the reading of the beam counter T10 installed right after the target. Both approaches will be discussed in more detail in section 4.8.1.

The possible background contribution can be split into two groups: prompt background and combinatorial background. Main sources of prompt background in the kaon data taking mode are kaon decays with pions or muons in the final state as $K^+ \to \pi^+\pi^+\pi^-$ or $K^+ \to \pi^+\mu^+\mu^-$ with $\mathcal{B} = (5.583 \pm 0.024)\%$ and $\mathcal{B} = (9.4 \pm 0.6) \times 10^{-8}$ respectively. Another possible but less likely contribution can come from decays of mesons produced in the interactions of beam particles in the magnets or other beam elements upstream of the decay volume, particularly decays of K_S. Finally, it is possible that a pair of muons can be produced in the conversions of photons in the beam elements upstream of the decay volume; however, this contribution is expected to be small as well. The combinatorial background can be any random combination between products of kaon decays and decays of other mesons, mostly beam pions. The preliminary background estimation is discussed in section 4.9.

The analysis is performed using a blind methodology, where the selected signal region is masked until the end of the analysis. The prediction of the background inside the signal region was made using data, while the Monte Carlo was used for trigger efficiency studies. The background is estimated for each search window using the dimuon invariant mass distribution. The definition of search windows is related to the resolution of the invariant mass, which was estimated from Monte Carlo.

The following sections will describe the data samples, trigger streams, and data filters used in this analysis.

4.3.1 Data samples

The analysis is performed using data collected during the 2017 and 2018 data taking periods. The data samples and the corresponding versions of the NA62 analysis and reconstruction software are given in Tab. 4.1. In the 2017D sample, the trigger time window was 12.5 ns, while starting from 2017C, it changed to 6.25 ns. An additional beam component, a copper plug, was installed in the last magnet of the GTK achromat before 2017A. The change was necessary for the $K^+ \to \pi^+ \nu\bar{\nu}$ analysis to suppress background from upstream decays. Later, the final collimator was replaced by a larger one to reduce the upstream background further. The changes took place starting from the 2018D sample. The samples after 2018E were taken at a higher intensity – $\sim 50 - 100\%$ of the nominal.

Sample	Run range	Number of bursts	Software version
2017A	8134-8282	83940	v2.1.7
2017B	7876-8107	151466	v2.1.5
2017C	7735-7873	31537	v2.1.4
2017D	7615-7721	42218	v2.1.4
2018A	8518-8535	17306	v2.0.3
2018B	8548-8740	105350	v2.0.4
2018C	8777-8799	18005	v2.0.4
2018D	8802-8967	107665	v2.0.4
2018E	8968-9040	77684	v2.0.4
2018F	9047-9134	71315	v2.0.4
2018G	9147-9271	93803	v2.0.3
2018H	9306-9462	38063	v2.0.3

TABLE 4.1: Summary of data samples used for the analysis presented in this thesis. The "Number of bursts" column shows all available bursts in a given sample. The data samples are ordered alphabetically.

4.3.2 Trigger streams

The analysis uses mainly two triggers: the Dimuon exotic trigger and the Control trigger.

The Control trigger is used for studies of random activity in NA62 veto subdetectors and L0 trigger efficiencies. Both studies will be described in the dedicated sections. The Control trigger selects any charged particle producing a coincidence of signals in the overlapping vertical and horizontal slabs of the NA48 CHOD within a 6.25 (12.5 in 2017D sample) ns time window. The trigger is downscaled by 400,[30] and no L1 condition is applied.

The Dimuon exotic trigger is designed to select events with at least two muons in the final state. During 2017-2018 the trigger conditions were multiple times redefined. All variations of the trigger stream used in this analysis are shown in Tab. 4.2, the definitions of listed L0 and L1 conditions are given below.

Year	Run range	L0 trigger	L1 trigger
2017	7600-7647	RICH-Q2-MO2	STRAW exotics
2017-2018	7648-8586	RICH-QX-MO2	STRAW exotics
2018	from 8587	RICH-Q2-MO2-!LKr10	STRAW DV5

TABLE 4.2: Summary of variations of the Dimuon trigger stream used for the analysis presented in this thesis.

Typically a downscaling factor of 3 or 2 was applied throughout all the data taking. The history of the downscaling factor for the Dimuon trigger stream is shown in Fig. 4.2A.

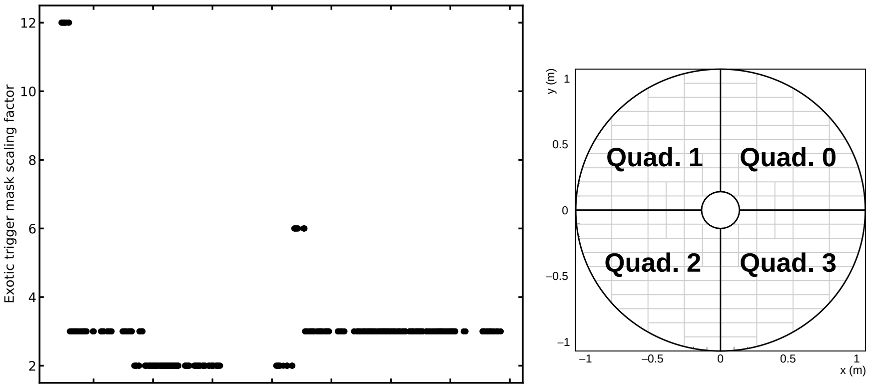

(A)

(B)

FIGURE 4.2: (A) Downscaling factor of the Dimuon trigger stream in 2017 and 2018 data taking periods. Typically a value of 3 or 2 was used. The changes in the downscaling mostly overlap with modifications in the trigger definitions. (B) Map of the Charged Hodoscope (CHOD) quadrants which are used for the L0 trigger definitions.

---

[30] As mentioned in section 2.14, NA62 L0 triggers can have a programmable downscaling factor.

L0 RICH

RICH condition selects events with at least two RICH hits in a 6.25 (12.5 in 2017D sample) ns time window.

L0 QX and Q2

QX and Q2 conditions are based on signals in the CHOD detector. At the L0 trigger level, the detector is divided into four equal parts; each called a quadrant. The CHOD quadrant map is shown in Fig. 4.2B. The QX condition requires at least two hits in two diagonally opposite quadrants in a 6.25 (12.5 in the 2017D sample) ns time window. The Q2 condition is more relaxed and requires at least two hits in two different quadrants in the same time window as QX.

L0 MO2

The L0 MO2 condition is based on signals from muon veto detector MUV3. At the L0 level, the detector is divided into inner and outer regions: the eight tiles surrounding the beam pipe are considered inner. The MO2 condition selects events that have at least two hits in the outer region of the detector in a 6.25 (12.5 in 2017D sample) ns time window.

L0 LKr10

The L0 LKr10 condition is based on the total energy of the reconstructed clusters in the LKr calorimeter. The trigger accepts all events where the released energy is larger than 10 GeV. This condition is used as a veto in the Dimuon trigger to reject events with pions more effectively.

L1 STRAW exotics

L1 STRAW exotics aims at identifying decay channels with a negatively charged particle in the final state. The algorithm performs a simple track reconstruction and accepts events with at least one track satisfying the following conditions:

- longitudinal track momentum is between 3 and 100 GeV/c;
- track slopes θ_{XZ} and θ_{YZ} are within ± 20 mrad;
- negative charge.

L1 STRAW displaced vertex (DV)

The L1 STRAW displaced vertex (DV) algorithm was designed specifically for exotic decay channels like the one studied in this thesis. The main idea of this trigger is to suppress kaon decays by selecting events with two-track vertices displaced with respect to the kaon beamline. The algorithm accepts events with at least two reconstructed tracks which satisfy the following conditions:

- opposite charge;
- tracks form a vertex with the Closest Distance of Approach (CDA) between the two tracks less than 30 mm;
- CDA between vertex and the nominal kaon beamline is more than 5 (loose) or 10 cm (tight);
- longitudinal track momentum is between 3 and 100 GeV/c;
- track slopes θ_{XZ} and θ_{YZ} are within ±20 mrad.

It is worth mentioning that the implications of the cuts on track momenta were not fully grasped before the trigger studies described in section 4.8.3 were made. The impact of these cuts will be discussed in more detail in section 4.8.3.

Data filters

To reduce the amount of stored data, the reconstruction output is filtered into multiple data sets, which can later be used for physics analysis. In this work, three filters, `HNL`, `CTRL` and `RES3TV`, were used. The description of each filter is provided below.

The `HNL` filter selects events that passed the exotic trigger, the Dimuon trigger in particular, with at least one pair of tracks forming a vertex with the closest distance of approach (CDA) to each other less than 50 mm and the minimal distance to the kaon beamline greater than 100 mm. The two tracks should be inside the geometrical acceptance of all STRAW chambers, NA48 CHOD, MUV3 and LKr. Additionally, the `HNL` filter requires a special mode of the STRAW track reconstruction, which does not reject the tracks with momentum higher than 90 GeV/c as in the standard mode. The output of this filter is used for the main analysis.

The `CTRL` filter is very simple and accepts every 25th event passing minimum bias Control trigger. As mentioned before, it is used for studies of random activity in the veto detectors as LAV, SAV, LKr and CHANTI.

Finally, the `RES3TV` filter selects events with at least one good three track vertex defined as

- vertex χ^2 is below 40;
- vertex Z position is above 102.4 m;
- the total momentum of the vertex is below 90 GeV/c;

- all tracks are in acceptance of all STRAW chambers;
- minimal distance between tracks forming the vertex at the first STRAW chamber is above 10 mm.

This filter is used for the estimation of the number of protons on target.

Event quality

In all studies discussed in this chapter, data events and bursts marked with the bad quality flag for all detectors, except for MUV0 and HASC, were discarded. That is because the candidates and hits from these detectors were not considered in the analysis.

4.4 Signal Monte Carlo

In the NA62MC, the simulation of processes that include Beyond the Standard Model particles can be done via three different mechanisms. The first mechanism is connected to the `Turtle` generator [130] and handles the production of exotic particles in decays of kaons and pions. The second method handles only HNLs produced in decays of D-mesons.[31] Finally, the last mechanism is responsible for simulating two-body decays of exotic particles (ALP, Dark Photon and HNL), their direct productions in the target and TAX material, and the production in the decays of various mesons. The model described in section 4.2 was implemented in the last mechanism called the exotic generator. The author of this thesis was one of the main contributors to the source code for the generator, in particular, by introducing the new production mechanism and maintaining the existing ones.

The exotic generator relies on several input parameters, such as the particle mass, particle decay type (only Standard Model decay products are supported), production mode, range of exotic particle decay Z position and coupling strength. Typically, the coupling strength is set to 1, which allows studying different models using the same Monte Carlo output.

The generator works in the following way. The event simulation starts with the random generation of the production position in the target material. The material can be set in the configuration file to either T10 target, TAX or a combination between the two. If the latter option is selected, 60% of events are generated in the T10 material and the other 40% in the TAX. Indeed, the interaction probability can be computed as

$$\epsilon = 1 - e^{-l/\lambda} \tag{4.12}$$

---

[31] The dedicated description can be found in [167].

where l is the length of the material and λ is the nuclear interaction length of the material. In the case of the target T10, $l = 400$ mm and $\lambda = 421$ mm, while in the case of the TAX $l = 3230$ mm and $\lambda = 153$ mm. Inserting the numbers in Eq. 4.12, one obtains 0.613 for the T10 target and $0.999(9)$ for the TAX. Therefore, in the kaon mode of NA62 data taking, only 40% of protons will interact in the TAX material. The material factor A from Eq. 4.11 is not considered at this stage and has to be applied as a weight on already generated events.

X and Y coordinates of the production position are randomly sampled from a 2D histogram of proton distribution at the selected plane. The corresponding distributions at target and TAX (Fig. 4.3) were obtained from the dedicated K12 beamline simulation described in detail in [168], and stored as a histogram in `.root` format. The Z coordinate of the interaction position at target T10 or TAX is calculated as:

$$Z = -\lambda_i \cdot ln(1 - \epsilon_i \cdot f_{rand}) \tag{4.13}$$

where $i = \{T10, TAX\}$, λ_i is the nuclear interaction length of the corresponding material, ϵ_i is the interaction probability in the corresponding material, and f_{rand} is a random number uniformly distributed between 0 and 1.

The kinematic parameters of the primary particle produced in the proton-nucleon interaction are randomly sampled from a 2D histogram. In the case of direct exotic production, the 2D histogram is obtained from a dedicated toy-MC simulation developed for a given model. Otherwise, the 2D histogram is filled with the output of the custom-made `Pythia8` simulation of meson production in proton-proton or proton-neutron interactions. The 2D histogram contains the track polar angle θ as a function of the track momentum p. The azimuthal angle ϕ is generated as a uniformly distributed random number in the range of 0 to 2π. The momentum components are then computed as follows:

$$p^X_{init} = p \cdot cos(\phi) \cdot sin(\theta) \tag{4.14}$$

$$p^Y_{init} = p \cdot sin(\phi) \cdot sin(\theta) \tag{4.15}$$

$$p^Z_{init} = p \cdot cos(\theta) \tag{4.16}$$

An example of the 2D histogram described above for B^+ meson is shown in Fig. 4.4. The histogram was obtained from the `Pythia8` simulation made with the following settings:

- only hard $b\bar{b}$ processes are generated;
- PDF set 2 is selected, which corresponds to the leading-order 5L set from the CTEQ collaboration [169];

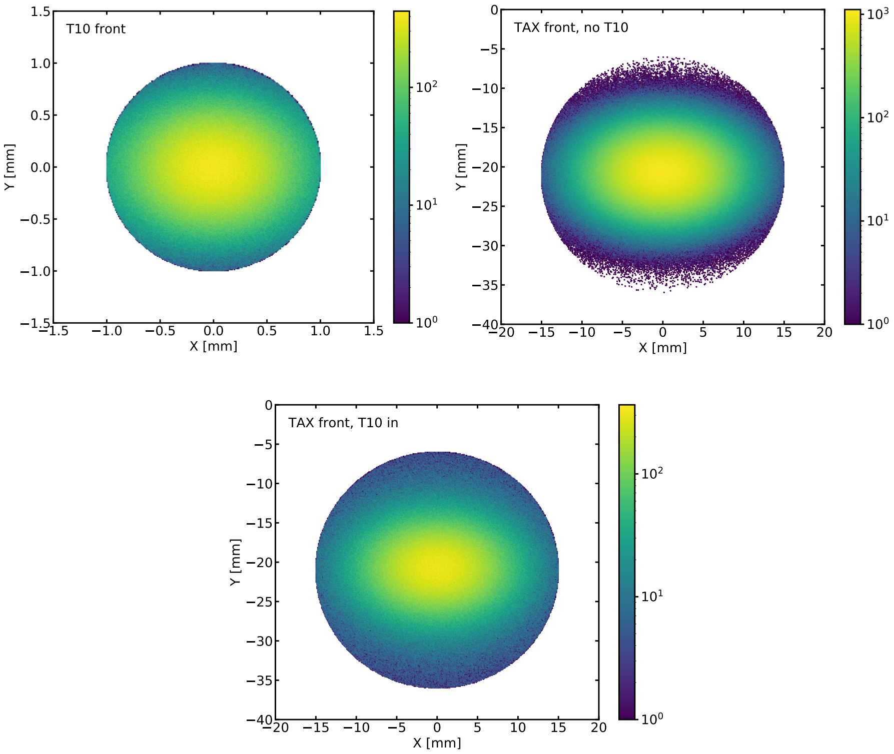

FIGURE 4.3: Proton distributions on the target and TAX front planes obtained with the help of the dedicated beamline simulation described in [168]. The distributions are used to sample the primary production position in the exotic Monte Carlo.

- mass of b-quark is set to 4.2 GeV/c^2;
- minimum invariant transverse momentum is set to 300 MeV/c;
- center of mass energy is set to 27.4 GeV/c corresponding to the collision of a 400 GeV/c beam with a fixed target.

As a result, the $b\bar{b}$ cross-section of 1.868 nb and the average $b\bar{b}$ multiplicity of $N_{b\bar{b}} \sim 1.66$ were obtained. These numbers are in agreement with the existing literature [170]. Only B^0, B^+, B_s and their antiparticles were saved in the output of the simulation.

A small rotation in the X and Y axis is added to the particle momentum depending on the production position to account for the non-parallel beam at the TAX plane. The rotation parameters are also taken from the beamline simulation and saved as 2D histograms for two cases: when the T10 target is present

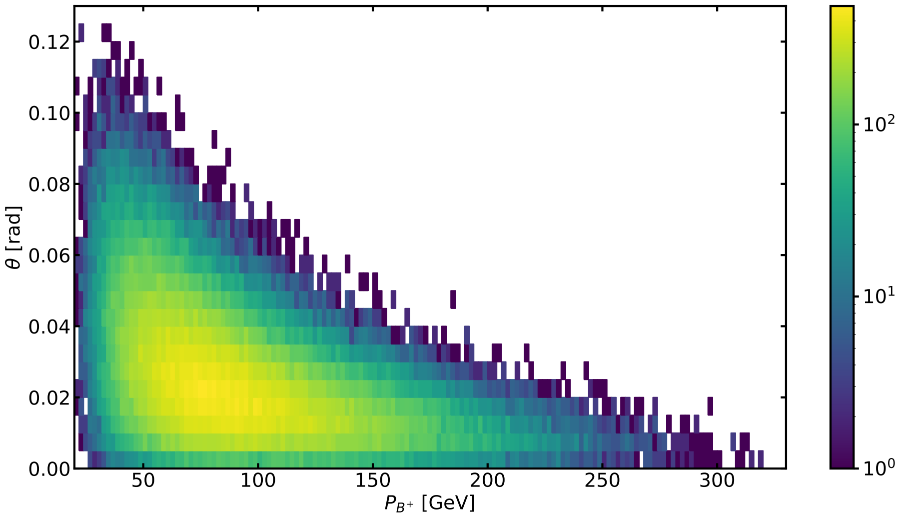

FIGURE 4.4: Distribution of the polar angle as a function of the track momentum for B^+ mesons produced in the interaction of the 400 GeV/c proton beam with the fixed target. The plot was obtained from the dedicated `Pythia8` simulation described in the text.

(kaon mode of data taking) and when removed (beam-dump mode). Fig. 4.5 demonstrates the 2D histograms with the proton beam angular distribution at X and Y planes as a function of the X and Y coordinate, respectively. The rotation in X (θ_X) and in Y (θ_Y) is then applied as:

$$\vec{p} = \begin{bmatrix} 1 & 0 & 0 \\ 0 & cos(\theta_X) & -sin(\theta_X) \\ 0 & sin(\theta_X) & cos(\theta_X) \end{bmatrix} \cdot \begin{bmatrix} cos(\theta_Y) & 0 & sin(\theta_Y) \\ 0 & 1 & 0 \\ -sin(\theta_Y) & 0 & cos(\theta_Y) \end{bmatrix} \cdot \vec{p}_{init} \tag{4.17}$$

After the coordinates and momentum of the primary particle at the production point are set, the simulation proceeds with its decay. For exotic particles, it is assumed that they are unaffected by the magnetic fields of the NA62 beamline, and therefore, can be extrapolated linearly to the Z position randomly selected from a uniform distribution in the defined decay region. For mesons, the distance travelled before the decay is computed as

$$l = -\lambda \cdot ln(1 - f_{rand}) \tag{4.18}$$

where f_{rand} is a random number uniformly distributed between 0 and 1, λ is the meson decay length computed as $\lambda = \gamma\beta c\tau$ with γ being the Lorentz factor, c – speed of light, $\beta = v/c$, and τ – meson lifetime.

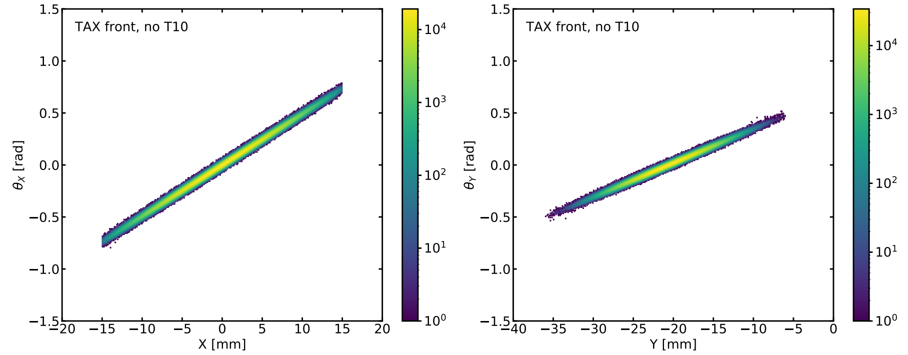

FIGURE 4.5: Angular distribution of protons as a function of the impact position at the TAX front plane. Angles and positions in the X-axis are shown in the left plot, while Y-axis is demonstrated on the right. The plots were obtained with the help of the dedicated beamline simulation described in [168].

At the rest frame of the primary particle, the momentum for products of the two-body decay is computed as:

$$p_1 = \frac{\sqrt{(M_{init}^2 + m_1^2 - m_2^2)^2 - 4M_{init}^2 m_1^2}}{2M_{init}} \tag{4.19}$$

$$p_2 = \frac{\sqrt{(M_{init}^2 + m_2^2 - m_1^2)^2 - 4M_{init}^2 m_2^2}}{2M_{init}} \tag{4.20}$$

The azimuthal and polar angles are selected randomly from a uniform spherical distribution; momenta components are set as in Eq. 4.14. The decay products are then boosted in the laboratory frame using the three-momentum of the parent particle, where each component is divided by the value of the particle energy. In the case of the exotic particle decay, charged daughter particles are extrapolated to the front plane of the NA48 CHOD detector to optimise the use of computing resources. If the extrapolated position of any of the particles is outside the NA48 CHOD geometrical acceptance, the kinematics of the event is regenerated until the successful configuration is found. Then, the generated decay products are passed to `Geant4`, which tracks them through the NA62 apparatus. All relevant information about failed and successful generation attempts, namely, the production and decay positions, the momentum of the exotic particle and its parent meson, if any, are saved in the output file. This bookkeeping is necessary for further geometrical acceptance evaluation, which must account for exotic particle lifetime. An example of momentum distributions of ALP produced in decays of B-mesons and its daughters is

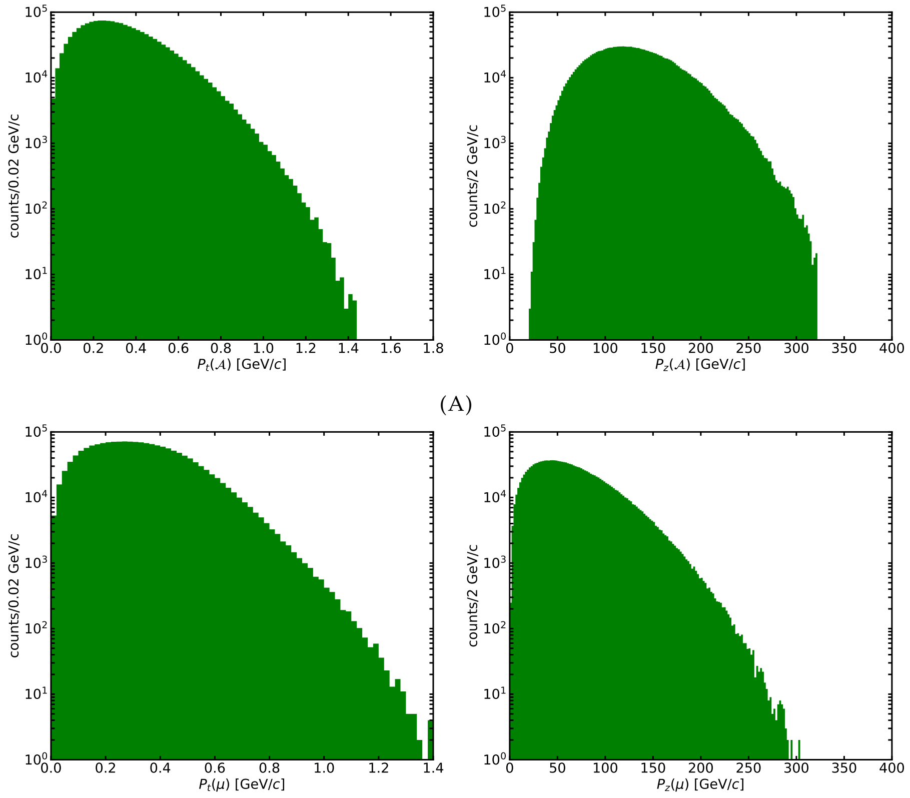

(A)

(B)

FIGURE 4.6: Transverse and longitudinal momentum distributions for (A) ALP produced in B-meson decays; (B) muons produced in ALP decays. The plots are obtained using the MC output. The ALP lifetime was not taken into account.

shown in Fig.4.6.

The generator allows for the simulation of multiple production modes of the same exotic particle, taking into consideration partial decay widths or production probabilities. In the case of B-mesons, partial decay widths for all possible $B \to K/K^*\mathcal{A}$ scenarios are computed with the help of Eq. 4.4 and 4.5. As shown in [94] and in Eq. 4.10, the ratio between $B \to K\mathcal{A}$ and $B \to K^*\mathcal{A}$ is model-independent; therefore, the generated mixed samples can be used for both model-dependent and model-independent studies.

The samples of the signal Monte Carlo described in this section were generated with the dedicated `Git` tag of the NA62 Framework.[32] The sample consists of masses from 250 to 1050 MeV/c^2 generated with the step of 25 MeV/c^2 and with 50000 events for each mass. The ALP is requested to decay in the Z range between 105 and 180 m corresponding to the standard NA62 decay region. All $B \to K^{(*)}\mathcal{A}$ decay modes are generated together, and meson production in the target T10 and TAX is requested.

4.5 Signal selection

A dedicated event selection has been developed with the main goal to minimise the background contribution and maximise the signal yield. In short, the selection looks for a well reconstructed two-track vertex composed of opposite-charged tracks identified as muons; the vertex must be displaced from the nominal beamline and should point back to the expected production position at the TAX or the target T10.

There is a minor difference between the selection used on data and on the signal MC: on data, the trigger selection is made before any of the cuts, while on the Monte Carlo, it is applied at the very end.

Vertex selection

The vertex is reconstructed with the help of the standard NA62 tool `SpectrometerVertexBuilder` (see 2.15). The selection first identifies all good vertices reconstructed in the event and then rejects events with more than one good vertex. The vertex is identified as good if it satisfies the following criteria:

- All tracks inside the vertex are well reconstructed, such that the following conditions are satisfied for each track:
  - track is not marked as fake;
  - track fit $\chi^2 < 40$;
  - track has hits in at least 3 chambers of the STRAW spectrometer;
  - difference between reconstructed track momentum before and after the fit is less than 20 GeV/c;
- distance of the closest approach (CDA) between two tracks inside the vertex is less than 20 mm;
- time difference between the vertex time and trigger time (measured with RICH) should be within ±12 ns.

---

[32] The tag can be found in the NA62 `Git` repository: `gitlab.cern.ch/NA62FW/na62fw/-/tags/t-exoticmc-test-louvain` (available for members of NA62 Collaboration only).

The vertex time is computed as the weighted average of track times, accounting for the time resolution of the associated detectors. The track times here are taken from the track association with NA48 CHOD and CHOD detectors. The rejection of events with additional two-track vertices allows reducing the contribution from multitrack events such as $K^+ \to \pi^+\pi^+\pi^-$.

After an event with a single good vertex is selected, tighter cuts on the vertex quality are applied:

- vertex total charge is 0;
- vertex fit $\chi^2 < 10$;
- vertex Z position must be within $110 - 180$ m to reject possible contribution from the beam interactions in upstream beam elements;
- distance from the vertex to any of the tracks in the event should be above 50 mm to further suppress contribution from the multitrack events;
- CDA between vertex and the nominal beamline must be above 100 mm to suppress the majority of multitrack kaon decays;
- CDA between two tracks in the vertex must be below 10 mm.

Finally, both tracks in the vertex are required to be in the geometrical acceptance of STRAW, NA48 CHOD, LKr and MUV3. Additional cuts on track qualities are applied as:

- track fit $\chi^2 < 20$;
- track momentum above 10 GeV/c for better reconstruction and particle identification efficiency.

Timing cuts

In this analysis, multiple timing cuts are applied to suppress the combinatorial background:

- the time difference between the vertex time (defined above) and the trigger time (from RICH) should be within ±3 ns;
- there must be an associated NA48 CHOD candidate for each of the tracks;
- the time difference between two tracks using NA48 CHOD time must be within ±3 ns. The associated candidates should not be identical.

Additionally, the presence of a CHOD candidate associated with each of the tracks is required. The vertex time is taken as an event reference time. It is defined as a weighted average between NA48 CHOD and CHOD times associated with the tracks, where the weights are the resolutions of NA48

CHOD (200 ps) and CHOD (1 ns). The track time is always measured with NA48 CHOD.

Track separation

In order to provide higher track reconstruction efficiency and better association with the downstream detectors, the track separation criteria at the first STRAW chamber and the front plane of the LKr calorimeter are applied:

- the distance between two tracks at STRAW1 must be above 20 mm;
- the distance between two tracks at LKr must be above 100 mm.

Particle identification

Since both tracks are muons, both tracks are required to have an association in the outer tiles of the MUV3 detector. Furthermore, the associated tiles should not be the same for both tracks. Finally, the time difference between the associated MUV3 candidate and the track time must be within ±3 ns.

Additionally, track association with a cluster in LKr is checked. The event is accepted if, for any of the two tracks, one of the conditions is satisfied:

- there is no track-LKr association;
- the track-LKr association exists and
  - only one cluster is associated;
  - the distance between the track position at LKr and the associated track is within 20 mm;
  - the ratio of the associated cluster energy and the track momentum is below 0.2;
  - the distance to the closest dead cell of LKr is greater than 20 mm.

Veto

To suppress the background coming from muon halo, products of kaon and pion decays before the NA62 decay volume, and kaon decays with photons in the final state, the following selection criteria are applied:

- there must be no hits in SAV detectors in ±3 ns with the event time;
- veto events with at least 2 hits in LAV detectors in ±3 ns with the event time and with hit Z position greater than the vertex Z position;
- for each track there must be no association with CHANTI candidate in ±3 ns with track time;

- veto events with additional in time clusters in LKr, where the timing criteria are applied as in [171].

The cuts defined above were optimised using data since they can introduce an accidental veto due to the random activity in the corresponding detectors. These studies are going to be discussed in the dedicated section of this chapter.

To suppress the contribution from $K^+ \to \mu^+ \nu$ decay ($K\mu2$), which can create a signal-like vertex with a negative muon from the halo, the events which satisfy all following conditions are rejected:

- there is a KTAG candidate in ±3 ns with positive track time and with the number of fired sectors higher than 4;
- CDA between the positive track and the nominal beamline is below 20 mm, and the Z position of the CDA is between $100 - 180$ m;
- the momentum of the positive track is below 70 GeV/c;
- the squared missing mass is $|(P_K - P_\mu)^2| < 0.015$ GeV$^2/c^4$, where P_K is the 4-momentum of the kaon assuming the nominal beam momentum and P_μ is the 4momentum of the positive muon track.

Signal region

Finally, since the production either in the target T10 or in the TAX is assumed, the region blinded in data is defined as follows:

- extrapolate the total momentum from the selected vertex to the front plane of the target T10 and TAX;
- compute the distance between the impact point (IP) and the projected vertex. In the case of T10, IP is assumed to be $(0, 0)$ mm, while for TAX, it is $(0, -20)$ mm;
- select the minimum distance to the IP between TAX and T10;
- compute the CDA between the vertex and the nominal kaon beamline, and get the corresponding Z position;
- select events if the following conditions are satisfied
    - the minimum distance to the IP is less than 20 mm;
    - the Z position of vertex-nominal beam CDA is between -10 and 40 m.

The illustration of the signal region described above is shown in Fig. 4.7. The plot was made using the signal Monte Carlo with all generated masses, no weights applied. The red line indicates the borders of the selected signal region.

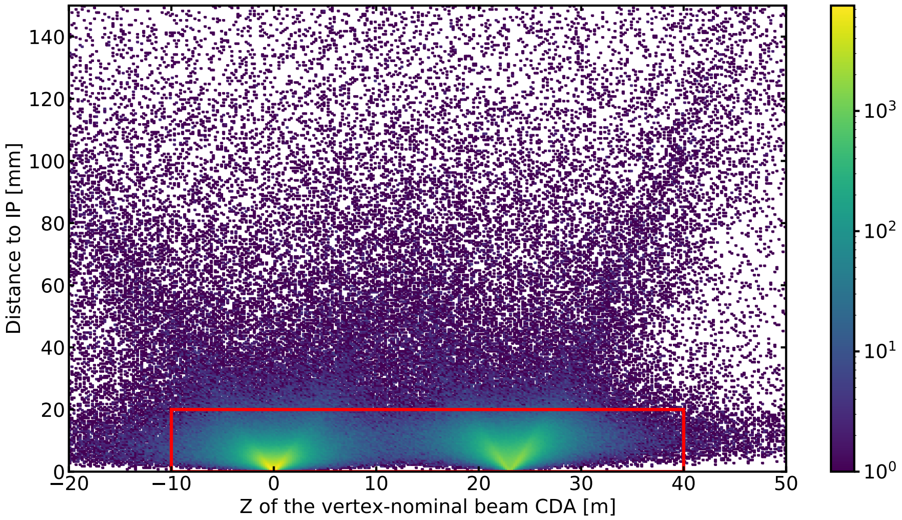

FIGURE 4.7: Minimum distance to the impact point (IP) as a function of Z position of the closest distance of approach (CDA) between the dimuon vertex and the nominal beam. The red box illustrates the selected signal region. For more details, see the text. The plot was made with the signal MC, and particle lifetime was not taken into account.

4.6 Sensitivity studies

The expected signal events are estimated using Eq. 4.11, but the production in the target T10 and the TAX is now considered. The equation is then rewritten to account for different materials of the target T10 and the TAX as

$$\begin{aligned} N_{exp} = POT \cdot N_{b\bar{b}} \cdot \frac{\sigma_{b\bar{b}}}{\sigma_{pp}} \cdot \sigma(b\bar{b} \to \mathcal{A} \to \mu^+\mu^-)\cdot \\ \cdot \sum_{i=1}^{T10,TAX} (A^i)^{1/3} \cdot f^i \cdot P^i_{RD}(\tau) \cdot \varepsilon^i_{acc} \end{aligned} \tag{4.21}$$

where f^i is the interaction probability in the target T10 or TAX, 60% and 40% respectively (see 4.12), ε^i_{acc} is the total acceptance of $B \to K^{(*)}\mathcal{A}, \mathcal{A} \to \mu^+\mu^-$, and ε_{RV} is the probability of the event to pass the veto conditions in the presence of accidental activity in the detectors used in the selection.

In principle, the f^i factor is already included in the MC simulation output, and the material factor can be added as a weight to $P_{RD}(\tau)$ and ε^i_{acc} computation; however, since the TAX component needs to be checked separately, the expression from Eq. 4.21 is used.

The full acceptance ε_{acc} is estimated by multiplying the geometrical acceptance by the selection efficiency. The selection efficiency and the geometrical acceptance of muons from $B \to K\mathcal{A}$, $\mathcal{A} \to \mu^+\mu^-$ processes were evaluated using the signal MC. The geometrical acceptance was estimated as

$$\varepsilon_{geom} = \frac{\sum_{i=1}^{N_{in\ acc}} w_i}{\sum_{i=1}^{N_{all\ gen}} w_i} \tag{4.22}$$

where $\sum_{i=1}^{N_{in\ acc}}$ is the sum over all events in the acceptance of STRAW chambers 1 and 2, NA48 CHOD (required on the event generation level), LKr and MUV3, $\sum_{i=1}^{N_{all\ gen}}$ is the sum over all generated events, and w_i is a weight applied to each event to correct the initially uniform decay distribution of an ALP and defined as

$$w_i = \frac{1}{\gamma_i \beta_i c\tau} \cdot e^{-\frac{Z_i^{decay} - Z_i^{prod}}{\gamma_i \beta_i c\tau}} \tag{4.23}$$

Similarly, the selection efficiency was estimated using $N_{selected}$ and $N_{in\ acc}$ instead of $N_{in\ acc}$ and $N_{all\ gen}$. In this analysis, acceptances depend only on the lifetime τ and the mass of the particle. Indeed, since the production and decay probabilities were considered to be independent parameters, for a given production probability, the value of $\sigma(b\bar{b} \to \mathcal{A} \to \mu^+\mu^-)$ will enter both in the numerator and in the denominator of Eq. 4.22. Considering that $\sigma(b\bar{b} \to \mathcal{A} \to \mu^+\mu^-)$ is a constant in this analysis,[33] its value cancels out in the acceptance computation. Fig. 4.8 shows the geometrical, selection and full acceptances as functions of the mass and the lifetime separately for productions in the TAX and target T10. The geometrical acceptance of ALPs, as can be seen from Fig. 4.8, depends on the mass and the lifetime: the probability of getting into the NA62 acceptance increases with shorter lifetimes and smaller masses. The mass dependence originates from the fact that the transverse momentum of muons increases with the ALP mass. This increase, in turn, reduces the probability of having both muons in the NA62 acceptance. However, events with heavy ALPs that pass geometrical acceptance criteria have a better separation between muon tracks in the downstream detectors, increasing the selection efficiency.

The parameter $P_{rd}(\tau)$ from Eq. 4.21 depends only on the simulated lifetime and the ALP decay Z range. Since this parameter is the acceptance of ALP to reach the NA62 decay volume and decay somewhere inside, it is computed as follows:

$$P_{rd}(\tau) = \frac{1}{N_{all\ gen}} \cdot \sum_{i=1}^{N_{all\ gen}} e^{-\frac{Z^{FVs} - Z_i^{prod}}{\gamma_i \beta_i c\tau}} \cdot (1 - e^{-\frac{Z^{FVs} - Z^{FVe}}{\gamma_i \beta_i c\tau}}) \tag{4.24}$$

---

[33] Note that Monte Carlo already takes into account probabilities of $B \to K$ and $B \to K^*$.

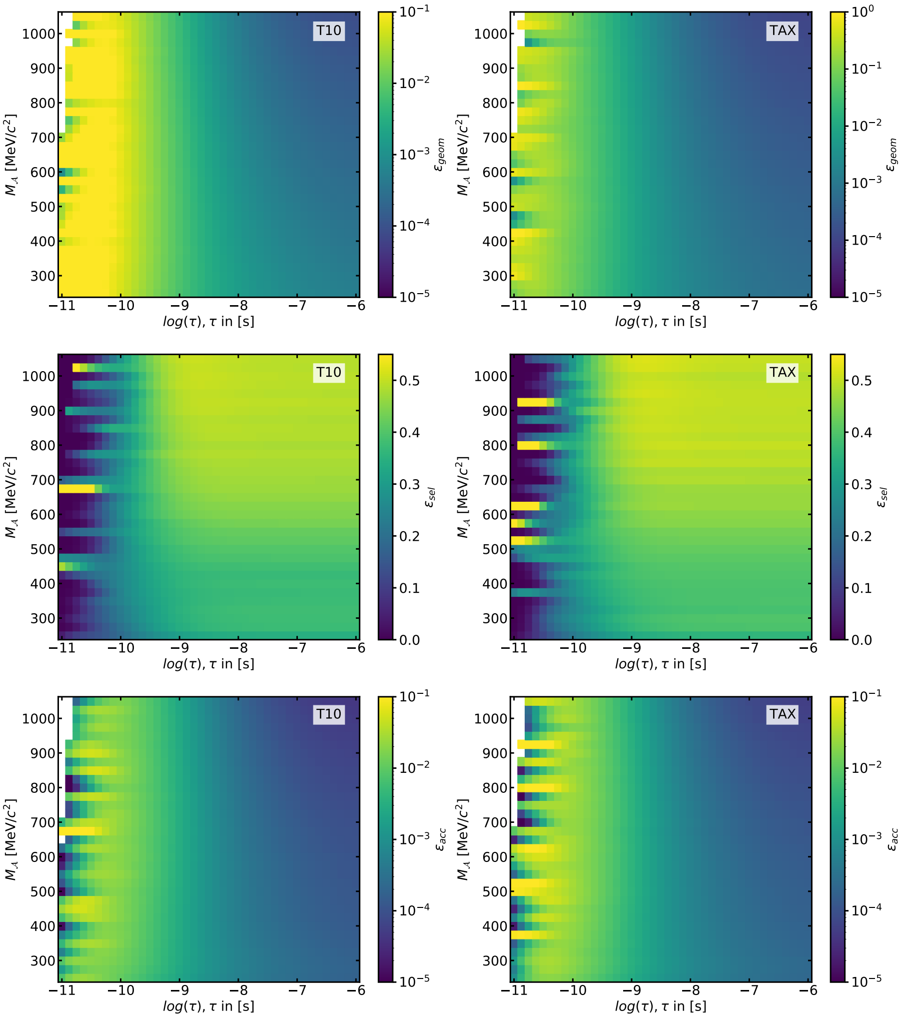

FIGURE 4.8: Left column corresponds to the ALP production in the target T10, right in the TAX. Each plot shows one of the estimated acceptances as a function of the mass and the lifetime. From top to bottom: geometrical acceptance of $B \to K^{(*)}\mathcal{A}, \mathcal{A} \to \mu^+\mu^-$ (ε_{geom}), selection efficiency (ε_{sel}), total acceptance of $B \to K^{(*)}\mathcal{A}, \mathcal{A} \to \mu^+\mu^-$ (ε_{acc}). The oscillations in acceptances in low lifetime values are due to statistical fluctuations.

where $Z^{FVs} = 105$ m and $Z^{FVe} = 180$ m are the start and the end of the NA62 decay volume. The distribution of $P_{rd}(\tau)$ as a function of the mass and the lifetime is displayed in Fig. 4.9. From the plot, one can see that the probability decreases for very short and very large lifetimes. In the first case, particles have a very high probability of decaying before entering the fiducial volume, while in the other, ALPs are more likely to pass the volume without decaying.

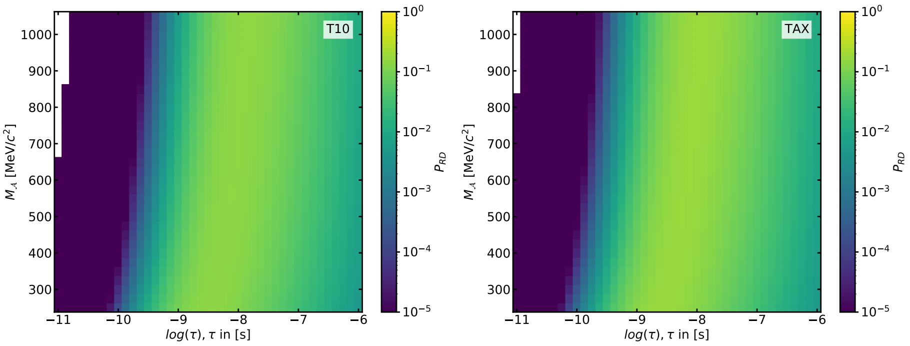

FIGURE 4.9: Probability P_{RD} of the ALP produced in decays of B-mesons to reach the NA62 decay volume and decay therein as a function of the particle mass and lifetime for the target T10 (left) and for the TAX (right).

Before proceeding with further studies, the full MC was validated against the toy-MC described in [94]. For this, the sensitivity of NA62 to ALPs produced in B-meson decays was evaluated using Eq. 4.21, where $POT = 10^{18}$, the production only in the TAX and only the geometrical acceptance was assumed. The sensitivity was evaluated at 95% CL, which corresponds to $N_{exp} = 2.99$.

The comparison between the two estimations made for for an ALP with a mass of 300 MeV/c^2 is shown in Fig. 4.10A. The small discrepancy is due to slightly different acceptance criteria for downstream detectors, in particular LKr and MUV3, used in the toy-MC and in the analysis.

After validating the signal Monte Carlo, the sensitivity of NA62 to ALPs from B-meson decays, including the selection efficiency and production in the TAX and target T10, was evaluated. The result is shown in Fig. 4.10B. As expected, the new bound is weaker than the one accounting only for the geometrical acceptance and the TAX production; however, it still covers a small unexplored parameter space. Additionally, the analysis is still worth doing to cross-check the results obtained with different experimental techniques, particularly results of LHCb and CHARM, where the latter is a recent reinterpretation of the old analysis.

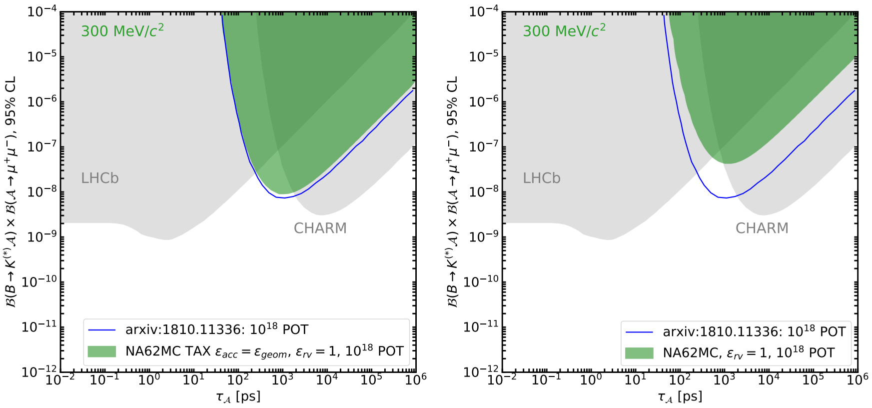

(A) (B)

FIGURE 4.10: (A) Validation of the full Monte Carlo simulation for an ALP with a mass of 300 MeV/c^2. Upper limits on the $B \to K^{(*)}\mathcal{A}, \mathcal{A} \to \mu^+\mu^-$ process are set at 95% CL assuming 10^{18} POT, 0 background events and the geometrical acceptance only. (B) NA62 sensitivity to the $B \to K^{(*)}\mathcal{A}, \mathcal{A} \to \mu^+\mu^-$ process at 95% CL accounting for the production in the TAX and the target T10 and the full efficiency. 10^{18} POT and 0 background events assumed.

It is worth mentioning that the discussed above sensitivity does not include a component of B-mesons produced from secondary products of the hadronic showers occurring in the TAX material; this corresponds to a factor 1.7 of enhancement in the B-meson production [172].

4.7 Resolution studies

The resolution of the reconstructed invariant mass of the two muon tracks is necessary for the mass window definition needed for the background and the final upper limit estimations.

The mass resolution was measured using the signal Monte Carlo, where no additional pileup tracks in the downstream detectors were added except for MUV3. The absence of pileup in the majority of the detectors implies that the resolution shown in this section is likely to be slightly underestimated; the issue will be solved when the signal MC samples with pileup will be available.

The distribution of the difference between the true generated mass of ALP and the reconstructed dimuon invariant mass as a function of the true ALP mass is shown in Fig. 4.11A. For each mass bin, the difference is fitted with a Gaussian function. The dependence of the measured resolution on the mass of the particle is then fitted with a polynomial function. The results are shown in Fig. 4.11B.

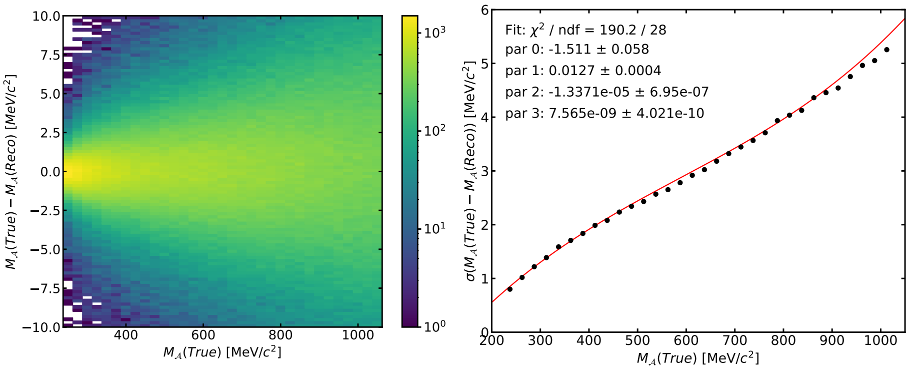

(A)

(B)

FIGURE 4.11: (A) Distribution of the difference between the reconstructed dimuon mass and the value of the true generated ALP mass as a function of the true generated ALP mass. (B) Dimuon invariant mass resolution as a function of the true generated mass of an ALP. This resolution was extracted by performing Gaussian fits in each mass bin of Fig. (A).

4.8 Data analysis

As mentioned in section 4.6, the sensitivity of NA62 to the $B \to K^{(*)}\mathcal{A}, \mathcal{A} \to \mu^+\mu^-$ process depends on the sample size; in this work, it is estimated as a number of protons on target POT. The details of this computation are provided in section 4.8.1.

The effect of accidental activity in veto detectors must be taken into consideration as well. In this work, several veto criteria were applied, and some of them can introduce non-negligible signal rejection due to the accidental hits in time. A so-called random veto efficiency ε_{RV} was estimated to account for this effect; the details of this procedure are given in section 4.8.2. The random veto efficiency enters in the estimation of the number of expected signal events as:

$$N_{exp} = POT \cdot N_{b\bar{b}} \cdot \frac{\sigma_{b\bar{b}}}{\sigma_{pp}} \cdot \sigma(b\bar{b} \to \mathcal{A} \to \mu^+\mu^-) \cdot \varepsilon_{RV} \cdot \\ \cdot \sum_{i=1}^{T10,TAX} (A^i)^{1/3} \cdot f^i \cdot P^i_{RD}(\tau) \cdot \varepsilon^i_{acc} \tag{4.25}$$

Additionally, N_{exp} must include the efficiency of the trigger streams used in this analysis. This efficiency is directly accounted for in the acceptance computation since the analysis requests the response of the trigger emulators. Note that in the plots shown in section 4.6, emulators were not applied. The dedicated study is discussed in detail in section 4.8.3.

Finally, the upper limit on the number of expected events depends on the predicted background. In section 4.6, the zero-background hypothesis was used; however, it can be not the case for this analysis. A preliminary strategy to estimate the background is presented in section 4.9. The estimation was made for each mass window where the search can be performed. The windows were defined using the dimuon mass resolution model extracted in the previous section with the following procedure:

- Start at $m = 2m_\mu$
- Around the selected mass value m define a search window of $\pm 2\sigma$ or $\pm 3\sigma$, where σ is extracted from the mass resolution model using m
- Continue with a step of 1σ.

4.8.1 Estimation of protons on target (POT)

The POT was estimated using two methods. The first method takes readings from the beam counter placed right after the target T10, while the other relies on the number of kaon decays in the NA62 fiducial volume.

The NA62 standard selection, `K3piSelection`,[34] was used to estimate the number of kaon decays. Only events passing the minimum bias CTRL trigger were requested to eliminate any possible bias originating from the physics trigger. The efficiency of the physics trigger used for this analysis is estimated from the dedicated study, and, therefore, is not included in the POT computation.

From the number of $K^+ \to \pi^+\pi^+\pi^-$ ($K3\pi$) decays, $N_{3\pi}$, the total number of kaon decays in the NA62 fiducial volume collected with the trigger masks used in this analysis was computed as:

$$N_K = \frac{D^{CTRL}}{\mathcal{B}(K3\pi) \cdot \epsilon_{acc} \cdot \epsilon_{trigger}} \cdot \sum_{i=1}^{N_{run}} \frac{N_{3\pi}^i}{D_i^{exo}} \tag{4.26}$$

where D^{CTRL} is the downscaling of the CTRL trigger, always 400, D^{exo} is the run-dependent downscaling of the trigger stream used for the analysis (Fig. 4.2A), $\mathcal{B}(K3\pi) = (5.583 \pm 0.024)\%$, ϵ_{acc} is the $K3\pi$ selection acceptance

---

[34] The Doxygen page of the source code: `na62-sw.web.cern.ch/d1/dea/K3piSelection_8cc_source.html`.

(0.1629 ± 0.0001), and $\epsilon_{trigger}$ is the trigger efficiency, which in the case of the CTRL is assumed to be 1.

The total number of protons on target can then be estimated as:

$$POT = \frac{N_K}{P_{decay}} \cdot f_{KtoPOT} \tag{4.27}$$

where P_{decay} is the probability of a kaon to decay inside the NA62 fiducial region given by:

$$P_{decay} = (1 - e^{-\frac{z^{FVs} - z^{FVe}}{\gamma\beta c\tau}}) = 0.124 \tag{4.28}$$

with $\gamma\beta c\tau$ of 75 GeV/c kaon being 563857 mm.

The f_{KtoPOT} factor is taken from Tab. 2.1 to translate the nominal kaon rate to the corresponding nominal proton rate as

$$f_{KtoPOT} = \frac{R_{proton}}{R_{kaon}} = \frac{1.1 \cdot 10^{12}}{45 \cdot 10^{6}} = 24.4 \cdot 10^{3} \tag{4.29}$$

where R_{proton} is the number of SPS protons per burst of 3 s, and R_{kaon} is the rate of kaons in Hz. The error was not reported in [108], and therefore it was assigned with the precision up to the last known digit as $0.1 \cdot 10^{12}/45 \cdot 10^{6} = 2 \cdot 10^{3}$.

The total number of kaon decays in the NA62 fiducial volume collected in 2017-2018 is:

$$N_K = (22.34 \pm 0.26) \times 10^{11} \tag{4.30}$$

where the error comes from the $K3\pi$ branching fraction, selection acceptance and collected statistics. The total POT written in the signal trigger stream is:

$$POT = (4.38 \pm 0.40) \times 10^{17} \tag{4.31}$$

where the error is computed from the error on the number of kaon decays (Eq. 4.30) and the error related to the scaling factor f_{KtoPOT}.

The estimated POT can be correlated with the numbers from the T10 counter. The data from the T10 counter was saved for each burst, and can be accessed using NA62 standard tools. The correlation between the results of both methods for the full data set is shown in Fig. 4.12A. It can be noted, that for certain samples the slope between POT from $K3\pi$ and POT from T10 changes. The evolution of the slope with the run number is shown in Fig. 4.12B, from where it is visible that the change appeared in 2018 (run number ≥ 8518).

Another beam counter, ARGONION, located at the end of the NA62 beamline,

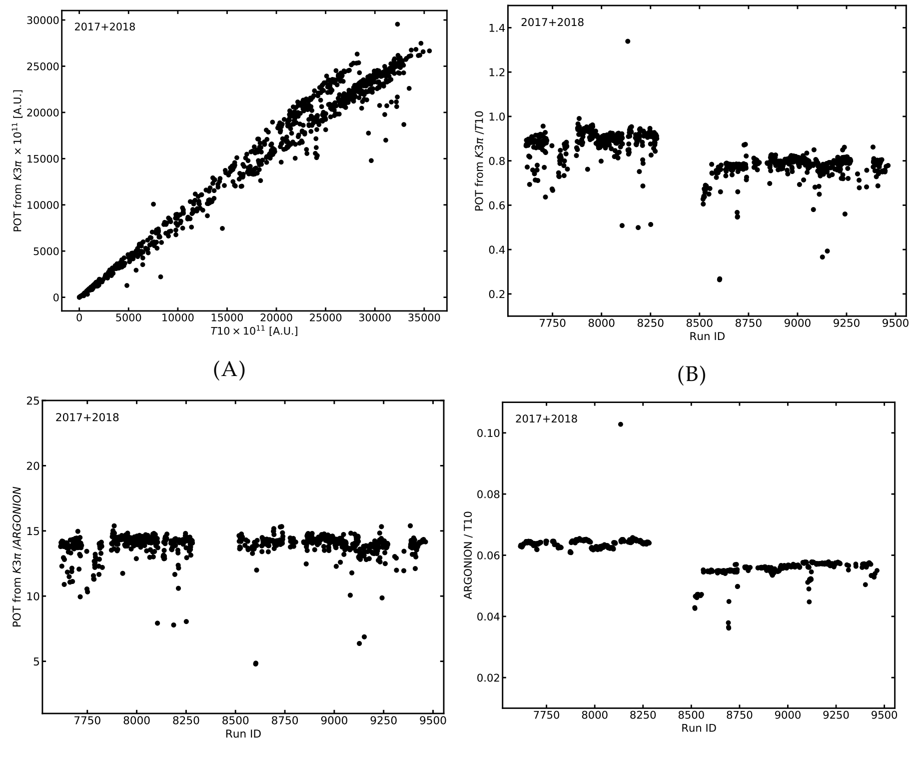

(A) (B)

(C) (D)

FIGURE 4.12: (A) Correlation between the number of protons on target (POT) per run (on average 1500 bursts) computed with the number of $K3\pi$ decays and the number taken from the T10 counter (B) Ratio between POT from $K3\pi$ decays and POT from T10 as a function of run number. (C) Ratio between POT from $K3\pi$ and the numbers taken from the beam counter ARGONION as a function of run number. (D) Ratio between ARGONION counts and T10 counts as a function of run number. Plots (B) and (D) demonstrate a distinct change in the ratio for run numbers > 8500. At the same time, the ratio shown in (C) remains the same for both data taking periods. This behaviour indicates that in 2018 (run number > 8500) a fraction of protons counted at T10 did not interact with its material.

was used to cross-check the results. Ratios between POT from T10 and ARGONION counts and POT from $K3\pi$ and ARGONION counts are shown in Fig. 4.12D and 4.12C. Similar behaviour as in the case of Fig. 4.12B, happens in Fig. 4.12D. This observation indicates that a fraction of protons counted at T10 did not interact with the target material and did not produce particles that could reach the NA62 apparatus. If that is the case, these protons could have interacted with the TAX material instead, providing enhanced probability to create B-mesons interesting for this analysis. The possible explanation for the observed behaviour of proton beam can be in the different beam optic settings used in two separate data taking periods.

The effect of protons missing the target and interacting with the TAX material is hard to quantify, and therefore, the number of POT computed from the $K3\pi$ decays was used in this analysis.

4.8.2 Accidental veto studies

The selection described in section 4.5 employs several veto conditions; in particular, events with signals in LAV, SAV, LKr and CHANTI detectors are rejected. These criteria, however, can introduce some accidental signal rejection due to pileup activity in the corresponding detectors. Consequently, it is essential to minimise these losses as much as possible.

The $K\mu2$ selection was used to measure the effect of the random activity. The $K\mu2$ decay has a large branching fraction of $\mathcal{B} = (63.56 \pm 0.11)\%$ and a single muon track in the final state. Therefore, selecting this decay inside the NA62 fiducial volume can ensure the absence of decay-related signals in the detectors of interest. The $K\mu2$ selection is described below.

$K\mu2$ selection

The selection proceeds as follows:

- CTRL trigger events only;
- only one good track per event with
  - track charge is $+1$;
  - track is not marked as fake;
  - track fit χ^2 is less than 40 (20 in the signal selection);
  - hits in at least 3 STRAW chambers;
  - track momentum is between 10 and 70 GeV/c (no upper cut on the momentum in the signal selection);
  - track is in geometrical acceptance of all STRAW chambers, NA48 CHOD, LKr and MUV3;
- there is a good KTAG candidate with the number of fired sectors higher than 4, and within 3 ns with NA48 CHOD candidate associated with the track (rejected in the signal selection);

- beam-track CDA is less than 20 mm (rejected in the signal selection);
- Z position of beam-track CDA is between 110 and 180 m (not applied in the signal selection);
- the track has an association with a MUV3 candidate from outer tiles in 3 ns with the track time provided by NA48 CHOD;
- no association with clusters in LKr or, if there is, the energy over momentum ratio should be below 0.2, and only one cluster is associated with the distance from the closest dead cell larger than 20 mm;
- m^2_{miss} is between ± 0.015 GeV$^2/c^4$, where $m^2_{miss} = (P_K - P_\mu)^2$, P_K is the nominal beam 4-momentum assuming it is a kaon, and P_μ is the track 4-momentum assuming it is a muon (rejected in the signal selection).

The selection efficiency is measured on MC and is $\epsilon_{K\mu 2} = 0.47447 \pm 0.00003$. The contribution from $K^+ \to \pi^+\pi^0$ and $K\mu3$ decays, also measured with MC, is 4×10^{-4} and 3.5×10^{-6} respectively.

Random veto efficiency

For the selected $K\mu2$ events, the same veto conditions as in the signal selection (section 4.5) were applied. The value of ε_{RV} was computed for each veto criteria independently as follows:

$$\varepsilon^i_{RV} = \frac{N_{pass\ veto\ i}}{N_{K\mu 2\ tot}} \tag{4.32}$$

The distributions of ε^i_{RV} as a function of run number are shown in Fig. 4.13A. The value of the random veto for each of the conditions was stable within 2% during the full data taking except for several runs in 2018 collected with different beam conditions (higher intensity in particular). The slight decrease in efficiency happens due to the dependence of the random veto efficiency on the beam intensity (Fig. 4.13B). From Fig. 4.13A and 4.13B, it can be noted that the highest random veto efficiency is in CHANTI, while the lowest efficiency comes from LKr and LAV.

The LKr veto conditions were previously optimised for the $K^+ \to \pi^+\nu\bar{\nu}$ analysis [171]; in this work, the same strategy was adopted. As for the LAV, based on previous similar studies, various settings of the cuts were investigated (Fig. 4.13C):

- at least one hit in any of LAV sub-detectors;
- at least two hits in any of LAV sub-detectors;
- at least one hit with Z position further than the vertex Z position;

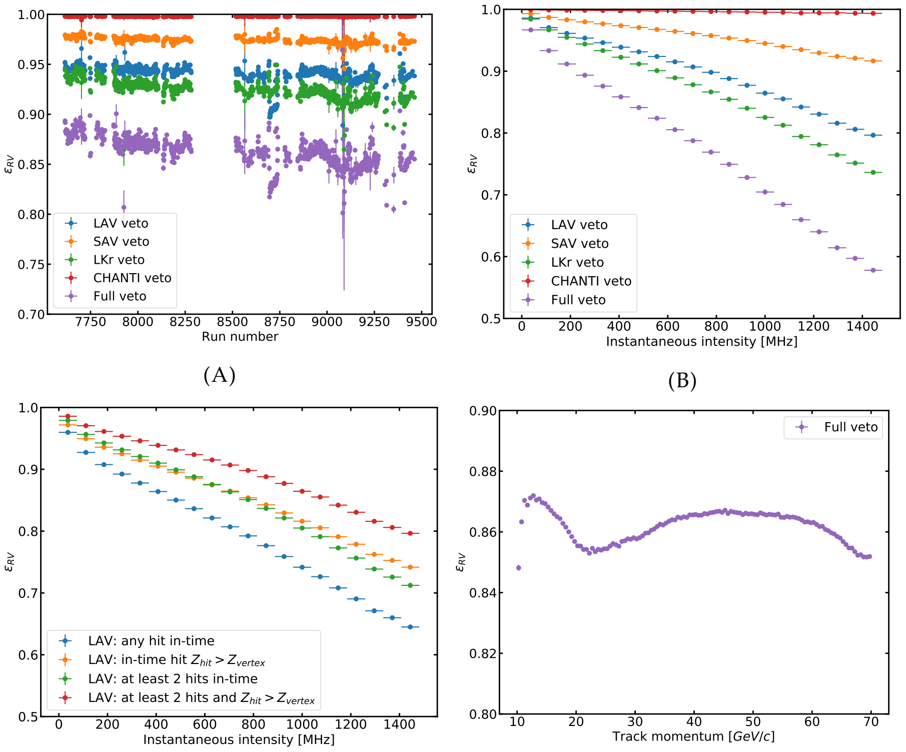

(A) (B)

(C) (D)

FIGURE 4.13: (A) Random veto efficiency for each veto condition independently as a function of the run number in 2017-2018. The "Full veto" here and further stands for the total random veto efficiency estimated with all conditions applied simultaneously. (B) Random veto efficiency for each veto condition independently as a function of the instantaneous beam rate. (C) Random veto efficiency studies for the LAV condition displayed as a function of the instantaneous beam rate. (D) Random veto efficiency as a function of the muon track momentum for the full data sample.

- at least two hits in the LAV sub-detector with Z position further than the vertex Z position.

The best combination of cuts was chosen as at least two hits with Z position further than Z position of the vertex. However, this condition can increase the contribution from $K3\pi$ decays where one of the pions travels in the opposite direction from the kaon decay position.

The final value of random veto efficiency is:

$$\varepsilon_{RV} = 0.862 \pm 0.014_{mom} \pm 0.020_{mc} \tag{4.33}$$

where *mom* error is taken from the muon track momentum dependence of the measured random veto (Fig. 4.13D), and computed as a maximum deviation from the mean value; *mc* comes from the comparison between the random veto calculated on $K\mu2$ Monte Carlo (no pileup tracks added) and the random veto measured on data and propagated to 0 intensity. The statistical error was found to be negligible. The momentum dependence mentioned previously may come from the radiative process, secondary muon interactions, or muon interactions in the last station of LAV.

4.8.3 Trigger efficiency

The signal Monte Carlo with emulators for L0 and HLT for L1 was used to estimate the efficiency of the triggers used in the analysis. Unfortunately, the signal MC was reconstructed without pileup tracks added in the downstream detectors (except for MUV3); therefore, the estimation of the triggers provided in this section is not complete. In the future, it is considered to use the overlay reconstruction technique to improve the study. However, at the time of writing this manuscript, this sample was not available for technical reasons.

Trigger efficiency using signal MC

The efficiency for each of the L0 and L1 conditions is defined as

$$\varepsilon^{i}_{trigg} = \frac{N_{pass\ trigger\ i}}{N_{sel}} \tag{4.34}$$

where N_{sel} is the number of events passing the signal selection, and $N_{pass\ trigger\ i}$ is the number of events passing the selection and the trigger.

Fig. 4.14 displays the efficiency of each L0 trigger condition as a function of the generated mass. The errors are shown as well; however, most of them are covered by markers. It can be noted that QX and Q2 have the lowest efficiency – all below 90%, with QX being less than 20% for masses below 700 MeV/c^2. The reason for such performance is the following. The kinematics of the signal event is such that the lower the mass is, the more boosted muons become in the direction of the ALP. Hence the separation between the two tracks at the CHOD plane decreases, directly affecting the probability to create QX or Q2. This behaviour can be seen from the dependence of QX and Q2 efficiency on the mass of the particle; moreover, it was already hinted from the selection efficiency (see section 4.6). It is worth mentioning that the Q2 condition was also used in the beam dump mode of the NA62 data taking, meaning that the same loss appears there as well. However, in this mode, no trigger downscaling factor was applied.

The efficiency for L1 STRAW conditions as a function of mass is shown in Fig. 4.15A. In the case of L1 STRAW, the opposite situation to QX and Q2 was observed: here, the efficiency increases with the ALP mass. This happens due to the momentum and angular conditions applied in the trigger algorithm. Indeed, as discussed before, the transverse momentum of muons increases with the mass of the ALP. The same is true for the longitudinal momentum component. Therefore, the combination of these two effects increases the probability to be rejected by the L1 STRAW algorithm. The rejection is even stronger in the STRAWDV5 algorithm since the momentum cut was applied on both tracks. Fig. 4.15B shows the L1 STRAW efficiency as a function of the muon momenta to illustrate the effect of the L1 algorithms on the signal events.

It is possible that the efficiency of QX and Q2 conditions can be slightly improved if the random activity is considered. For example, if both tracks are present in one of the CHOD quadrants, random in time hit in one of the other quadrants can allow the event to pass QX or Q2 condition. Consequently, the random triggering of QX and Q2 can be estimated from data using the $K\mu2$ decays. For this study, the same $K\mu2$ selection as in the previous section was used. The probability of the $K\mu2$ event passing the QX and Q2 triggers as a function of the run number is shown in Fig. 4.16. These values were roughly stable during the whole data taking period except for a few runs at the beginning of 2017 (2017D sample). For QX and Q2, the mean probability of producing accidental trigger P^{i}_{rand} was found to be 0.025 and 0.068, respectively. Knowing P^{i}_{rand} and the values of ε^{i}_{trigg} without pileup, the efficiency of QX for each mass given the presence of a single hit in any of the CHOD quadrants was estimated as:

$$\varepsilon^{QX}_{trigg+rand} = \varepsilon^{!Q2}_{trigg} \cdot P^{QX}_{rand} + 2 \cdot (\varepsilon^{!(QX\ or\ !Q2)}_{trigg}) \cdot P^{QX}_{rand} + \varepsilon^{QX}_{trigg} \tag{4.35}$$

where $\varepsilon^{!(QX\ or\ !Q2)}_{trigg}$ is the probability to have hits in the neighbouring non-diagonal quadrants computed as $1 - \varepsilon^{QX}_{trigg} - (1 - \varepsilon^{Q2}_{trigg})$, the factor of 2 is added to account for an increased chance to have QX given Q2. The $\varepsilon^{!Q2}_{trigg}$ is $1 - \varepsilon^{Q2}_{trigg}$. The efficiency of Q2 was computed as:

$$\varepsilon^{Q2}_{trigg+rand} = \varepsilon^{!Q2}_{trigg} \cdot P^{Q2}_{rand} + \varepsilon^{Q2}_{trigg} \tag{4.36}$$

To account for the new QX and Q2 trigger efficiencies, the expected number of events for each sample, i.e. samples with QX or Q2 in the trigger mask, was multiplied by a corresponding number computed as the ratio between $\varepsilon^{i}_{trigg+rand}$ and ε^{i}_{trigg}.

Since the estimations made in Eq. 4.35 and Eq. 4.36 assumed the probability of having a hit in any of the CHOD quadrants equally likely, a systematic error of 10% was assigned to the estimated efficiencies to account for the non-uniform distribution of random activity in the CHOD. The error was obtained from the following consideration. If particles were indeed uniformly distributed at the CHOD plane, the Q2 condition would be three times more likely to appear than QX. Therefore, the error of the estimated random activity can be taken from the following expression: $3 \cdot P^{QX}_{rand} / P^{Q2}_{rand} - 1$. Inserting the numbers for the probabilities of the QX and Q2 random firing quoted above, one would get $3 \cdot 0.025/0.068 - 1 = 0.10$.

The trigger efficiency evaluation presented in this section can be improved by using Monte Carlo with the properly simulated pileup activity. Therefore, in future studies, the Monte Carlo reconstructed with the overlay technique should be used.

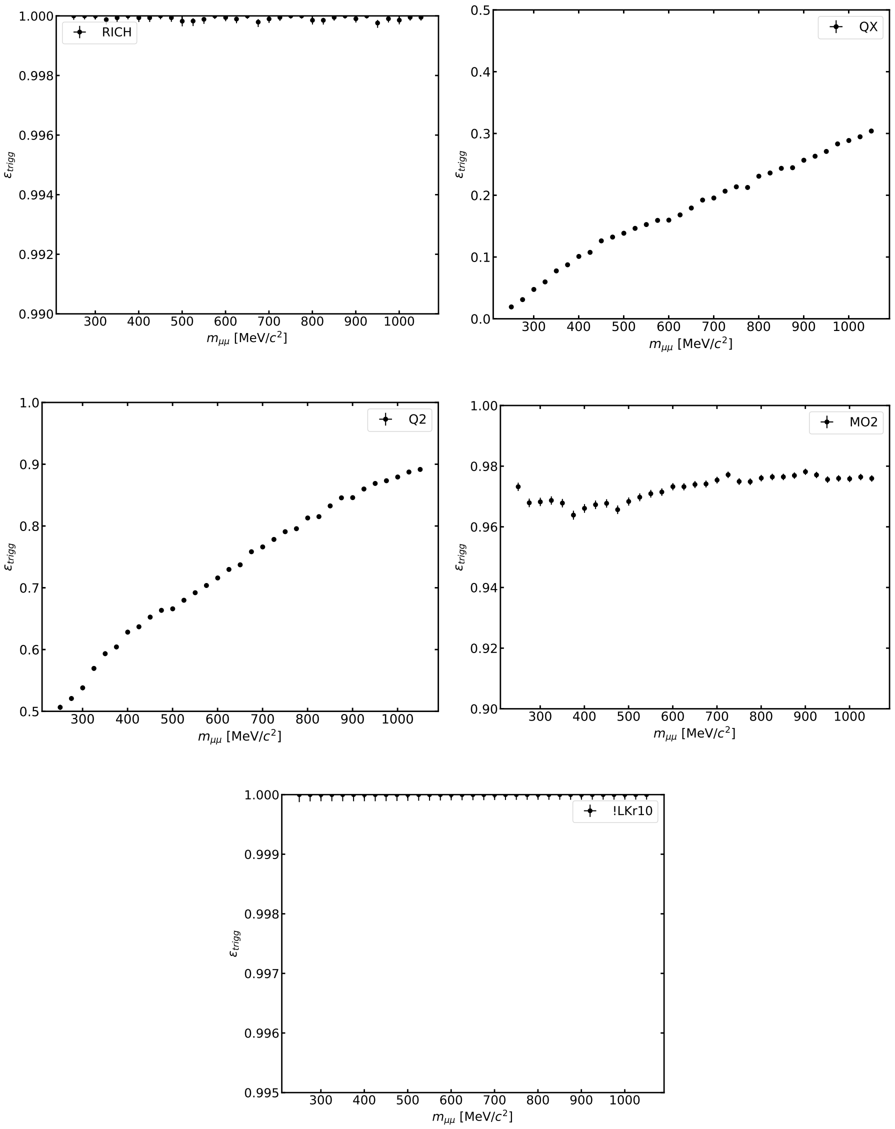

FIGURE 4.14: L0 trigger efficiencies as a function of the mass of the generated particle measured on the signal Monte Carlo. No pileup tracks were added (except for MUV3), and no lifetime-related weight was applied. The efficiencies were defined as a fraction of events passing the trigger condition and the signal selection from all events passing the signal selection.

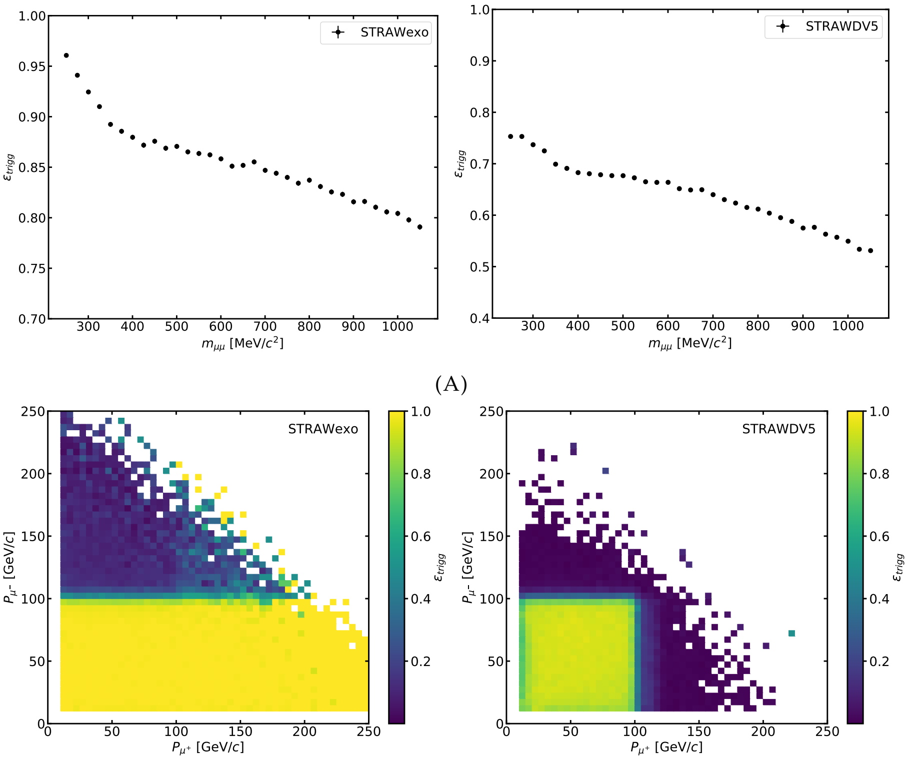

(A)

(B)

FIGURE 4.15: L1 trigger efficiencies measured on the signal Monte Carlo as a function of the mass of the generated particle (A) and the muon track momenta (B). No pileup tracks were added, and no lifetime-related weight was applied. Similarly to L0, the efficiencies were defined as a fraction of events passing the L1 algorithm and the signal selection from all events passing the signal selection.

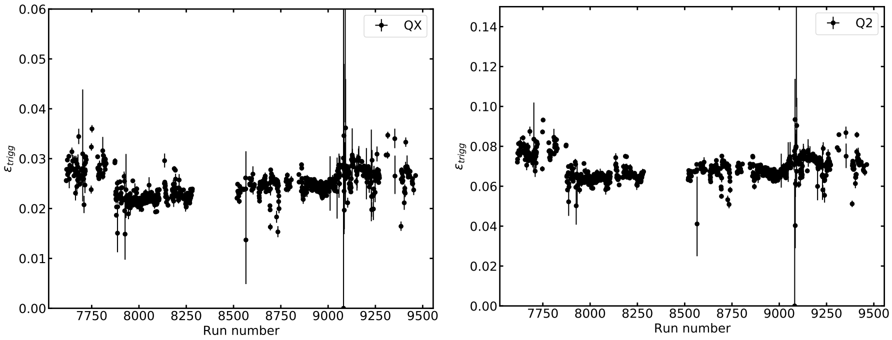

FIGURE 4.16: Probability of the $K\mu 2$ event to pass QX or Q2 condition as a function of the run number. This probability was estimated as a ratio between the selected $K\mu 2$ events passing the QX or Q2 condition and the total number of the $K\mu 2$ events. Since $K\mu 2$ has a single track in the final state, these probabilities are linked to the pileup effects in the L0 CHOD.

Preliminary sensitivity evaluation

Fig. 4.17 demonstrates the sensitivity of NA62 to the $B \to K^{(*)}\mathcal{A}, \mathcal{A} \to \mu^+\mu^-$ process considering the evaluated POT, ε_{RV}, ε_{trigg} and 0 background events; the trigger efficiency was applied using the emulators and HLT on the signal MC. In addition, the estimated effect of random triggering for QX and Q2 is included as scaling factors defined in the previous section. The evaluated NA62 sensitivity is now lying well inside the parameter region excluded by LHCb. The inclusion of the pileup activity helps to improve the situation slightly. It is possible that considering the B-meson production in the secondary products of the hadronic showers in the TAX will improve the sensitivity even further.

This study shows that the inefficient trigger conditions and the downscaling factors dramatically reduced the sensitivity of NA62 in the most interesting mass range below 600 MeV$/c^2$. However, in the data taking starting in July 2021, NA62 is going to collect data at 100% of nominal intensity. Therefore, the analysis can benefit from the newly collected sample if the trigger conditions are reviewed.

Possible improvements for the future data taking

Several possible changes that could be addressed in the conditions of the dimuon trigger were studied. Their description is provided below:

- H2 – at least two in time hits in CHOD. Very sensitive to random activity since it accepts events with two hits in the same tile

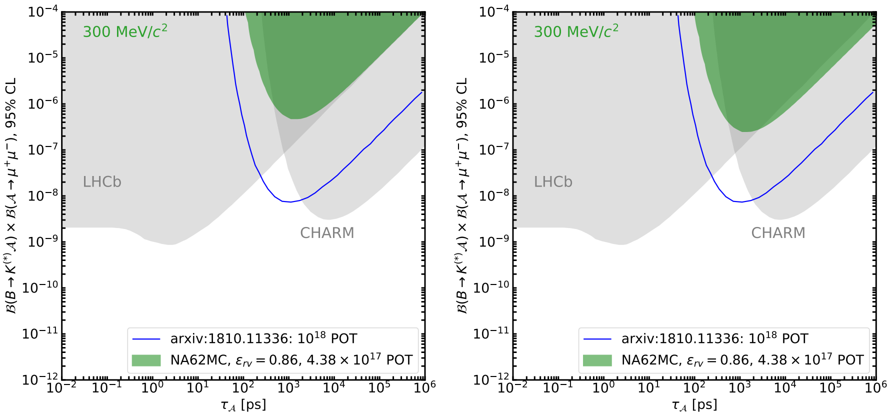

(A) (B)

FIGURE 4.17: Sensitivity of NA62 to the $B \to K^{(*)}\mathcal{A}, \mathcal{A} \to \mu^+\mu^-$ process at 95% CL accounting for the geometrical acceptance, the selection and the trigger efficiency, POT and the zero-background hypothesis without considering pileup in QX and Q2 (A) and with (B).

- HO2 – same as H2, but excluding tiles around the beam pipe
- !H3 – number of in time hits in CHOD is less than 3
- RICH6 – at least six hits in RICH
- RICH8 – at least eight hits in RICH
- RICH10 – at least ten hits in RICH

The efficiency of each each tested condition as a function of ALP mass is shown in Fig. 4.18; for the study, the trigger emulators with no pileup included were used.

From all CHOD-based conditions, H2 gives the highest efficiency of $\sim$ 100%. However, it is very sensitive to the random activity in the detector, meaning the trigger rate is expected to be very high. A good alternative can be HO2, which provides trigger efficiency higher than 87% for the full studied mass range. The data rate of this condition is expected to be lower since the tiles with the highest activity (closest to the beamline) are excluded. To further reduce the trigger rate, RICH10 or RICH8 can be used instead of the standard RICH. These conditions have an efficiency higher than 90% for all studied masses. An observed decrease of efficiency with the mass of the particle can be explained by increasing separation between two tracks, which, in this case, leads to higher chances to slightly miss the acceptance of RICH by one of the tracks.

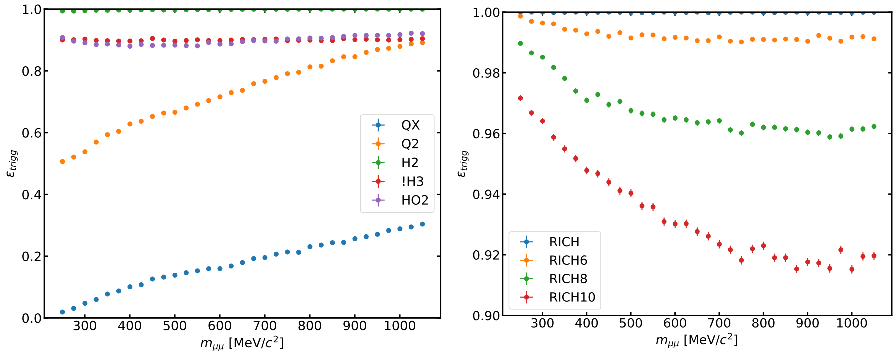

FIGURE 4.18: Efficiencies of the proposed L0 trigger conditions as a function of the ALP mass measured on the signal Monte Carlo. No pileup tracks were added, and no lifetime-related weight was applied. The HO2 CHOD condition seems to be the best candidate to replace Q2 and QX. The trigger rate can be further adjusted using one of the RICH conditions shown on the right plot.

The data rates of the proposed trigger conditions are under investigation. However, the final decision on whether to implement them will be made after performing a test on data during the first weeks of the stable data taking in the coming run in 2021.

The trigger stream used in this analysis can benefit from another detector, which was not studied or discussed in this thesis. The ANTI0 counter is a new detector to be installed for the data taking in 2021. The detector will have dimensions of 1080 × 1080 mm and will be placed after the last CHANTI station. In this analysis, ANTI0 can be used as a veto detector against halo muons. Additionally, it can be included in the trigger, which can help to reduce the dimuon mask's total rate. The impact of ANTI0 on the trigger rate will also be investigated during the data taking in 2021.

Finally, the work on the L1 STRAW algorithm is ongoing. It is possible that an efficiency of $\sim 80\%$ can be achieved; however, the expected trigger rate after this improvement is under investigation [173].

4.9 Background estimation

Even though NA62 appeared to be not sensitive to the $B \to K^{(*)}\mathcal{A}, \mathcal{A} \to \mu^+\mu^-$ process, the analysis itself is model-independent. Therefore, it is still important to estimate the expected background. Since the results of this analysis are preliminary and can be interpreted in terms of a different model, the signal region for $\mu^+\mu^-$ events kept blinded.

As mentioned in section 4.3, two background components were considered: prompt and combinatorial. Prompt background can consist of kaon decays, decays of other mesons, and possible photon conversion into muons. Combinatorial, in turn, is a random combination of muons from prompt processes and muon halo. The strategy to evaluate both background components will be described in the following subsections. The preliminary results of the study will be presented as well. Considering the sensitivity of NA62 to the signal discussed in previous sections, no signal event is expected to be observed after applying the selections described below.

4.9.1 Combinatorial background

For estimation of the combinatorial background component, vertices with oppositely charged muons out of time with each other were used. In this case, it is assumed that such events are evenly distributed in time; hence, they can be present in the signal region.

In the signal selection (section 4.5), the events with tracks in ±3 ns with respect to each other are selected. Therefore, to estimate the combinatorial background inside this time window, one must use an equivalent side-band. However, due to the bias introduced by the trigger time window definition, ±6.25 ns, and the other timing cuts applied in the analysis, the side-bands $(-6,-3) \cup (3,6)$ cannot be used. Instead, events in the range $(-5,-3) \cup (3,5)$ were selected. The distribution of the time difference between two muon tracks in the vertex is shown in Fig. 4.19A; the full selection is applied except for the timing cuts, events inside the signal region not included. The selected side-bands are indicated with green arrows.

The total time window of the NA48 CHOD side-band used in this analysis is 4 ns, while the time window in the signal selection is 6 ns. Therefore, a scaling factor of 1.5 must be applied to the number of background events found inside the signal region of the side-band. The expected number of events inside the blinded region can then be computed as:

$$N^{\mu^+\mu^-}_{comb} = N^{\mu^+\mu^-}_{chsb\ sig} \cdot 1.5 \tag{4.37}$$

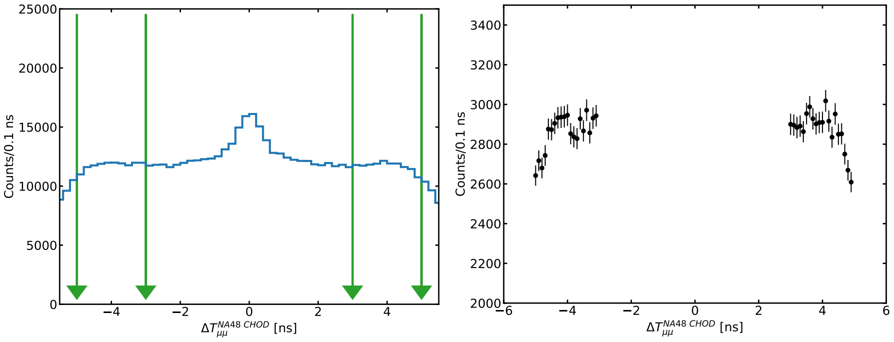

(A) (B)

FIGURE 4.19: (A) Distribution of the time difference between the two muon tracks, where time is taken from the NA48 CHOD. The green arrows indicate the boundaries of the selected side-bands. (B) Distribution of events inside the NA48 CHOD time side-bands after applying the full selection except for the signal box. It can be noted that the distributions are not uniform as one would expect; this is due to the timing conditions applied earlier in the trigger and the selection.

where $N^{\mu^+\mu^-}_{chsb\ sig}$ is the number of events found inside the signal region of the NA48 CHOD side-bands.

To extract the shape of the combinatorial background in the signal region, all selection criteria but the signal box were applied. However, the obtained dimuon mass distribution could not be used due to an observed correlation between the minimum distance to the IP and the dimuon mass (Fig. 4.20). Therefore, the range of minimum distance to IP from 20 to 200 mm was selected (marked with the red box in Fig. 4.20). The shape of the dimuon mass distribution in this range was found to be compatible with the one inside the signal region with a probability of 0.3 computed from the Kolmogorov test. The integral of the obtained distribution was then set to the $N^{\mu^+\mu^-}_{comb}$.

The expected combinatorial background in bins of 2 MeV/c^2 and for each mass window is shown in Fig. 4.21. The systematic error of 10% was assigned to account for the non-uniform distribution of events in the NA48 CHOD time side-bands (Fig. 4.19B); the error was subtracted from polynomial fits to the distribution shown in Fig. 4.19B in the different time ranges.

The observed combinatorial background was found to be a random combination between muons from decays upstream the NA62 decay region, pion decays in particular, muons from $K\mu2$ decays, muons from $K^+ \to \pi^+\pi^+\pi^-$ decays with subsequent pion decay, and muons from the beam halo.

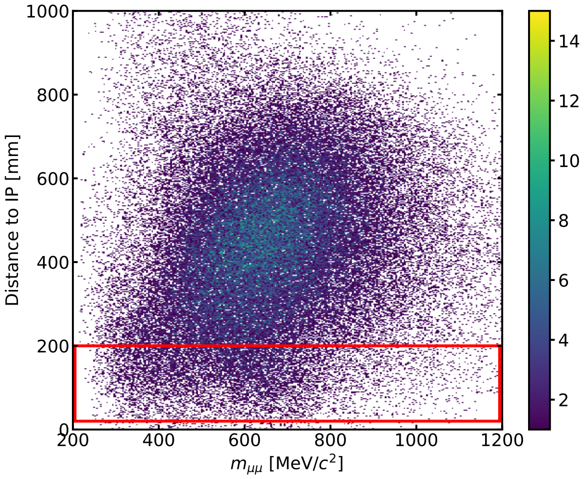

FIGURE 4.20: Minimum distance to the interaction point (IP) as a function of the dimuon mass for events in the NA48 CHOD side-bands. The region used to extract the shape of the combinatorial background inside the signal region is shown with the red rectangle.

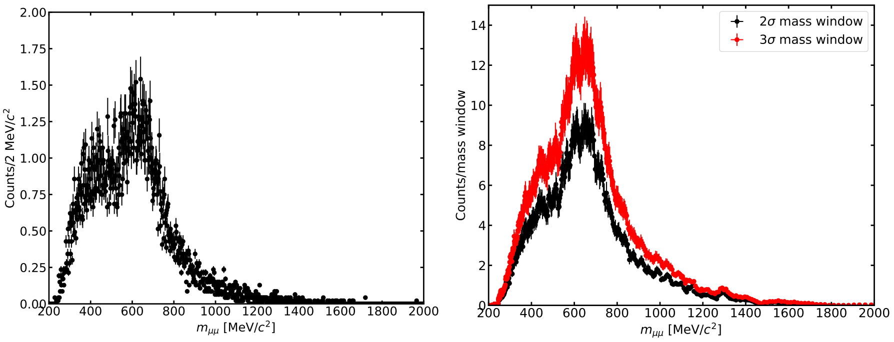

(A)

(B)

FIGURE 4.21: Expected number of combinatorial events in the blinded region as a function of the invariant dimuon mass in 2 MeV/c^2 bins (A) and for each mass window (B). The 10% systematic error was assigned to account for the non-uniform time distribution in the NA48 CHOD side-bands.

4.9.2 Prompt background

In the prompt background study, vertices with tracks of the same charge were investigated. For this, the full selection except for the signal region cut was applied, the vertex charge was requested to be either $+2$ or -2.

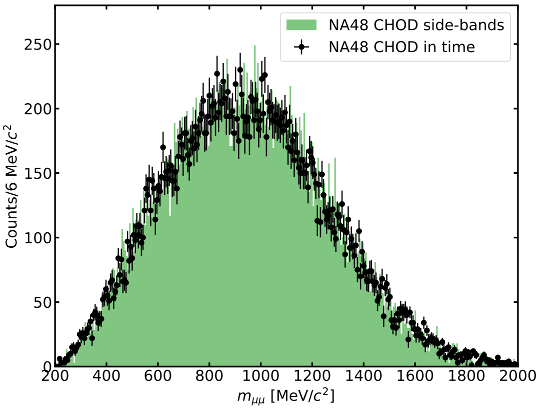

FIGURE 4.22: Dimuon mass distribution for $\mu^-\mu^-$ events in the NA48 CHOD side-bands compared to the same distribution for the in time tracks.

The $\mu^-\mu^-$ dimuon mass distributions in the NA48 CHOD side-bands (combinatorial) and for the in time tracks are shown in Fig. 4.22. The combinatorial side-bands are defined as in the previous subsection, excluding the upper cut on the minimum distance to the IP. The in time side-bands are defined using the timing cut as in the signal selection and the cut on the minimal distance to the IP as $\text{IP} > 20$ mm. As shown in Fig. 4.22, the in time $\mu^-\mu^-$ sample is dominated by the combinatorial background. The in time and side-band distributions were found to be alike, with the probability obtained from the Kolmogorov test equal to 0.76. This observation is expected since the NA62 beam consists of positively charged particles, where negative muons typically originate from kaon decays into three charged particles, most of which are $K^+ \to \pi^+\pi^+\pi^-$. Hence, the probability of having two negative muons coming from the same process is expected to be very small.

For the sample with $\mu^+\mu^+$, the situation is different. From the comparison between the dimuon distribution in the combinatorial and in time samples, a peak of in time events in the low dimuon mass can be clearly seen (Fig. 4.23). The side-bands were defined as in the case of $\mu^-\mu^-$. The events in the combinatorial sample were found to be dominated by $K\mu2$ decays combined with the halo muons. As concluded from the Monte Carlo, the in time events mostly come from the $K^+ \to \pi^+\pi^+\pi^-$ decay with one or two pions decaying in flight. Indeed, the pion decay in flight is a necessary ingredient for this background since vertices reconstructed with the two tracks from a kaon decay will have a small displacement (below 50 mm) from the nominal beamline. If one of the pions decays either before or inside the first STRAW chambers, the direction of the reconstructed track will be slightly different, increasing the probability for the two-track vertex to pass the cut on the minimum distance to

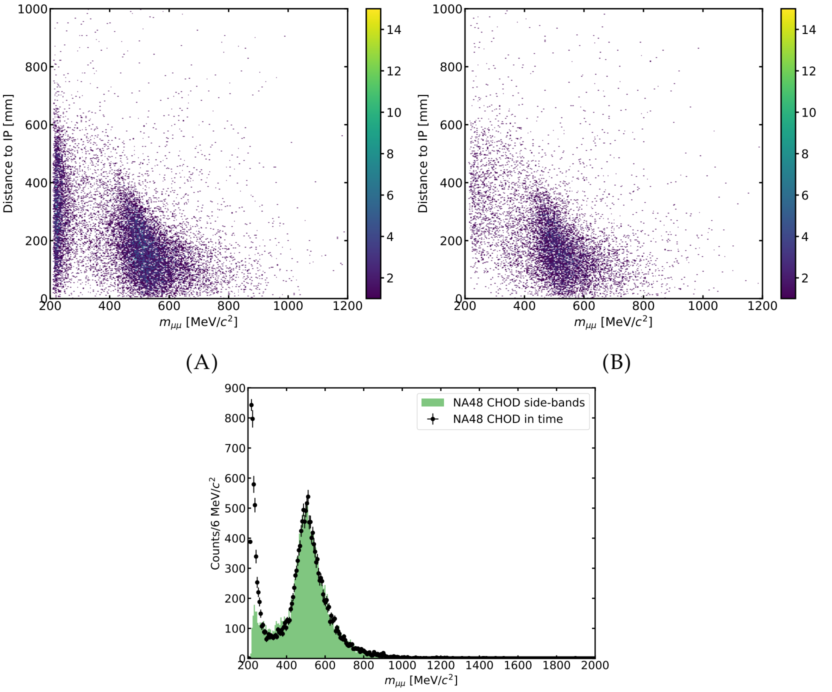

(A)

(B)

(C)

FIGURE 4.23: Minimum distance to the interaction point (IP) as a function of the dimuon mass for $\mu^+\mu^+$ events in time (A) and in the NA48 CHOD side-bands (B). (C) Comparison between the dimuon mass distribution for the in time $\mu^+\mu^+$ events and events in the NA48 CHOD side-bands. The contribution of the K3pi decays can be seen in the dimuon mass close to the kinematic threshold.

the beamline.

The contribution of the in time component can be obtained by subtracting the combinatorial component from the in time distribution. The procedure was done as follows. First, the maximum likelihood fit was performed on the dimuon distribution in the NA48 CHOD side-bands with a model parametrised as the sum of two Landau and one Gaussian probability density functions (PDF) (Fig. 4.24A) as:

$$F_{chsb}^{\mu^+\mu^+} = f \cdot G_{fit}(x|\mu, \sigma) + (1-f) \cdot L_1(x|\mu_{L1}, \sigma_{L1}) + (1-f) \cdot f' \cdot L_2(x|\mu_{L2}, \sigma_{L2}) \tag{4.38}$$

The L_2 here is the Landau with the smallest most probable value μ. Then, the in time dimuon distribution was fitted with the sum of the $F_{chsb}^{\mu^+\mu^+}$ model and a

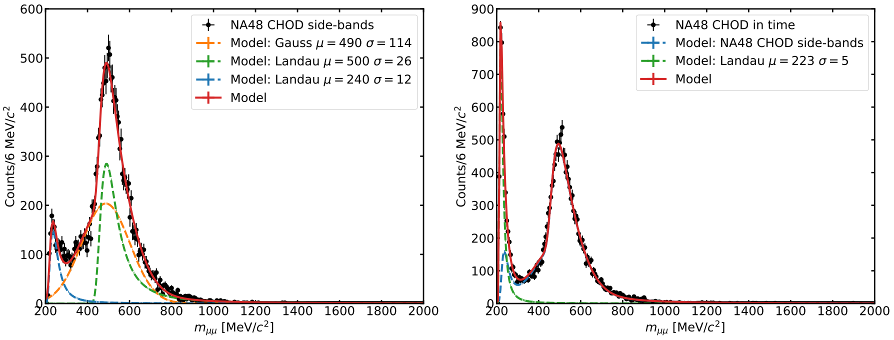

(A) (B)

FIGURE 4.24: (A) Fit of the $\mu^+\mu^+$ dimuon mass distribution in the NA48 CHOD time side-bands with the model comprised of two Landau and one Gaussian PDFs. (B) Fit of the $\mu^+\mu^+$ dimuon mass distribution for the in time events with the model comprised of a Landau PDF and the NA48 CHOD side-band model. This Landau PDF is used to estimate the expected number of in time events.

Landau PDF as shown in Fig. 4.24B. For the fit, the `RooFit` package [174] was used. The fit parameters f and f' from the combinatorial model were fixed. The shape of the in time background was parametrised by the last Landau PDF, which fit parameters were stored.

Then, the obtained Landau distribution was scaled to the number of events in the signal region. To estimate the scaling factor, the in time $\mu^+\mu^+$ events with $m_{\mu^+\mu^+} < 300$ MeV/c^2 were selected. This mass range was chosen based on Fig. 4.23C, from which it can be assumed that in this mass region, the background is dominated by the in time component. The expected number is then can be computed as:

$$N_{sig}^{\mu^+\mu^+} = N_{fit}^{\mu^+\mu^+} \cdot \frac{N_{IP<20}^{\mu^+\mu^+}}{N^{\mu^+\mu^+}} \tag{4.39}$$

where $N_{IP<20}^{\mu^+\mu^+}$ is the number of events with the dimuon mass below 300 MeV/c^2 and with the minimum distance to the interaction point below 20 mm, $N^{\mu^+\mu^+}$ is the total number of events with the dimuon mass below 300 MeV/c^2, and $N_{fit}^{\mu^+\mu^+}$ is the integral of the obtained Landau distribution. The combinatorial component, possibly contributing to $N_{IP<20}^{\mu^+\mu^+}$ and $N^{\mu^+\mu^+}$, was removed using the events found in the NA48 CHOD side-bands in the same dimuon mass and the minimum distance to the IP regions. The value of the $N_{IP<20}^{\mu^+\mu^+}/N^{\mu^+\mu^+}$ was found to be 0.003 ± 0.001. This computation assumes that the shape of the dimuon distribution of the in time events does not depend on the minimum

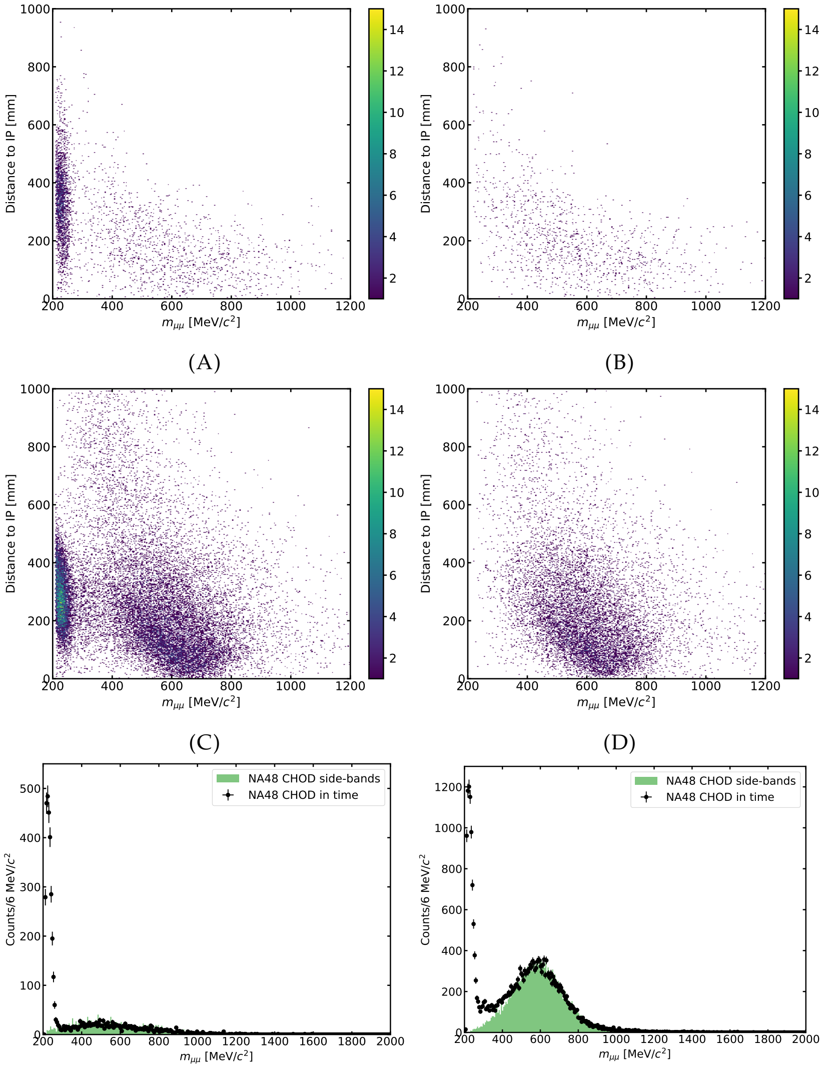

(A) (B)

(C) (D)

(E) (F)

FIGURE 4.25: Top two rows: minimum distance to the interaction point (IP) as a function of the dimuon mass for events inside the vertex Z position side-bands for $\mu^+\mu^+$ (top) and $\mu^+\mu^-$ (middle) vertices: (A), (C) in time events; (B), (D) events in the NA48 CHOD side-bands. Bottom row: comparison between the dimuon mass distribution of the in time events and the events in the NA48 CHOD side-bands for $\mu^+\mu^+$ (E) and $\mu^+\mu^-$ (F) vertices inside the vertex Z position side-bands.

distance to the interaction point, which is a valid assumption as it can be seen from Fig. 4.23A.

The conversion from $N_{sig}^{\mu^+\mu^+}$ to $N_{sig}^{\mu^+\mu^-}$ was performed using the $\mu^+\mu^+$ and $\mu^+\mu^-$ events in the side-band of the two-track vertex Z position. The side-band was defined by alternating the corresponding cut in the full selection to 90 m $< Z_{vertex} <$ 110 m. Fig. 4.25 shows the in time and the combinatorial samples of the vertex Z position side-band for $\mu^+\mu^+$ and $\mu^+\mu^-$ events. In this case, the in time component is also concentrated in the low mass region and has a similar shape as for the $\mu^+\mu^+$ events studied above. The ratio between the in time $\mu^+\mu^+$ and $\mu^+\mu^-$ is defined as:

$$f_{\mu^+\mu^+ \ to \ \mu^+\mu^-} = \frac{N_Z^{\mu^+\mu^-} - N_{Z\ comb}^{\mu^+\mu^-}}{N_Z^{\mu^+\mu^+} - N_{Z\ comb}^{\mu^+\mu^+}} \tag{4.40}$$

where N_Z is the number of events inside the vertex Z position side-band with muon tracks in time and the dimuon mass below 300 MeV/c^2, while $N_{Z\ comb}$ is the number of the combinatorial events inside the vertex Z position side-band with the dimuon mass below 300 MeV/c^2. The value for the ratio was found to be $f_{\mu^+\mu^+ \ to \ \mu^+\mu^-} = 2.94 \pm 0.12$. It is higher than 2 as one could expect from $K^+ \to \pi^+\pi^+\pi^-$ hypothesis due to the L1 trigger conditions selecting events with at least one negative track.

Finally, the number of expected prompt $\mu^+\mu^-$ events was estimated as:

$$N_{sig}^{\mu^+\mu^-} = N_{fit}^{\mu^+\mu^+} \cdot \frac{N_{IP<20}^{\mu^+\mu^+}}{N^{\mu^+\mu^+}} \cdot f_{\mu^+\mu^+ \ to \ \mu^+\mu^-} \tag{4.41}$$

The total error is dominated by the statistical uncertainty of the conversion factors and is ∼ 40%. The expected in time background estimated with the $\mu^+\mu^+$ vertices in bins of 2 MeV/c^2 and for each mass window is shown in Fig. 4.26.

4.9.3 Summary of the background estimation

The preliminary estimation of the number of background events in 2 MeV/c^2 mass bins and for each mass window is shown in Fig. 4.27. The expected number of events in a $\pm 3\sigma$ mass window corresponding to 300 MeV/c^2 is 2.7, which indicates that limits from Fig. 4.17 are going to be reduced by a factor of 2.6 assuming one-sided Poisson 95% CL limit.

The background prediction can be improved by studying MC samples with pileup activity included, in particular, samples with $K^+ \to \mu^+\nu$ and $K^+ \to \pi^+\pi^+\pi^-$ with forced pion decays. The predicted background can be further

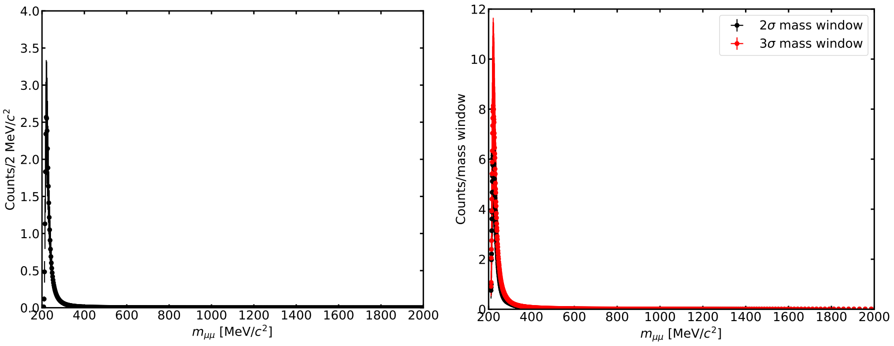

(A)

(B)

FIGURE 4.26: Expected number of the in time events in the blinded region as a function of the invariant dimuon mass in 2 MeV/c^2 bins (A) and for each mass window (B). The systematic error is about 40%.

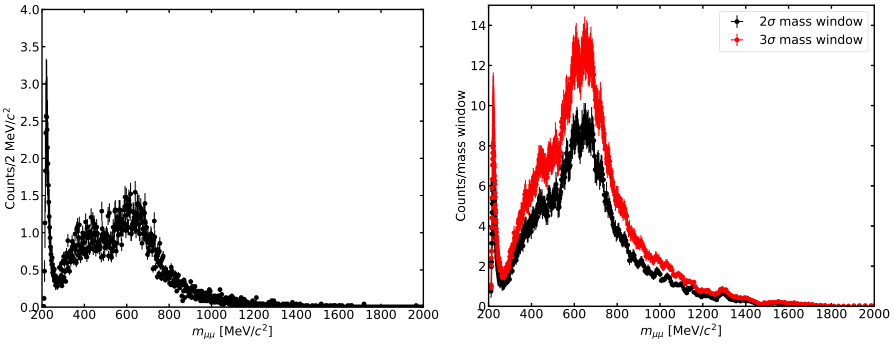

(A)

(B)

FIGURE 4.27: Expected number of background events in the blinded region estimated as a sum of combinatorial and prompt (in time) components as a function on the invariant dimuon mass in 2 MeV/c^2 bins (A) and for each mass window (B).

reduced by introducing stricter veto cuts. In particular, the condition on $K\mu2$ decay rejection can be replaced with the KTAG-based veto; however, this can reduce the signal acceptance by $\sim$ 10% due to the accidental activity. The effect of the cut on data was investigated using the following definition: all events with a KTAG candidate within 3 ns with respect to the track time and with a number of fired sectors higher than 4 are rejected. In this case, the in time component in the $\mu^+\mu^+$ sample coincides with the combinatorial (Fig. 4.28A). Therefore, it was assumed that the combinatorial component also dominates the background in the signal region. A preliminary background expectation with the KTAG veto applied is shown in Fig. 4.28B. The KTAG veto dramatically reduces in time contribution and suppress combinatorial background by a factor of 4. The expected background in a $\pm 3\sigma$ mass window corresponding to 300 MeV/c^2 is 1.2 events. Therefore, accounting for the 10% signal loss and 95% CL one-sided upper limit, the sensitivity from Fig. 4.17 is reduced by a factor of 1.7, which is $\sim$ 60% better than without the KTAG veto. A multivariate analysis based on variables such as the time difference between muon tracks, minimum distance to IP, Z position corresponding to the CDA of the vertex to the nominal beamline can be used to suppress the background further. It is possible that with this strategy, a zero-background hypothesis can be achieved without large signal losses. This idea, however, deserves a dedicated study, which is out of the scope of this thesis.

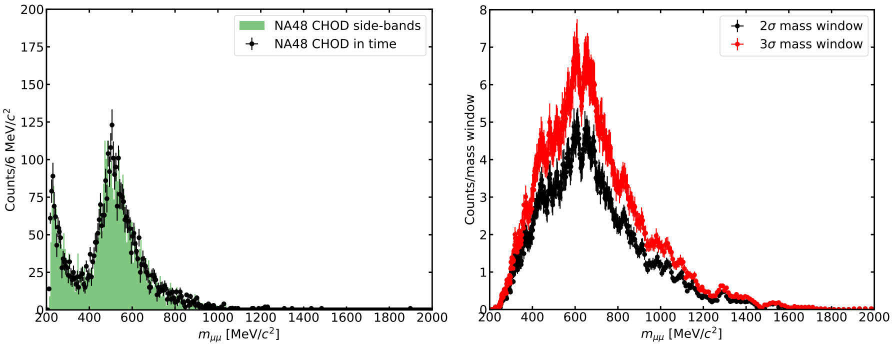

(A)

(B)

FIGURE 4.28: KTAG veto studies: (B) comparison between the dimuon mass distribution for the in time $\mu^+\mu^+$ events and events in the NA48 CHOD side-bands. (B) Expected number of background events in the signal region as a function of the invariant dimuon mass for each mass window.

4.10 Conclusions

This chapter presents a sensitivity study of the NA62 experiment to a light scalar or pseudoscalar with coupling to fermions produced in the rare decays of B-mesons. The model-independent approach, the analysis strategy, the signal Monte Carlo, and the analysis of data collected during 2017-2018 data taking periods were discussed.

As a result of this work, the new Monte Carlo simulation involving B-mesons was added to the NA62 Framework. Furthermore, the prepared B-meson distributions can also be used for other physics cases, for example, to simulate the HNL production.

In this work, the signal selection strategy was developed, and the signal acceptance was investigated along with the accidental signal rejection due to the veto conditions introduced in the selection. The size of the data sample collected in 2017-2018 was estimated as well. Additionally, the efficiency of the exotic trigger streams was studied in detail, and considerably large inefficiencies in the signal acceptance close to the kinematic threshold were discovered. Consequently, new possible triggers, which can be proposed to replace the inefficient ones, were investigated. The data rates of these conditions are to be tested at the beginning of the data taking in 2021.

Additionally, an investigation of possible background components, which can enter the signal region, was performed. As a result, a preliminary technique to estimate the background using the data-driven approach was developed. Further background rejection, especially in the mass range close to the kinematic threshold, can be achieved by applying the not-KTAG condition at the cost of 10% signal loss. Moreover, the zero-background level can possibly be achieved if a multivariate analysis is considered. In future, this result can be improved with the help of Monte Carlo samples with the pileup activity included. In particular, the signal MC sample should be reconstructed using the overlay technique; this will provide a more reliable estimation of the dimuon mass resolution, trigger, selection and random veto efficiencies.

Finally, the prepared background expectation can be used to evaluate the sensitivity of NA62 to other models, including exotic particles with coupling to fermions, for example, Dark Photons. The NA62MC already has an implementation of the Dark Photon production in $p-p$ interactions and in decays of mesons, which is being validated at the moment of writing the thesis.

The results of the work described in this chapter can be used to increase the sensitivity of NA62 to $B \to K^{(*)}\mathcal{A}, \mathcal{A} \to \mu^+\mu^-$ and other exotics processes in the future data taking, both in the kaon and in the beam dump mode of NA62. The NA62 experiment plans on taking data for at least two more years with an intensity of about 100% of the nominal one. More data is planned to be taken in the dump mode as well; this implies that with improved trigger conditions proposed in this work, the analysis can significantly improve the current sensitivity with a few 10^{17} POT collected, which can be achieved already in 2021.

Conclusions and Outlook

This thesis discusses the results of the two projects carried out within the NA62 collaboration of the fixed-target kaon experiment located in the North area of the CERN SPS.

The NA62 experiment aims to measure the ultra-rare kaon decay $K^+ \to \pi^+ \nu\bar{\nu}$ with 10% precision. This task is impossible without the beam spectrometer, hybrid silicon detector, GigaTracKer (GTK). The GTK was designed to sustain a gigahertz rate of 75 GeV$/c$ particles, and provide the single hit time, track momentum and angular resolutions better than 200 ps, $\delta p/p = 0.2\%$ and 16 μrad respectively. In the scope of this thesis, the development of the dedicated time calibration procedure, crucial for achieving the best timing performances of the GTK, was discussed. During the work on this project, a set of tools necessary to monitor the quality of the data collected by the GTK was implemented into the NA62 data processing routine. The timing performances of the GTK and effects of radiation damage on the detectors installed during the 2016-2018 data taking periods were also investigated. The products of this work are directly used in any physics analysis in NA62, which relies on the GTK. The conclusions of the radiation damage study described in this thesis indicate that modules can be safely reused with the bias voltage higher than 150 V even after being irradiated up to 4×10^{13} 1 MeV n_{eq}/cm^2. The latter is essential for the GTK working group since an additional GTK station will be installed starting from 2021, which will require higher production rates for the detector modules.

As a direct consequence of this work, the GTK module 7 was re-installed in the beamline in 2021 with the bias voltage set to 200 V. Additionally, the data quality monitoring tools and the time calibration proved to be working as expected during the online data processing.

The second project discussed in this thesis is concentrated on the searches for the New Physics processes. The studied process assumes the production of a pseudoscalar particle, ALP, in the $b \to s$ transitions with the subsequent decay of the ALP into a pair of muons inside the fiducial volume of NA62. The main idea of the search was to perform a model-independent analysis and treat the production and decay as unrelated parameters. A Monte Carlo simulation of the process was developed and implemented within the NA62 framework. The dedicated signal selection was prepared to perform searches using data collected in the kaon mode of NA62 data taking. The geometrical and signal acceptances and trigger efficiencies as a function of mass and lifetime were estimated using the signal Monte Carlo and tools developed within the NA62 collaboration. The size of the collected data sample was estimated as a total number of protons on target, POT, and was found to be $POT = (4.38 \pm 0.40) \times 10^{17}$. The effects of the random activity on the signal selections were studied, estimated and minimised using data. Finally, the evaluated sensitivity of NA62 to the process of interest assuming 0 background events, full selection, geometrical, trigger efficiencies and sample size for the most sensitive mass value was found to be well inside already covered parameter space. One of the crucial ingredients for this result was the efficiency and the downscaling factor of triggers used to collect the data sample for this search. In this study, changes for the most inefficient trigger conditions for future data taking were investigated and proposed. Regardless of the sensitivity loss, background studies using a data-driven approach were performed. It was identified that the dominant background component in the mass range close to the kinematic threshold is coming from $K^+ \to \pi^+\pi^+\pi^-$ decays with one or more pions decaying in flight, while in higher mass range, the background is represented by a random combination of muon tracks from kaon and pion decays. Both components can be largely suppressed by applying the veto conditions, particularly by using KTAG; however, this can be done at the cost of the signal acceptance loss ($\sim 10\%$ for KTAG). The studies performed in this project are particularly interesting for any similar data analysis carried out at NA62. Additionally, the results of this analysis can be interpreted in terms of the Dark Photon Standard Model extension or any other model involving particles with fermionic coupling.

The NA62 experiment plans to collect data at 100% of the nominal beam intensity during the physics run in 2021. If the dimuon mask remains in the list of the triggers, it would be possible to acquire about the same amount of data as in 2017. Concerning the beam-dump mode of the NA62 operation, it is planned to run for about a week in this mode with the beam intensity of 200% of the nominal. In this case, a sample of 10^{17} POT can be collected. If the trigger conditions are changed as proposed in this thesis, these samples can already provide a sizable improvement in the exclusion bounds. However, it would take one more year of the data taking to reach the desired sensitivity.

Appendix A

Output of GTK data quality monitoring tools

This appendix demonstrates an example of plots put in the `.pdf` reports of data quality monitoring analysers.

`GigaTrackerDataQualityMonitor`

The following figures show examples of plots produced by the`GigaTrackerDataQualityMonitor` for a run 8647 from the 2018 data taking period.

Fig. A.1A presents a fraction of events with good GTK event quality and a fraction of events with GTK candidates in time with $K2\pi$ and $K3\pi$. The efficiency of $K\pi\nu\nu$-like matching between GTK tracks and a single positive track from $K3\pi$ and $K2\pi$ events in bins of instantaneous beam intensity and for each burst is shown in Fig. A.1B and Fig. A.1C. Fig. A.1B shows that the efficiency is stable during the run and is around 80% for $K3\pi$ and 79% for $K2\pi$. On the contrary, the efficiency trend in Fig. A.1C decreases at higher values of instantaneous intensity. Moreover, there is a kink in the intensity range close to 0. This behaviour is due to the instantaneous intensity estimator computed using out of time GTK hits. It was discovered that the GTK-RO periodically loses a non-negligible amount of data (will be discussed later). This loss is responsible for the false-low instantaneous intensity values and, therefore, for the shape of the efficiency shown in Fig. A.1C.

The `.pdf` report of `GigaTrackerDataQualityMonitor` also contains the resolution and the mean of the time difference between GTK tracks and KTAG kaon candidates measured for each run (Fig. A.2A) and each burst. In addition, the same study is made for the resolution of the $K2\pi$ squared missing mass distribution m^2_{miss} (Fig. A.2B); it also is measured in pion momentum bins.

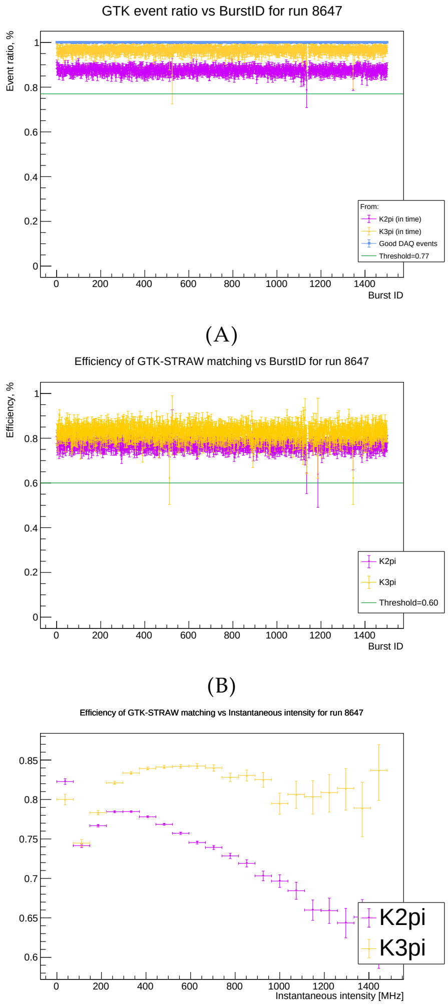

(A)

(B)

(C)

FIGURE A.1: (A) Fraction of events in a given burst with no readout or reconstruction problems (blue), with at least one reconstructed GTK track in time with $K2\pi$ (pink) and $K3\pi$ (yellow) decays. (B) GTK track reconstruction efficiency estimated using matching between GTK tracks and a single track from $K2\pi$ (pink) and $K3\pi$ (yellow) decays for each burst and in bins of instantaneous intensity (MHz) (C).

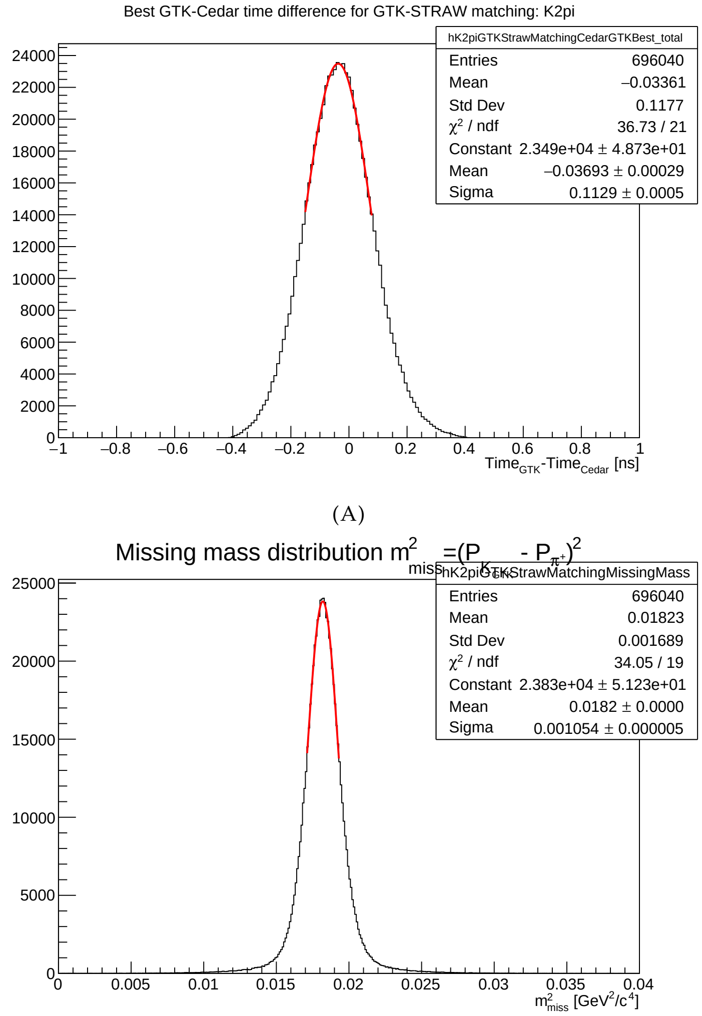

(A)

(B)

FIGURE A.2: (A) Example of the distribution of the time difference between GTK tracks and KTAG kaon candidates, run 8647 from the 2018 data taking period. (B) Example of the squared missing mass $m^2_{miss} = (P_K - P_\pi)^2$ distribution, run 8647 from 2018 data taking period. In both cases, the fit is shown as a red line.

From the plots, it can be seen that both parameters are consistent with the design specifications.

The ToT study is not included in the `.pdf` report but can be saved in `.root` format. For each chip, the pixel peak ToT value is extracted, and the full width at half maximum (FWHM) is computed as a measure of the width of the ToT peak. The values are stored in the dedicated `ROOT` `TGraph`. Fig. A.3 shows an example of such a study made for GTK module 7 chip 7 using data collected in 2018 (one of the most irradiated chips). It can be noted that pixels close to the beam spot (the first 400 pixels correspond to the last 10 rows of the TDCpix from the EoC) have an increasingly larger peak width than the ones far from the beam.

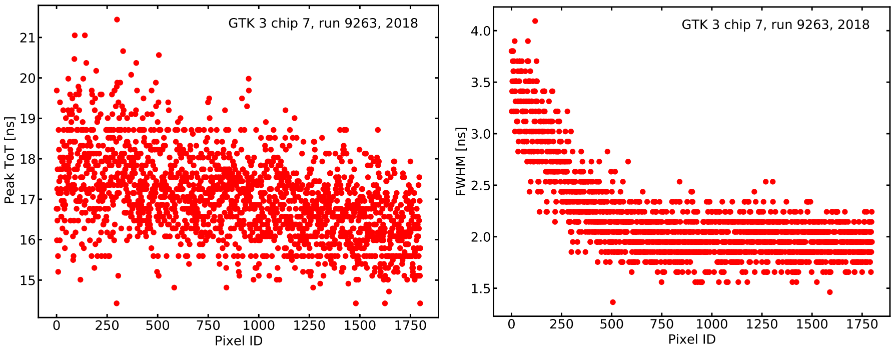

(A) (B)

FIGURE A.3: (A) Example of pixel peak ToT for each pixel in a single chip. The most irradiated GTK module was used for the plot. The peak ToT of the pixels in the shown chip slightly increases towards the area of the beam centre (first 400 pixel IDs). (B) Example of full width at half maximum (FWHM) for each pixel in a single chip. Here as well, the most irradiated module was used. In this case, an increase of 2 ns in the FWHM is clearly seen in the pixels near the beam centre (first 400 IDs).

`SpectrometerGigaTrackerMatchingEfficiency`

On the following plots, figures produced by the `SpectrometerGigaTrackerMatchingEfficiency` analyser and printed in the output `.pdf` report are shown.

It was not mentioned previously, but the analyser splits data into three samples to study the effect of GTK-RO inefficiencies. Fig. A.4 demonstrates the problems observed in the data collected by the GTK. The plot shows the time

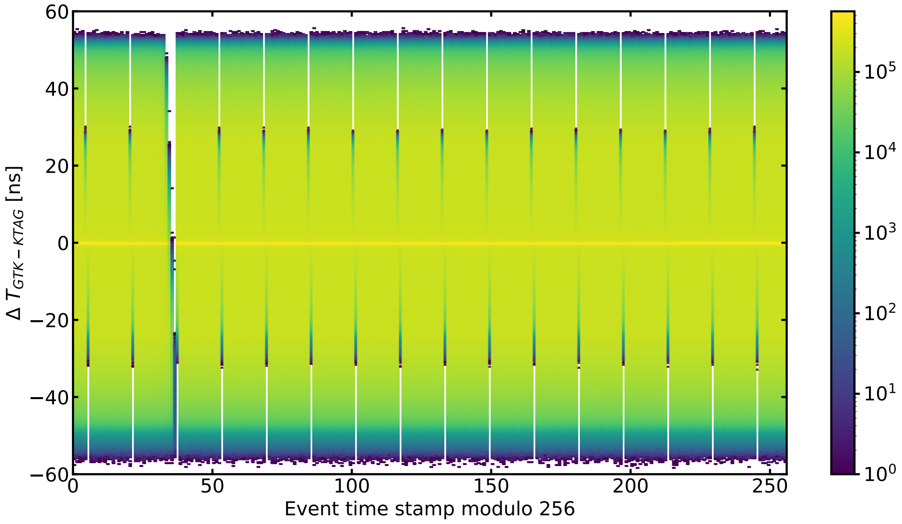

FIGURE A.4: Time difference between GTK hits and KTAG as a function of the event timestamp (L0 trigger timestamp) modulo 256. The plot was made using run 9263 from the 2018 data taking period. The inefficiencies can be seen as periodic gaps.

difference between GTK hit and KTAG kaon candidate as a function of trigger time stamp modulo 256, where each bin in the X-axis corresponds to an event inside one readout frame.[35] It can be seen that for some bins, one-third of the GTK event is missing – this is the problem arising from the GTK-RO, and it happens every 400 ns. Another consequence of the GTK-RO limitation is also very well visible – it is a big gap around $X = 36$ which corresponds to the end of the TDCpix readout frame. The hole is not in $X = 254$ because of the delays induced by cables from the TDCpix to the GTK-RO. Since cables of GTK stations were not aligned with each other during the data taking, readout inefficiencies in stations mostly do not overlap. The problems are currently being investigated and addressed by the GTK working group.

From the plot in Fig. A.4, it is clear that instantaneous intensity estimation is incorrect for events with the discussed problems since some part of out of time hits is missing. Moreover, events close to the end of the frame must be entirely excluded from the data analysis as most of them lose hits from the physics peak. Therefore, to account for all these features, the `SpectrometerGigaTrackerMatchingEfficiency` splits data into three samples: events with 400 ns inefficiency (A), events with the end of the frame inefficiency (B) and good events (C). The fractions of events in each sample are shown in Fig.

---

[35] TDCpix continuously reads out data in frames of $\sim$ 6.4 μs.

A.5. Inefficient events include all possible bad time stamps for all stations, which means that some of these events are good for certain stations due to the misalignment described above. The observed fractions are independent of the intensity as expected; statistical fluctuations are possible in the high-intensity bins.

In Fig. A.6, the matching efficiency described in section 3.3 is shown in bins of KTAG candidates as the instantaneous intensity estimator for each sample. Additionally, in the `.pdf` report, the efficiency is expressed in bins of the standard instantaneous intensity (from the GTK) and time within the burst. From Fig. A.6, it is evident that efficiency decreases with the instantaneous intensity, which is a consequence of the increasing contribution of pileup tracks. Notably, it can be seen that efficiencies for good events (sample C) and events from sample A are similar (about 3% of difference) – this can be explained by the fact that the 400 ns inefficiency rarely affects hits from the physics peak. Therefore, considering the total fraction of events in samples A and C is 97% (see Fig. A.5A and A.5C) and assuming an inefficiency of 3% for sample A, one obtains 96.1% as an estimation of overall GTK RO efficiency.[36]

Apart from the plots described above, the `.pdf` report contains the GTK-KTAG time resolution measurement expressed in terms of the number of KTAG candidates and the number of hits in GTK candidates (Fig. A.7). The overall trend in Fig. A.7A shows that GTK-KTAG time resolution degrades at higher instantaneous intensity values. As in the case of efficiency, the reason for such behaviour is the rising contribution of pileup tracks. As for Fig. A.7B, the time degradation in tracks with clusters of two or more pixels was also observed in the previous studies, and the possible explanation for this behaviour could be in the charge sharing between pixels in a cluster.

Finally, the `.pdf` report ends with inefficiency hit maps described in Fig. 3.10 and pixel time resolution maps as in Fig. 3.14.

As mentioned in section 3.3, both analysers are included in the NA62 data processing routine. The `.pdf` reports for each run are accessible for inspection for all members of the NA62 collaboration, along with other files produced by monitoring tools of other subsystems. Moreover, the NA62 data processing also runs during the data taking for instant quality evaluation of the collected data, allowing for quick intervention if needed.

---

[36] This is true only for intensities below 80% of nominal. At higher intensities, additional limitations of GTK-RO were discovered and are currently being investigated.

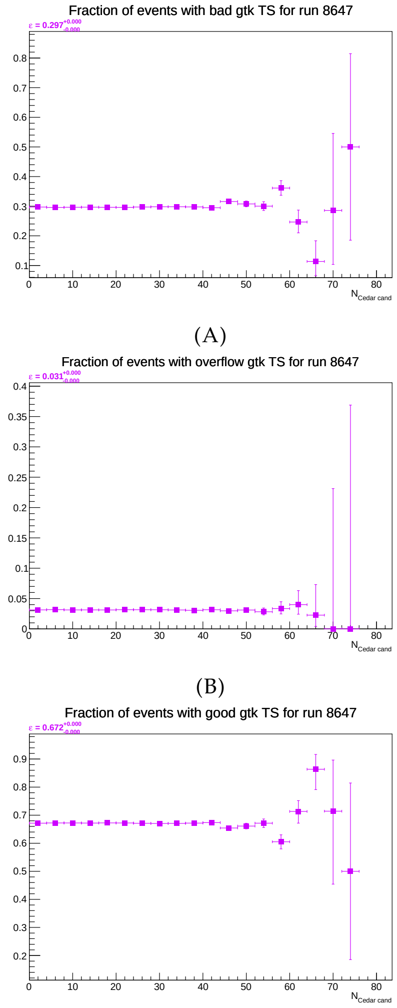

(A)

(B)

(C)

FIGURE A.5: Example of the event fraction found in each GTK data sample as a function of the number of KTAG candidates: (A) events with the inefficiency appearing every 400 ns (sample A), (B) events with the inefficiency appearing at the end of each readout frame (sample B), (C) good events (sample C).

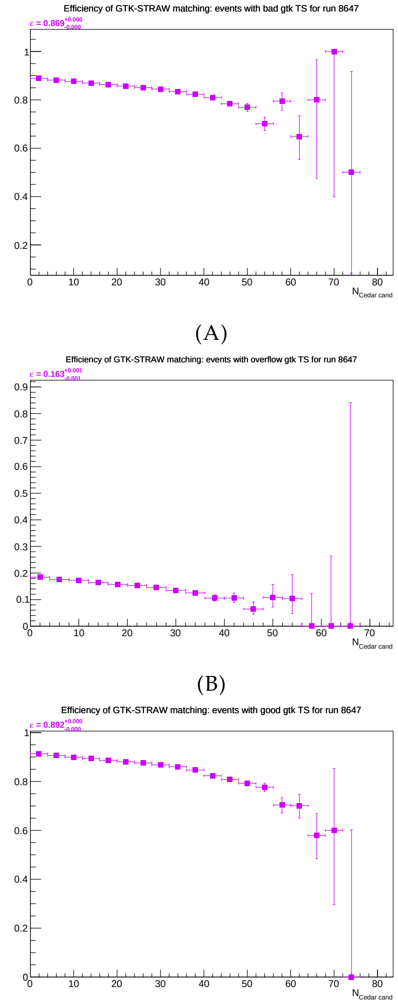

(A)

(B)

(C)

FIGURE A.6: Example of the GTK-$K3\pi$ discriminant based matching efficiency for each GTK data sample as a function of KTAG candidates: (A) events with the inefficiency appearing every 400 ns (sample A), (B) events with the inefficiency appearing at the end of each readout frame (sample B), (C) good events (sample C).

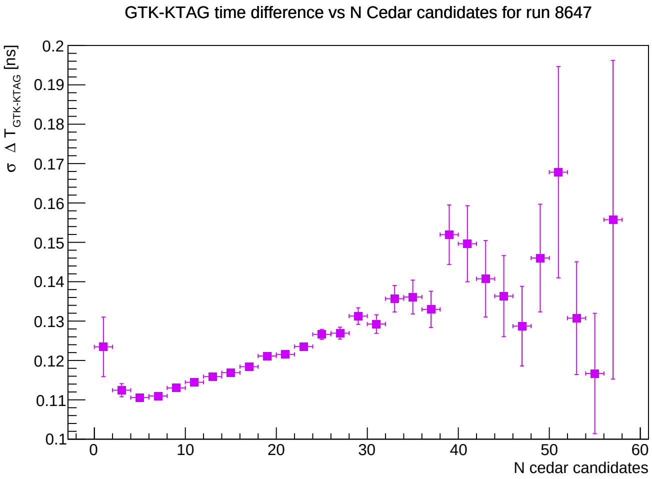

(A)

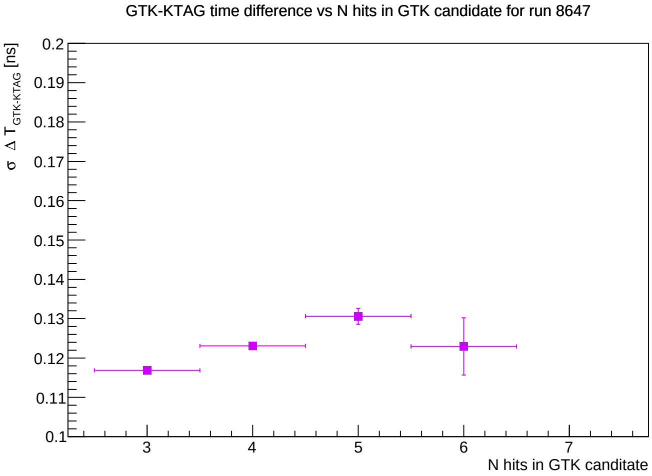

(B)

FIGURE A.7: Time resolution of the time difference between GTK tracks and KTAG kaon candidates as a function of the number of KTAG candidates (A) and the number of hits in the GTK track (B).

Appendix B

Time-over-threshold of some irradiated pixels

This appendix provides an example of the time distribution as a function of ToT for some of the most irradiated pixels in GTK module 7. The following plots were made with the help of the time calibration `TTree` using multiple consecutive runs taken at the end of the 2018 data taking period and before the bias voltage scan. The histograms are filled with all GTK hits without matching with any physics decay.

In Fig. B.1, time distributions as a function of ToT for several pixels from chip 8 row 0 (the closest row to the beam spot and the furthest from the EoC) are shown; no pixel time calibration was applied. From the slice at ToT$=$ 21.25 ns (each ToT bin in the histogram is $\sim$ 97 ps equal to the TDC bin size) in Fig. B.1A, it can be seen that the time resolution is more than two times worse compared to the normal pixel from the same row, see Fig. B.1C.[37] Moreover, in some pixels, one can observe a second peak in the time distribution in the same ToT bin (Fig. B.1B). The second peak appears in a similar location in most of the affected pixels. Since these pixels have the highest statistics in the chip, the time walk function starts to follow the second peak, causing miscalibration of the order of several nanoseconds in the ToT range above $\sim$ 20 ns. Most of the irradiated chips in module 7 were affected by this feature. So far, a solution to mitigate the problem in the calibration was not found.

Notably, most pixels from the inefficient area in Fig. 3.14A have similar characteristics shown in this Appendix. Investigations on the causes of this behaviour are ongoing. However, it is clear that the effect is connected to the irradiation of the sensor since it disappears with the increase of the bias voltage.

---

[37] Here, column numbering is inverted compared to TDCpix column ID, i.e. column 0 here is column 40 for TDCpix.

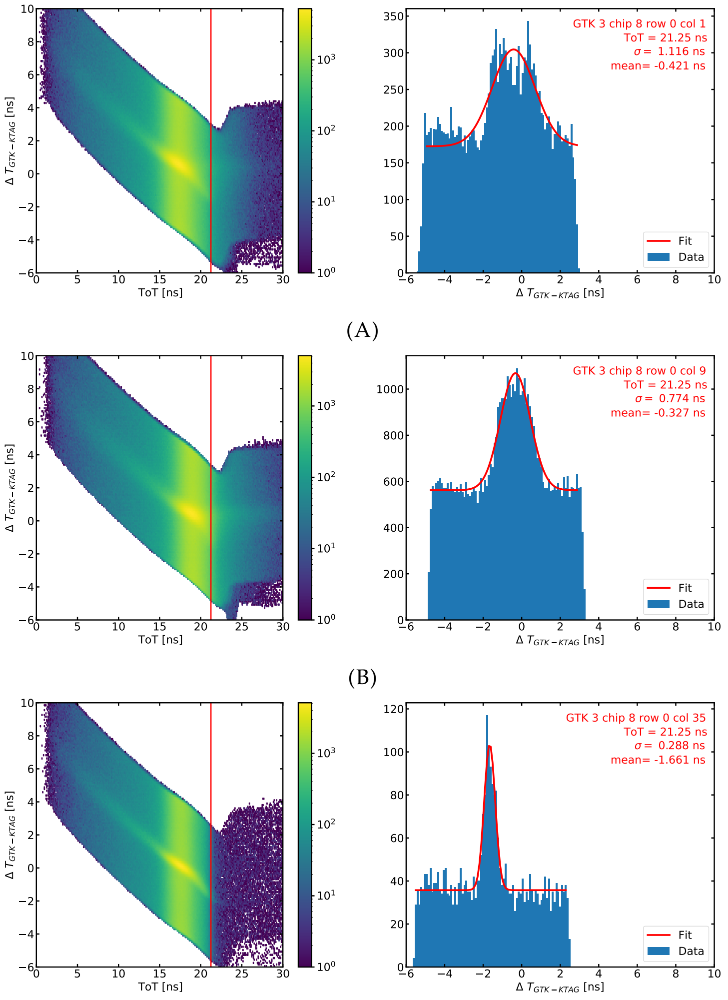

(A)

(B)

(C)

FIGURE B.1: Time difference between GTK hits and KTAG kaon candidates as a function of ToT for a single pixel (left) and the same difference at the selected ToT= 21.25 ns (right). (A) Closest pixel from the selected chip to the beam centre. (B) Pixel from the same row same chip as (A), but slightly further from the beam spot. (C) Pixel from the same row as (A) and (B) but located further from the beam spot compared to (A) and (B). The vertical red line indicates the selected ToT bin. The most irradiated module, GTK module 7, was used for the plots. The data corresponds to several runs at the end of the 2018 data taking period. The bias voltage was set to 100 V.

Bibliography

[1] S. Chatrchyan et al. “Observation of a new boson at a mass of 125 GeV with the CMS experiment at the LHC”. In: *Physics Letters B* 716.1 (2012), pp. 30–61. DOI: `10.1016/j.physletb.2012.08.021`. arXiv: `1207.7235`.

[2] G. Aad et al. “Observation of a new particle in the search for the Standard Model Higgs boson with the ATLAS detector at the LHC”. In: *Physics Letters B* 716.1 (2012), pp. 1–29. DOI: `10.1016/j.physletb.2012.08.020`. arXiv: `1207.7214`.

[3] P. A. R. Ade et al. “Planck 2015 results. XIII. Cosmological parameters”. In: *Astronomy & Astrophysics* 594 (2016), A13. DOI: `10.1051/0004-6361/201525830`.

[4] Andrei D Sakharov. “Violation of CP invariance, C asymmetry, and baryon asymmetry of the universe”. In: *Soviet Physics Uspekhi* 34.5 (1991), pp. 392–393. DOI: `10.1070/PU1991v034n05ABEH002497`.

[5] Y. Fukuda et al. “Evidence for Oscillation of Atmospheric Neutrinos”. In: *Physical Review Letters* 81.8 (1998), pp. 1562–1567. DOI: `10.1103/PhysRevLett.81.1562`. arXiv: `9807003 [hep-ex]`.

[6] Q. R. Ahmad et al. “Measurement of the Rate of $\nu_e + d \rightarrow p + p + e^-$ Interactions Produced by ^8B Solar Neutrinos at the Sudbury Neutrino Observatory”. In: *Physical Review Letters* 87.7 (2001), p. 071301. DOI: `10.1103/PhysRevLett.87.071301`. arXiv: `0106015 [nucl-ex]`.

[7] Steven Weinberg. “A Model of Leptons”. In: *Physical Review Letters* 19.21 (1967), pp. 1264–1266. DOI: `10.1103/PhysRevLett.19.1264`.

[8] Sheldon L. Glashow. “Partial-symmetries of weak interactions”. In: *Nuclear Physics* 22.4 (1961), pp. 579–588. DOI: `10.1016/0029-5582(61)90469-2`.

[9] A. Salam and J. C. Ward. “Electromagnetic and weak interactions”. In: *Physics Letters* 13.2 (1964), pp. 168–171. DOI: `10.1016/0031-9163(64)90711-5`.

[10] J. H. Christenson et al. “Evidence for the 2 π Decay of the K_2^0 Meson”. In: *Physical Review Letters* 13.4 (1964), pp. 138–140. DOI: `10.1103/PhysRevLett.13.138`.

[11] Nicola Cabibbo. “Unitary Symmetry and Leptonic Decays”. In: *Physical Review Letters* 10.12 (1963), pp. 531–533. DOI: `10.1103/PhysRevLett.10.531`.

[12] B. J. Bjørken and S. L. Glashow. "Elementary particles and SU(4)". In: *Physics Letters* 11.3 (1964), pp. 255–257. DOI: `10.1016/0031-9163(64)90433-0`.

[13] S. L. Glashow, J. Iliopoulos, and L. Maiani. "Weak Interactions with Lepton-Hadron Symmetry". In: *Physical Review D* 2.7 (1970), pp. 1285–1292. DOI: `10.1103/PhysRevD.2.1285`.

[14] J. J. Aubert et al. "Experimental observation of a heavy particle J". In: *Physical Review Letters* 33.23 (1974), pp. 1404–1406. DOI: `10.1103/PhysRevLett.33.1404`.

[15] J. E. Augustin et al. "Discovery of a narrow resonance in e+e- annihilation". In: *Physical Review Letters* 33.23 (1974), pp. 1406–1408. DOI: `10.1103/PhysRevLett.33.1406`.

[16] Makoto Kobayashi and Toshihide Maskawa. "CP -Violation in the Renormalizable Theory of Weak Interaction ". In: *Progress of Theoretical Physics* 49.2 (1973), pp. 652–657. DOI: `10.1143/ptp.49.652`.

[17] Lincoln Wolfenstein. "Parametrization of the Kobayashi-Maskawa Matrix". In: *Physical Review Letters* 51.21 (1983), pp. 1945–1947. DOI: `10.1103/PhysRevLett.51.1945`.

[18] P A Zyla and Others. "Review of Particle Physics". In: *PTEP* 2020.8 (2020), p. 083C01. DOI: `10.1093/ptep/ptaa104`.

[19] C. Jarlskog. "Commutator of the Quark Mass Matrices in the Standard Electroweak Model and a Measure of Maximal CP Nonconservation". In: *Physical Review Letters* 55.10 (1985), pp. 1039–1042. DOI: `10.1103/PhysRevLett.55.1039`.

[20] Ziro Maki, Masami Nakagawa, and Shoichi Sakata. "Remarks on the Unified Model of Elementary Particles". In: *Progress of Theoretical Physics* 28.5 (1962), pp. 870–880. DOI: `10.1143/ptp.28.870`.

[21] Ivan Esteban et al. "The fate of hints: updated global analysis of three-flavor neutrino oscillations". In: *Journal of High Energy Physics* 2020.9 (2020), p. 178. DOI: `10.1007/JHEP09(2020)178`. arXiv: `2007.14792`.

[22] Steven Weinberg. "The U(1) problem". In: *Physical Review D* 11.12 (1975), pp. 3583–3593. DOI: `10.1103/PhysRevD.11.3583`.

[23] G. 't Hooft. "Computation of the quantum effects due to a four-dimensional pseudoparticle". In: *Physical Review D* 14.12 (1976), pp. 3432–3450. DOI: `10.1103/PhysRevD.14.3432`.

[24] G. 't Hooft. "Symmetry Breaking through Bell-Jackiw Anomalies". In: *Physical Review Letters* 37.1 (1976), pp. 8–11. DOI: `10.1103/PhysRevLett.37.8`.

[25] J. M. Pendlebury et al. "Revised experimental upper limit on the electric dipole moment of the neutron". In: *Physical Review D* 92.9 (2015), p. 092003. DOI: `10.1103/PhysRevD.92.092003`. arXiv: `1509.04411`.

[26] B. K. Sahoo. "Improved limits on the hadronic and semihadronic CP violating parameters and role of a dark force carrier in the electric dipole

moment of Hg 199". In: *Physical Review D* 95.1 (2017), p. 013002. DOI: `10.1103/PhysRevD.95.013002`. arXiv: `1612.09371`.

[27] C. Abel et al. "Measurement of the Permanent Electric Dipole Moment of the Neutron". In: *Physical Review Letters* 124.8 (2020), p. 081803. DOI: `10.1103/PhysRevLett.124.081803`. arXiv: `2001.11966`.

[28] R. D. Peccei and Helen R. Quinn. "CP conservation in the presence of pseudoparticles". In: *Physical Review Letters* 38.25 (1977), pp. 1440–1443. DOI: `10.1103/PhysRevLett.38.1440`.

[29] R.N. Mohapatra and G. Senjanović. "Natural suppression of strong P and T non-invariance". In: *Physics Letters B* 79.3 (1978), pp. 283 –286. DOI: `https://doi.org/10.1016/0370-2693(78)90243-5`.

[30] Ann Nelson. "Naturally weak CP violation". In: *Physics Letters B* 136.5 (1984), pp. 387 –391. DOI: `https://doi.org/10.1016/0370-2693(84)92025-2`.

[31] S. M. Barr. "Solving the Strong CP Problem without the Peccei-Quinn Symmetry". In: *Physical Review Letters* 53.4 (1984), pp. 329–332. DOI: `10.1103/PhysRevLett.53.329`.

[32] Wen-Yuan Ai et al. "Absence of CP violation in the strong interactions". In: (2020). arXiv: `2001.07152 [hep-th]`.

[33] Steven Weinberg. "A New Light Boson?" In: *Physical Review Letters* 40.4 (1978), pp. 223–226. DOI: `10.1103/PhysRevLett.40.223`.

[34] F. Wilczek. "Problem of Strong P and T Invariance in the Presence of Instantons". In: *Physical Review Letters* 40.5 (1978), pp. 279–282. DOI: `10.1103/PhysRevLett.40.279`.

[35] Marco Gorghetto and Giovanni Villadoro. "Topological susceptibility and QCD axion mass: QED and NNLO corrections". In: *Journal of High Energy Physics* 2019.3 (2019), p. 33. DOI: `10.1007/JHEP03(2019)033`. arXiv: `1812.01008`.

[36] Jihn E. Kim. *Light pseudoscalars, particle physics and cosmology*. 1987. DOI: `10.1016/0370-1573(87)90017-2`.

[37] M A Shifman, A I Vainshtein, and V I Zakharov. "Can confinement ensure natural CP invariance of strong interactions?" In: *Nuclear Physics B* 166.3 (1980), pp. 493–506. DOI: `https://doi.org/10.1016/0550-3213(80)90209-6`.

[38] Jihn E. Kim. "Weak-Interaction Singlet and Strong CP Invariance". In: *Physical Review Letters* 43.2 (1979), pp. 103–107. DOI: `10.1103/PhysRevLett.43.103`.

[39] Michael Dine, Willy Fischler, and Mark Srednicki. "A simple solution to the strong CP problem with a harmless axion". In: *Physics Letters B* 104.3 (1981), pp. 199–202. DOI: `https://doi.org/10.1016/0370-2693(81)90590-6`.

[40] A.R. Zhitnitsky. "On Possible Suppression of the Axion Hadron Interactions. (In Russian)". In: *Sov.J.Nucl.Phys.* 31 (1980), p. 260.

[41] Joerg Jaeckel and Andreas Ringwald. “The Low-Energy Frontier of Particle Physics”. In: *Annual Review of Nuclear and Particle Science* 60.1 (2010), pp. 405–437. DOI: `10.1146/annurev.nucl.012809.104433`.

[42] B. Abi et al. “Measurement of the Positive Muon Anomalous Magnetic Moment to 0.46 ppm”. In: *Phys. Rev. Lett.* 126 (14 2021), p. 141801. DOI: `10.1103/PhysRevLett.126.141801`.

[43] T. Aoyama et al. “The anomalous magnetic moment of the muon in the Standard Model”. In: *Physics Reports* 887 (2020). The anomalous magnetic moment of the muon in the Standard Model, pp. 1–166. DOI: `https://doi.org/10.1016/j.physrep.2020.07.006`.

[44] Claudia Cornella, Paride Paradisi, and Olcyr Sumensari. “Hunting for ALPs with lepton flavor violation”. In: *Journal of High Energy Physics* 2020.1 (2020), p. 158. DOI: `10.1007/JHEP01(2020)158`. arXiv: `1911.06279`.

[45] Martin Bauer et al. “Axionlike Particles, Lepton-Flavor Violation, and a New Explanation of a_μ and a_e”. In: *Physical Review Letters* 124.21 (2020), p. 211803. DOI: `10.1103/PhysRevLett.124.211803`. arXiv: `1908.00008`.

[46] Darwin Chang et al. “Large two-loop contributions to $g-2$ from a generic pseudoscalar boson”. In: *Physical Review D* 63.9 (2001), p. 091301. DOI: `10.1103/PhysRevD.63.091301`. arXiv: `0009292 [hep-ph]`.

[47] Edward Witten. “Some properties of O(32) superstrings”. In: *Physics Letters B* 149.4 (1984), pp. 351–356. DOI: `https://doi.org/10.1016/0370-2693(84)90422-2`.

[48] Joseph P Conlon. “The QCD axion and moduli stabilisation”. In: *Journal of High Energy Physics* 2006.05 (2006), pp. 078–078. DOI: `10.1088/1126-6708/2006/05/078`. arXiv: `0602233 [hep-th]`.

[49] Peter Svrcek and Edward Witten. “Axions in string theory”. In: *Journal of High Energy Physics* 2006.06 (2006), pp. 051–051. DOI: `10.1088/1126-6708/2006/06/051`. arXiv: `0605206 [hep-th]`.

[50] Asimina Arvanitaki et al. “String axiverse”. In: *Physical Review D* 81.12 (2010), p. 123530. DOI: `10.1103/PhysRevD.81.123530`. arXiv: `0905.4720`.

[51] Bobby Samir Acharya, Konstantin Bobkov, and Piyush Kumarf. “An M theory solution to the strong CP-problem, and constraints on the axiverse”. In: *Journal of High Energy Physics* 2010.11 (2010), p. 105. DOI: `10.1007/JHEP11(2010)105`. arXiv: `1004.5138`.

[52] Michele Cicoli, Mark D. Goodsell, and Andreas Ringwald. “The type IIB string axiverse and its low-energy phenomenology”. In: *Journal of High Energy Physics* 2012.10 (2012), p. 146. DOI: `10.1007/JHEP10(2012)146`. arXiv: `1206.0819`.

[53] L F Abbott and P Sikivie. “A cosmological bound on the invisible axion”. In: *Physics Letters B* 120.1 (1983), pp. 133–136. DOI: `https://doi.org/10.1016/0370-2693(83)90638-X`.

[54] Michael Dine and Willy Fischler. "The not-so-harmless axion". In: *Physics Letters B* 120.1 (1983), pp. 137–141. DOI: `https://doi.org/10.1016/0370-2693(83)90639-1`.

[55] John Preskill, Mark B Wise, and Frank Wilczek. "Cosmology of the invisible axion". In: *Physics Letters B* 120.1 (1983), pp. 127–132. DOI: `https://doi.org/10.1016/0370-2693(83)90637-8`.

[56] Paola Arias et al. "WISPy cold dark matter". In: *Journal of Cosmology and Astroparticle Physics* 2012.06 (2012), pp. 013–013. DOI: `10.1088/1475-7516/2012/06/013`. arXiv: `1201.5902`.

[57] Maurizio Giannotti et al. "Cool WISPs for stellar cooling excesses". In: *Journal of Cosmology and Astroparticle Physics* 2016.05 (2016), pp. 057–057. DOI: `10.1088/1475-7516/2016/05/057`. arXiv: `1512.08108`.

[58] D Horns and M Meyer. "Indications for a pair-production anomaly from the propagation of VHE gamma-rays". In: *Journal of Cosmology and Astroparticle Physics* 2012.02 (2012), pp. 033–033. DOI: `10.1088/1475-7516/2012/02/033`. arXiv: `1201.4711`.

[59] Brian Batell, Maxim Pospelov, and Adam Ritz. "Exploring portals to a hidden sector through fixed targets". In: *Physical Review D* 80.9 (2009), p. 095024. DOI: `10.1103/PhysRevD.80.095024`. arXiv: `0906.5614`.

[60] J. Beacham et al. "Physics Beyond Colliders at CERN: Beyond the Standard Model Working Group Report". In: *Journal of Physics G: Nuclear and Particle Physics* 47.1 (2019). DOI: `10.1088/1361-6471/ab4cd2`. arXiv: `1901.09966`.

[61] Igor G Irastorza and Javier Redondo. "New experimental approaches in the search for axion-like particles". In: *Progress in Particle and Nuclear Physics* 102 (2018), pp. 89–159. DOI: `https://doi.org/10.1016/j.ppnp.2018.05.003`. arXiv: `1801.08127`.

[62] P. Sikivie. "Experimental Tests of the "Invisible" Axion". In: *Physical Review Letters* 51.16 (1983), pp. 1415–1417. DOI: `10.1103/PhysRevLett.51.1415`.

[63] Javier Redondo. "Solar axion flux from the axion-electron coupling". In: *Journal of Cosmology and Astroparticle Physics* 2013.12 (2013), pp. 008–008. DOI: `10.1088/1475-7516/2013/12/008`. arXiv: `1310.0823`.

[64] K. Van Bibber et al. "Proposed experiment to produce and detect light pseudoscalars". In: *Physical Review Letters* 59.7 (1987), pp. 759–762. DOI: `10.1103/PhysRevLett.59.759`.

[65] L. Maiani, R. Petronzio, and E. Zavattini. "Effects of nearly massless, spin-zero particles on light propagation in a magnetic field". In: *Physics Letters B* 175.3 (1986), pp. 359–363. DOI: `10.1016/0370-2693(86)90869-5`.

[66] R. Ballou et al. "New exclusion limits on scalar and pseudoscalar axionlike particles from light shining through a wall". In: *Physical Review D* 92.9 (2015), p. 092002. DOI: `10.1103/PhysRevD.92.092002`. arXiv: `1506.08082`.

[67] Federico Della Valle et al. "The PVLAS experiment: measuring vacuum magnetic birefringence and dichroism with a birefringent Fabry–Perot cavity". In: *European Physical Journal C* 76.1 (2016), pp. 1–15. DOI: `10.1140/epjc/s10052-015-3869-8`. arXiv: `1510.08052`.

[68] N. Du et al. "Search for Invisible Axion Dark Matter with the Axion Dark Matter Experiment". In: *Physical Review Letters* 120.15 (2018), p. 151301. DOI: `10.1103/PhysRevLett.120.151301`. arXiv: `1804.05750`.

[69] V. Anastassopoulos et al. "New CAST limit on the axion-photon interaction". In: *Nature Physics* 13.6 (2017), pp. 584–590. DOI: `10.1038/nphys4109`. arXiv: `1705.02290`.

[70] R.R. Dusaev, D.V. Kirpichnikov, and M.M. Kirsanov. "Photoproduction of axionlike particles in the NA64 experiment". In: *Physical Review D* 102.5 (2020), p. 055018. DOI: `10.1103/PhysRevD.102.055018`. arXiv: `2004.04469`.

[71] Babette Döbrich, Joerg Jaeckel, and Tommaso Spadaro. "Light in the beam dump. Axion-Like Particle production from decay photons in proton beam-dumps". In: *Journal of High Energy Physics* 2019.5 (2019), p. 213. DOI: `10.1007/JHEP05(2019)213`. arXiv: `1904.02091`.

[72] Matthew J. Dolan et al. "Revised constraints and Belle II sensitivity for visible and invisible axion-like particles". In: *Journal of High Energy Physics* 2017.12 (2017), p. 94. DOI: `10.1007/JHEP12(2017)094`. arXiv: `1709.00009`.

[73] Simon Knapen et al. "Searching for Axionlike Particles with Ultraperipheral Heavy-Ion Collisions". In: *Physical Review Letters* 118.17 (2017), p. 171801. DOI: `10.1103/PhysRevLett.118.171801`. arXiv: `1607.06083`.

[74] Adrian Ayala et al. "Revisiting the Bound on Axion-Photon Coupling from Globular Clusters". In: *Physical Review Letters* 113.19 (2014), p. 191302. DOI: `10.1103/PhysRevLett.113.191302`. arXiv: `1406.6053`.

[75] N. Vinyoles et al. "New axion and hidden photon constraints from a solar data global fit". In: *Journal of Cosmology and Astroparticle Physics* 2015.10 (2015), pp. 015–015. DOI: `10.1088/1475-7516/2015/10/015`. arXiv: `1501.01639`.

[76] Eduard Massó and Ramon Toldrà. "Light spinless particle coupled to photons". In: *Physical Review D* 52.4 (1995), pp. 1755–1763. DOI: `10.1103/PhysRevD.52.1755`. arXiv: `9503293`.

[77] Davide Cadamuro et al. "Cosmological bounds on sub-MeV mass axions". In: *Journal of Cosmology and Astroparticle Physics* 2011.02 (2011), pp. 003–003. DOI: `10.1088/1475-7516/2011/02/003`. arXiv: `1011.3694`.

[78] Babette Döbrich. "Axion-like Particles from Primakov production in beam-dumps". In: (2017). arXiv: `1708.05776`.

[79] M W Krasny and Others. "RECENT SEARCHES FOR SHORTLIVED PSEUDOSCALAR BOSONS IN ELECTRON BEAM DUMP EXPERIMENTS". In: *International Europhysics Conference on High-energy Physics*. 1987.

[80] J. D. Bjorken et al. "Search for neutral metastable penetrating particles produced in the SLAC beam dump". In: *Physical Review D* 38.11 (1988), pp. 3375–3386. DOI: `10.1103/PhysRevD.38.3375`.

[81] F Bergsma et al. "Search for axion-like particle production in 400 GeV proton-copper interactions". In: *Physics Letters B* 157.5 (1985), pp. 458–462. DOI: `https://doi.org/10.1016/0370-2693(85)90400-9`.

[82] J. Blümlein et al. "Limits on neutral light scalar and pseudoscalar particles in a proton beam dump experiment". In: *Zeitschrift für Physik C Particles and Fields* 51.3 (1991), pp. 341–350. DOI: `10.1007/BF01548556`.

[83] G. Abbiendi et al. "Multi-photon production in e^+e^- collisions at $\sqrt{s} = 181 - 209\ GeV$: The OPAL collaboration". In: *European Physical Journal C* 26.3 (2003), pp. 331–344. DOI: `10.1140/epjc/s2002-01074-5`. arXiv: `0210016 [hep-ex]`.

[84] F. Abudinén et al. "Search for Axionlike Particles Produced in e^+e^- Collisions at Belle II". In: *Physical Review Letters* 125.16 (2020), p. 161806. DOI: `10.1103/PhysRevLett.125.161806`. arXiv: `2007.13071`.

[85] The BaBar Collaboration and B. Aubert. "Search for Invisible Decays of a Light Scalar in Radiative Transitions $Upsilon(3S) \to \gamma\ A_0$". In: (2008). arXiv: `0808.0017`.

[86] Daniel Aloni et al. "Photoproduction of Axionlike Particles". In: *Physical Review Letters* 123.7 (2019), p. 071801. DOI: `10.1103/PhysRevLett.123.071801`. arXiv: `1903.03586`.

[87] Jonathan L. Feng et al. "Axionlike particles at FASER: The LHC as a photon beam dump". In: *Physical Review D* 98.5 (2018), p. 055021. DOI: `10.1103/PhysRevD.98.055021`. arXiv: `1806.02348`.

[88] Babette Döbrich et al. "ALPtraum: ALP production in proton beam dump experiments". In: *Journal of High Energy Physics* 2016.2 (2016), pp. 1–27. DOI: `10.1007/JHEP02(2016)018`. arXiv: `1512.03069`.

[89] Asher Berlin et al. "Dark sectors at the Fermilab SeaQuest experiment". In: *Physical Review D* 98.3 (2018), p. 035011. DOI: `10.1103/PhysRevD.98.035011`. arXiv: `1804.00661`.

[90] Akitaka Ariga et al. "FASER's physics reach for long-lived particles". In: *Physical Review D* 99.9 (2019), p. 095011. DOI: `10.1103/PhysRevD.99.095011`. arXiv: `1811.12522`.

[91] A. V. Artamonov et al. "Study of the decay $K^+ \to \pi^+\nu\bar{\nu}$ in the momentum region $140 < P_\pi < 199\ MeV/c$". In: *Physical Review D* 79.9 (2009), p. 092004. DOI: `10.1103/PhysRevD.79.092004`.

[92] R. Ammar et al. "Search for the Familon via $B^\pm \to \pi^\pm X^0$, $B^\pm \to K^\pm X^0$ and $B^0 \to K^0_S X^0$ Decays". In: *Physical Review Letters* 87.27 (2001), p. 271801. DOI: `10.1103/PhysRevLett.87.271801`.

[93] NA62 Collaboration. "Search for π^0 decays to invisible particles". In: *to be submitted to JHEP* (2020). arXiv: `2010.07644`.

[94] Babette Döbrich et al. "Model-independent bounds on light pseudoscalars from rare B-meson decays". In: *Physics Letters B* 790 (2019), pp. 537–544. DOI: `10.1016/j.physletb.2019.01.064`. arXiv: `1810.11336`.

[95] R. Aaij et al. "Search for long-lived scalar particles in $B^+ \to K^+\chi(\mu^+\mu^-)$ decays". In: *Physical Review D* 95.7 (2017), p. 071101. DOI: `10.1103/PhysRevD.95.071101`.

[96] R. Aaij et al. "Search for Hidden-Sector Bosons in $B^0 \to K^{*0}\mu^+\mu^-$ Decays". In: *Physical Review Letters* 115.16 (2015), p. 161802. DOI: `10.1103/PhysRevLett.115.161802`.

[97] V. Khachatryan et al. "Observation of the rare $B_s^0 \to \mu^+\mu^-$ decay from the combined analysis of CMS and LHCb data". In: *Nature* 522.7554 (2015), pp. 68–72. DOI: `10.1038/nature14474`. arXiv: `1411.4413`.

[98] J. P. Lees et al. "Search for di-muon decays of a low-mass Higgs boson in radiative decays of the Υ $(1S)$". In: *Physical Review D* 87.3 (2013), p. 031102. DOI: `10.1103/PhysRevD.87.031102`. arXiv: `1210.0287`.

[99] Matthew J. Dolan et al. "A taste of dark matter: flavour constraints on pseudoscalar mediators". In: *Journal of High Energy Physics* 2015.3 (2015), p. 171. DOI: `10.1007/JHEP03(2015)171`. arXiv: `1412.5174`.

[100] Changbo Fu et al. "Limits on Axion Couplings from the First 80 Days of Data of the PandaX-II Experiment". In: *Physical Review Letters* 119.18 (2017), p. 181806. DOI: `10.1103/PhysRevLett.119.181806`. arXiv: `1707.07921v2`.

[101] E. Aprile et al. "Excess electronic recoil events in XENON1T". In: *Physical Review D* 102.7 (2020), p. 072004. DOI: `10.1103/PhysRevD.102.072004`. arXiv: `2006.09721`.

[102] Daniel Aloni, Yotam Soreq, and Mike Williams. "Coupling QCD-Scale Axionlike Particles to Gluons". In: *Physical Review Letters* 123.3 (2019), p. 031803. DOI: `10.1103/PhysRevLett.123.031803`. arXiv: `1811.03474`.

[103] J. P. Lees et al. "Measurements of branching fractions and CP asymmetries and studies of angular distributions for $B \to \phi\phi K$ decays". In: *Physical Review D* 84.1 (2011), p. 012001. DOI: `10.1103/PhysRevD.84.012001`. arXiv: `1105.5159`.

[104] B. Aubert et al. "Study of B Meson Decays with Excited η and $\eta^{'}$ Mesons". In: *Physical Review Letters* 101.9 (2008), p. 091801. DOI: `10.1103/PhysRevLett.101.091801`. arXiv: `0804.0411`.

[105] V. Chobanova et al. "Measurement of branching fractions and CP violation parameters in $B \to \omega K$ decays with first evidence of CP violation in $B^0 \to \omega K_s^0$". In: *Physical Review D* 90.1 (2014), p. 012002. DOI: `10.1103/PhysRevD.90.012002`. arXiv: `1311.6666`.

[106] C. Lazzeroni et al. "Study of the $K^\pm \to \pi^\pm\gamma\gamma$ decay by the NA62 experiment". In: *Physics Letters, Section B: Nuclear, Elementary Particle and*

High-Energy Physics 732 (2014), pp. 65–74. DOI: `10.1016/j.physletb.2014.03.016`. arXiv: `1402.4334`.

[107] E. Abouzaid et al. "Final results from the KTeV experiment on the decay $K_L \to \pi^0\gamma\gamma$". In: *Physical Review D - Particles, Fields, Gravitation and Cosmology* 77.11 (2008), p. 112004. DOI: `10.1103/PhysRevD.77.112004`. arXiv: `0805.0031`.

[108] E. Cortina Gil et al. "The beam and detector of the NA62 experiment at CERN". In: *Journal of Instrumentation* 12.05 (2017), P05025–P05025. DOI: `10.1088/1748-0221/12/05/P05025`. arXiv: `1703.08501`.

[109] Andrzej J. Buras et al. "$K^+ \to \pi^+\nu\bar{\nu}$ and $K_L \to \pi^0\nu\bar{\nu}$ in the Standard Model: status and perspectives". In: *Journal of High Energy Physics* 2015.11 (2015), pp. 1–34. DOI: `10.1007/JHEP11(2015)033`.

[110] Monika Blanke et al. "Rare K and B Decays in a warped extra dimension with custodial protection". In: *Journal of High Energy Physics* 2009.3 (2009), p. 108. DOI: `10.1088/1126-6708/2009/03/108`. arXiv: `0812.3803`.

[111] Monika Blanke, Andrzej J. Buras, and Stefan Recksiegel. "Quark flavour observables in the Littlest Higgs model with T-parity after LHC Run 1". In: *European Physical Journal C* 76.4 (2016), p. 182. DOI: `10.1140/epjc/s10052-016-4019-7`. arXiv: `1507.06316`.

[112] Andrzej J. Buras, Dario Buttazzo, and Robert Knegjens. "$K^+ \to \pi^+\nu\bar{\nu}$ and ϵ'/ϵ in simplified new physics models". In: *Journal of High Energy Physics* 2015.11 (2015), pp. 1–33. DOI: `10.1007/JHEP11(2015)166`. arXiv: `1507.08672`.

[113] Tomáš Blažek and Peter Maták. "Left-Left squark mixing, $K^+ \to \pi^+\nu\bar{\nu}$ and minimal supersymmetry with large *tan* β". In: *International Journal of Modern Physics A* 29.27 (2014). DOI: `10.1142/S0217751X14501620`. arXiv: `1410.0055`.

[114] Gino Isidori et al. "Exploring the flavour structure of the MSSM with rare K decays". In: *Journal of High Energy Physics* 2006.8 (2006), p. 064. DOI: `10.1088/1126-6708/2006/08/064`. arXiv: `0604074`.

[115] Marzia Bordone et al. "Probing lepton-flavour universality with $K \to \pi\nu\bar{\nu}$ decays". In: *European Physical Journal C* 77.9 (2017), p. 618. DOI: `10.1140/epjc/s10052-017-5202-1`. arXiv: `1705.10729`.

[116] E. Cortina Gil et al. "First search for $K^+ \to \pi^+\nu\bar{\nu}$ using the decay-in-flight technique". In: *Physics Letters, Section B: Nuclear, Elementary Particle and High-Energy Physics* 791 (2019). DOI: `10.1016/j.physletb.2019.01.067`.

[117] NA62 Collaboration. "An investigation of the very rare $K^+ \to \pi^+\nu\bar{\nu}$ decay". In: (2020). arXiv: `2007.08218`.

[118] E. Cortina Gil et al. "Measurement of the very rare $K^+ \to \pi^+\nu\bar{\nu}$ decay". In: *Journal of High Energy Physics* 2021.6 (2021), p. 93. DOI: `10.1007/JHEP06(2021)093`.

[119] John R. Fry, Giuseppe Ruggiero, and Felix Bergsma. “Precision magnetic field mapping for CERN experiment NA62”. In: *Journal of Physics G: Nuclear and Particle Physics* 43.12 (2016), p. 125004. DOI: `10.1088/0954-3899/43/12/125004`.

[120] M. Noy et al. “Characterisation of the NA62 GigaTracker end of column readout ASIC”. In: *Journal of Instrumentation*. Vol. 6. 1. IOP Publishing, 2011, pp. 20–24. DOI: `10.1088/1748-0221/6/01/C01086`.

[121] G. Romagnoli et al. “Silicon micro-fluidic cooling for NA62 GTK pixel detectors”. In: *Microelectronic Engineering* 145 (2015), pp. 133–137. DOI: `10.1016/j.mee.2015.04.006`.

[122] G. Aglieri Rinella et al. “The NA62 GigaTracKer: A low mass high intensity beam 4D tracker with 65 ps time resolution on tracks”. In: *Journal of Instrumentation* 14.7 (2019). DOI: `10.1088/1748-0221/14/07/P07010`.

[123] F. Ambrosino et al. “CHANTI: A fast and efficient charged particle veto detector for the NA62 experiment at CERN”. In: *Journal of Instrumentation* 11.3 (2016), P03029. DOI: `10.1088/1748-0221/11/03/P03029`.

[124] *NA62 Framework*. URL: `na62-sw.web.cern.ch` (visited: 2021-05-06).

[125] *NA62 Framework `GitLab` repository*. URL: `gitlab.cern.ch/NA62FW/na62fw` (visited: 2021-05-06).

[126] Rene Brun and Fons Rademakers. “ROOT - An object oriented data analysis framework”. In: *Nuclear Instruments and Methods in Physics Research, Section A: Accelerators, Spectrometers, Detectors and Associated Equipment* 389.1-2 (1997), pp. 81–86. DOI: `10.1016/S0168-9002(97)00048-X`.

[127] S. Agostinelli et al. “GEANT4 - A simulation toolkit”. In: *Nuclear Instruments and Methods in Physics Research, Section A: Accelerators, Spectrometers, Detectors and Associated Equipment* 506.3 (2003), pp. 250–303. DOI: `10.1016/S0168-9002(03)01368-8`.

[128] J. Allison et al. “Geant4 developments and applications”. In: *IEEE Transactions on Nuclear Science* 53.1 (2006), pp. 270–278. DOI: `10.1109/TNS.2006.869826`.

[129] J. Allison et al. “Recent developments in GEANT4”. In: *Nuclear Instruments and Methods in Physics Research, Section A: Accelerators, Spectrometers, Detectors and Associated Equipment* 835 (2016), pp. 186–225. DOI: `10.1016/j.nima.2016.06.125`.

[130] K.L. Brown and F.C. Iselin. “Decay TURTLE (Trace Unlimited Rays Through Lumped Elements): A Computer Program for Simulating Charged Particle Beam Transport Systems, Including Decay Calculations”. In: (). DOI: `10.5170/CERN-1974-002`.

[131] L. J. Nevay et al. “BDSIM: An accelerator tracking code with particle–matter interactions”. In: *Computer Physics Communications* 252 (2020), p. 107200. DOI: `10.1016/j.cpc.2020.107200`.

[132] T. J. Roberts et al. "G4Beamline Particle Tracking in Matter-dominated Beam Lines". In: *Conf. Proc. C* 0806233 (2008). Ed. by Ivan Andrian and Christine Petit-Jean-Genaz, WEPP120.

[133] Elisa Minucci. "Search for Lepton Number and Flavor violation in K decays at the NA62 experiment". PhD thesis. Louvain U., 2018.

[134] Lubos Bician. "Measurement of $K^+ \to \pi^+\mu^+\mu^-$ Decay Form Factor and Evaluation of Muon Veto and Charged Hodoscope Efficiencies at NA62 Experiment at CERN". Presented 06 May 2019. 2019.

[135] Marco Boretto. "First observation of the rare decay mode $K^+ \to \mu^+\nu_\mu\mu^+\mu^-$ in the NA62 experiment at CERN SPS". PhD thesis. Turin U., 2020.

[136] Petra Riedler. "Radiation damage effects and performance of silicon strip detectors using LHC readout electronics". PhD thesis. Vienna U., 1998.

[137] M. Fiorini et al. *Test of Silicon Sensors for a High Rate Pixel Detector for the NA62 Experiment*. Internal note NA62-08-01. 2008.

[138] B. Velghe et al. *Characterisation of Irradiated GigaTracker FBK n-in-p Sensors*. Internal note NA62-17-02. 2017.

[139] G. Aglieri Rinella et al. *The TDCpix Design Manual*. Tech. rep.

[140] G. Aglieri Rinella et al. "The TDCpix ASIC: High rate readout of hybrid pixels with Timing Resolution Better than 200 ps". In: *IEEE Nuclear Science Symposium Conference Record*. Institute of Electrical and Electronics Engineers Inc., 2013. DOI: `10.1109/NSSMIC.2013.6829432`.

[141] A. Kluge et al. "The TDCpix readout ASIC: A 75 ps resolution timing front-end for the NA62 Gigatracker hybrid pixel detector". In: *Nuclear Instruments and Methods in Physics Research, Section A: Accelerators, Spectrometers, Detectors and Associated Equipment* 732 (2013), pp. 511–514. DOI: `10.1016/j.nima.2013.06.089`.

[142] G. Aglieri Rinella et al. "Test-beam results of a silicon pixel detector with Time-over-Threshold read-out having ultra-precise time resolution". In: *Journal of Instrumentation* 10.12 (2015), P12016. DOI: `10.1088/1748-0221/10/12/P12016`.

[143] Georg Nuessle. "Development of a novel micro channel cooling system for the NA62 GTK detector". PhD thesis. Louvain U., CP3, 2015.

[144] Bob Velghe. "Development and commissioning of the silicon pixel GigaTracker for the NA62 experiment at CERN". PhD thesis. Louvain U., 2016.

[145] Enrico Gamberini. "Development and Commissioning of the GigaTracker Data Acquisition and Control Systems for the NA62 Experiment at CERN". PhD thesis. Ferrara U., 2017.

[146] Jan Jakubek. "Precise energy calibration of pixel detector working in time-over-threshold mode". In: *Nuclear Instruments and Methods in Physics Research, Section A: Accelerators, Spectrometers, Detectors and Associated Equipment*. Vol. 633. SUPPL. 1. North-Holland, 2011, S262–S266. DOI: `10.1016/j.nima.2010.06.183`.

[147] Mathieu Perrin-Terrin. *Pixel Dependent Time Calibration*. NA62 Gigatracker Working Group Meeting. CERN, October 2016.

[148] P.A. Zyla et al. “Review of Particle Physics”. In: *PTEP* 2020.8 (2020), p. 083C01. DOI: `10.1093/ptep/ptaa104`.

[149] Matthew Noy. *The GigaTracKer: A high time resolution pixel detector for the NA62 experiment*. Joint Instrumentation Seminar. February 2017.

[150] Luca Federici. *GigaTraKer modules summary (and calibration update)*. NA62 Gigatracker Working Group Meeting. CERN, February 2020.

[151] Michael Moll. “Radiation damage in silicon particle detectors: Microscopic defects and macroscopic properties”. PhD. Hamburg U., 1999.

[152] Claude Leroy and Pier Giorgio Rancoita. “Particle interaction and displacement damage in silicon devices operated in radiation environments”. In: *Reports on Progress in Physics* 70.4 (2007), pp. 493–625. DOI: `10.1088/0034-4885/70/4/R01`.

[153] Alexander Chilingarov. “Temperature dependence of the current generated in Si bulk”. In: *Journal of Instrumentation* 8.10 (2013), p. 10003. DOI: `10.1088/1748-0221/8/10/P10003`.

[154] *Standard Practice for Characterizing Neutron Fluence Spectra in Terms of an Equivalent Monoenergetic Neutron Fluence for Radiation-Hardness Testing of Electronics*. Standard ASTM E722-14. West Conshohocken, PA: ASTM International, 2014. DOI: `10.1520/E0722-14`.

[155] Ernesto Migliore. *Two-pixel hits in 2018 data*. NA62 Gigatracker Working Group Meeting. CERN, June 2018.

[156] Mika Huhtinen. “Simulation of non-ionising energy loss and defect formation in silicon”. In: *Nuclear Instruments and Methods in Physics Research, Section A: Accelerators, Spectrometers, Detectors and Associated Equipment* 491.1-2 (2002), pp. 194–215. DOI: `10.1016/S0168-9002(02)01227-5`.

[157] NA62 Collaboration. *Search for lepton number and flavour violation in K^+ and π^0 decays*. 2021. arXiv: `2105.06759 [hep-ex]`.

[158] E Cortina Gil et al. “Searches for lepton number violating K^+ decays”. In: *Physics Letters B* 797 (2019), p. 134794. DOI: `https://doi.org/10.1016/j.physletb.2019.07.041`.

[159] E Cortina Gil et al. “Search for π^0 decays to invisible particles”. In: *Journal of High Energy Physics* 2021.2 (2021), p. 201. DOI: `10.1007/JHEP02(2021)201`.

[160] E Cortina Gil et al. “Search for a feebly interacting particle X in the decay $K^+ \to \pi^+ X$ ”. In: *Journal of High Energy Physics* 2021.3 (2021), p. 58. DOI: `10.1007/JHEP03(2021)058`.

[161] E Cortina Gil et al. “Search for K^+ decays to a muon and invisible particles”. In: *Physics Letters B* 816 (2021), p. 136259. DOI: `https://doi.org/10.1016/j.physletb.2021.136259`.

[162] Patricia Ball and Roman Zwicky. “$B_{d,s} \to \rho, \omega, K^*, \phi$ decay form factors from light-cone sum rules reexamined”. In: *Physical Review D* 71.1 (2005), p. 14029. DOI: `10.1103/PhysRevD.71.014029`.

[163] Patricia Ball and Roman Zwicky. “New results on $B \to \pi, K, \eta$ decay form factors from light-cone sum rules”. In: *Physical Review D* 71.1 (2005), p. 14015. DOI: `10.1103/PhysRevD.71.014015`.

[164] A Ali et al. “Comparative study of the decays $B \to (K, K^*)l^+l^-$ in the standard model and supersymmetric theories”. In: *Physical Review D* 61.7 (2000), p. 74024. DOI: `10.1103/PhysRevD.61.074024`.

[165] G. D’Ambrosio et al. “Minimal flavour violation: an effective field theory approach”. In: *Nuclear Physics B* 645.1-2 (2002), pp. 155–187. DOI: `10.1016/S0550-3213(02)00836-2`. arXiv: `0207036 [hep-ph]`.

[166] Torbjörn Sjöstrand, Stephen Mrenna, and Peter Skands. “A brief introduction to PYTHIA 8.1”. In: *Computer Physics Communications* 178.11 (2008), pp. 852–867. DOI: `10.1016/j.cpc.2008.01.036`. arXiv: `0710.3820`.

[167] Lorenza Iacobuzio. “Heavy Neutral Lepton Decay Searches at the NA62 Experiment at CERN”. Presented 2019. Birmingham U., 2019.

[168] Lau Gatignon et al. *Report from the Conventional Beams Working Group to the Physics beyond Colliider Study and to the European Strategy for Particle Physics*. Tech. rep. CERN-PBC-REPORT-2018-002. Geneva: CERN, 2018.

[169] Pavel M Nadolsky et al. “Implications of CTEQ global analysis for collider observables”. In: *Physical Review D* 78.1 (2008), p. 13004. DOI: `10.1103/PhysRevD.78.013004`.

[170] C. Lourenço and H. K. Wöhri. *Heavy-flavour hadro-production from fixed-target to collider energies*. 2006. DOI: `10.1016/j.physrep.2006.05.005`. arXiv: `0609101 [hep-ph]`.

[171] Michele Corvino. “Novel technique to measure Lepton Universality ratio R_K at NA62”. Presented 2019. PhD thesis. Naples U., 2020.

[172] *Heavy Flavour Cascade Production in a Beam Dump*. Tech. rep. CERN-SHiP-NOTE-2015-009. SHiP Collaboration, 2015.

[173] Jacopo Pinzino. *New L1STRAW*. Talk at NA62 Trigger and Data Acquisition Working Group Meeting. CERN, June 2021.

[174] Wouter Verkerke and David P. Kirkby. “The RooFit toolkit for data modeling”. In: *eConf* C0303241 (2003). Ed. by L. Lyons and Muge Karagoz, MOLT007. arXiv: `physics/0306116`.